國立臺灣大學理學院地質科學研究所

碩士論文

Department of Geosciences

College of Science

National Taiwan University

Master Thesis

以遙測影像與數值模擬分析油車寮地滑之特性

On the Characteristics of Yucheliao Landslide in

Taiwan by Remote Sensing and Numerical Simulation

曹博涵

Bo-Han Tsao

指導教授：胡植慶 博士

Advisor: Jyr-Ching Hu, PhD

中華民國 108 年 7 月

July, 2019

致謝

感謝指導教授胡植慶教授數年來的指導與協助。

感謝臺大土木系王泰典教授在數值模擬相關的諸多提點與建議。

感謝海大李國添教授，林昭圭教授與歐慶賢教授多年以來的提攜與幫助。

感謝黃鐘、曾佳漢、童忻、邱俊穎、諾艾凡、鐘智承、邱家宏、施乃慈、林紹弘、孫正瑋等學長姐在研究過程中的建議與指教。

感謝成大地科系黃淳銘同學在數值模擬上的協助。

感謝釋賢與雅琳兩位經常給予建議的前輩。

感謝台北市召會邱宇光弟兄與童忻弟兄的加強與鼓勵。

感謝二信中學劉宗盛老師給予諸多參考資料。

感謝家人多年來的支持與付出，使我在學業無後顧之憂。

摘要

在西元 2009 年 8 月 6 日，莫拉克颱風襲擊台灣並引發許多山崩災害，其中包括位於嘉義縣梅山鄉油車寮聚落的油車寮地滑。根據災前與災後的相關研究，油車寮聚落附近的邊坡沿坡面發生數十公尺的位移，被認為是大規模崩塌發生的潛在區域。在本研究中，為釐清油車寮地滑的山崩機制，將應用質點影像測速(PIV)分析於兩對影像對中，並針對油車寮地滑的二維剖面模型進行有限元素法之數值模擬。

PIV 結果顯示，油車寮地滑被觸發後主要向南滑動。崩塌塊體平均水平移動距離為 40 公尺，最大滑移量為 60 公尺。然而，因地表覆蓋發生劇烈變化，以及 PIV 分析時搜尋窗格範圍過大，致使結果仍較不精確。

數值模擬結果中，由均質岩石或多層岩層組成的坡體均較滑動面已發育的坡體穩定。並且，以地表速度搭配數值模擬對潛在滑動面進行判釋的結果，雖能粗略推得滑動面形貌與深度，但與真實情形仍有出入。考量到地表下變形的機制，以此方法推估潛在滑動面可再搭配其他方法以精進。

關鍵字：大規模崩塌，油車寮地滑，質點影像測速，有限元素法，強度折減法，邊坡穩定分析

ii

Abstract

In August, 2009, the Typhoon Morakot hit Taiwan and induced many landslide hazards. An induced landslide event happened near the Yucheliao settlement, Meishan town, Chiayi county, Taiwan. According to data and research after Typhoon Morakot, slopes near Yucheliao are considered as potential region for deep-seated landslide. In this study, the characteristics of the Yucheliao Landslide event is examined with the particle image velocimetry (PIV) analysis and numerical simulation.

The PIV results show that the landslide block slipped southwardly after triggered. The block slip is 40 m averagely in horizontal distance, and the maximum slip is 60 m. However, the inaccuracy of the results occurs in the PIV analysis due to severe change in land cover and large interrogation window size.

From the numerical simulation, it is estimated that both the slope with homogeneous rock and slope with layered rock are more stable than the slope with pre-existing slip surface. The slip surface could be roughly interpreted by surface displacement with numerical modeling, but the depth and geometry have obvious differences from real situation. By considering the underground deformation of the landslide, the accuracy of interpreting potential slip surface

could be improved when other approaches are applied.

Content

Figure Index

Table Index

1. Introduction

With growing population, expansion of settlements and overexploitation in mountainous areas, catastrophic slope failures have caused extensive buildings damage and threatened human lives globally in the past decades (Dai et al., 2002; Nadim et al., 2006; Keefer and Larsen, 2007; Highland and Bobrowsky, 2008). There were more than fifty thousand people affected by catastrophic landslides in the period of 2000-2018 around the world based on the statistic of EM-DAT (Emergency Events Database) in International Disaster Database (Guha-Sapir et al., 2019). While in Taiwan, according to the database from National Science and Technology Center for Disaster Reduction (NCDR), there were over 8,000 slope failures and landslide events happened during 2000-2017, which resulted in about 970 deaths.

Many studies have investigated the basic physics of landslide triggering or reactivation, and the main factors of landslide occurrence are generally considered to be heavy rainfall and severe seismic shaking (e.g., Iverson, 2000; Keefer, 2000; Guzzetti et al., 2007; Jibson, 2007; Crosta and Frattini, 2008; Wasowski et al., 2011). Slow-moving or creeping slopes may further evolve to rapid and destructive landslides (Chigira, 1992; Dramis and Sorriso-Valvo, 1994; Kilburna and Petley, 2003; Petley et al., 2005).

1

Therefore, detecting and monitoring slope deformation can provide better clues to landslide forecast and identify potential landslide sites, and are crucial in hazard risk management and assessment. The location and scale of creeping landslides could be preliminary interpreted by the features of topography from remote sensing images, with supporting information such as geological maps, slope aspects, in situ monitoring data and field observations (Kääb, 2002; Glenn et al., 2006; Kasai et al., 2009; Lillesand et al., 2014). However, there still remain difficulties for detailed characterization of slope deformation over greater spatial and temporal scales. For the purpose of reducing casualties and property losses, not only mapping the areas susceptible to potential landslides is important but also landslide-affected area has to be considered the, as well as disaster prevention education and evacuation of protected targets for the disaster mitigation.
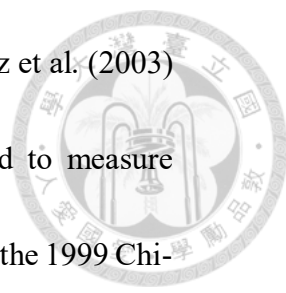
For landslide hazard assessments, the monitoring of potential deep-seated landslide is a significant issue. The application of Synthetic Aperture Radar Differential Interferometry (D-InSAR) to detect an unstable slope indicated the potential capability of this technique (Fruneau et al., 1996), and the development of Multi Temporal Interferometry (MTI) technique overcame the main factors including coherence loss in vegetated areas and

atmospheric effects limiting the performance of D-InSAR in landslide investigation (Hilley et al., 2004; Bovenga et al., 2006; Colesanti and Wasowski, 2006). In Taiwan, MTI techniques are also applied for the monitoring of potential landslides (Chen et al., 2017; Dong, 2017). However, because the deformation is too large to be derived from phase change in radar wave, D-InSAR and MTI techniques could hardly detect movement of landslide body with several meters.
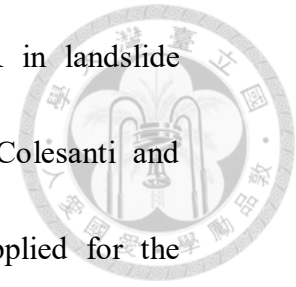
By comparing the ground objects in remote sensing images between pre-event and post-event, the horizontal displacement over 10 m could be derived. (Lin et al.,2004; Lin et al., 2014). The limitations of comparing the ground objects are that the distribution of ground objects is uneven, and the displacement with wide distribution cannot be derived. Therefore, an alternative which can remedy the limitation of MTI techniques and ground objects has to be considered.

Particle Image Velocimery (PIV) technique could be another attempt to analyze displacement of landslides. Originally, the PIV technique was applied in the hydromechanics field (Landreth rt al., 1988; Adrian, 1991; Lecordier et al., 1994). With the advantage of analyzing displacement of whole image by cross-correlation method, the PIV technique can provide displacement of

3

landslide with large movement in wide distribution. Dominquez et al. (2003) used SPOT satellite image with the cross-correlation method to measure horizontal coseismic displacement along the Chelungpu fault in the 1999 Chi-Chi earthquake. In other research work (Kääb et al.,2000; Kääb et al., 2002), the cross-correlation method was applied for monitoring glacial movement from repeated air- and spaceborne optical data. Chan et al. (2004) and Chen and Lee (2005) analyzed the surface rupture resulted from the 1999 Chi-Chi earthquake and the near-fault surface displacement for the 2003 Chengkung earthquake in eastern Taiwan with the PIV technique. Tseng et al. (2009) analyzed non-catastrophic landslide triggered by the 1999 Chi-Chi earthquake in central Taiwan with the PIV technique applied to digital aerial photos.

Slope stability and geometry of landslide subsurface are also crucial for landslide hazard assessments. For stability evaluation of a slope, accurate geotechnical site characteristics are essential. With limited site investigation data constrained by exploration techniques, subsurface information used in subsequent slope stability analysis involves uncertainty. Varnes (1978) and Carter and Bentley (1985) introduced graphical methods for inferring landslide subsurface from ground displacement. Bishop (1999) estimated the

depth of landslide sliding surface in translational slide by geometrically

balancing along downslope cross-section, and this approach is similar to

balanced cross-section method in structural geology (Woodward, 1989).
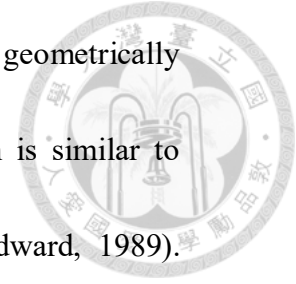
Elastic dislocation model is an alternative for estimating subsurface slip and

commonly performed for modeling static elastic deformation. (Steketee,

1958; Okada, 1985, 1992). Nikolaeva et al. (2014) applied elastic model to

invert surface displacement of a landslide estimated by InSAR and inferred

the subsurface.
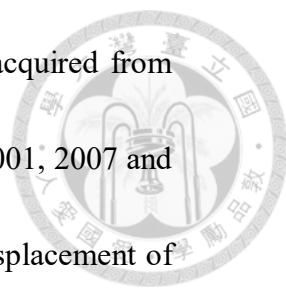
Slope stability analysis by finite element method (FEM) have been

developed in the past years (Zienkiewicz et al., 1975; Griffiths and Lanem

1999; Griffiths and Marquez, 2007; Zheng et al., 2006, 2009; Hammouri et

al., 2008; Le, 2014; Liu et al. 2015; Javankhoshdel et al. 2017; Zhang et al.,

2018). With the FEM based shear strength reduction analysis, stress, strain,

displacements and location of the critical slip surface could be obtained (Ugai

and Leshchinsky, 1995; Duncan et al., 1996; Griffiths, 1999; Matsui and San,

1992; Xu et al., 2005; Xu and Low, 2006; Zhang and Dai, 2010; Chen et al.,

2018; Liu et al., 2018; Moallemi et al.,2018). In contrast with the balanced-

cross section and elastic dislocation model, strength reduction analysis based

on the FEM is independent on ground displacement. This method depends on

5

the properties of material and geometry of the slope. Moreover, the failure process and development of strain distribution could be shown by the FEM based shear strength reduction analysis (Duncan et al., 1996; Griffiths, 1999).
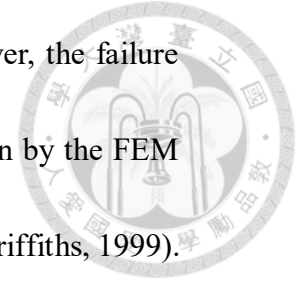
In this study, the aim is to examine the characteristics of landslide induced by the Typhoon Morakot in central Taiwan. The Typhoon Morakot influenced Taiwan during August 6, 2009 to August 10, 2009 and triggered more than 1,500 landslides. For example, the landslide event in the Shiaolin Village, Kaohsiung caused 400 deaths and the landslide body were over 25 million m3 in volume. Another example is the Yucheliao Landslide, which is in Chiayi County. In contrast with the case in the Shiaolin Village, the Yucheliao Landslide is also triggered by the rainfall brought by the Typhoon Morakot, but the landslide body almost remained and stayed on the slope (Fig. 1-1).

The purpose of this research is to estimate and characterize the Yucheliao Landslide. The work includes: (1) Cross-correlate the orthoretified aerial photographs with the PIV technique. (2) Discuss the PIV analysis to evaluate the calculated results of ground displacement. (3) The FEM based shear strength reduction analysis via numerical simulation. (4) Inverse the geometry of the landslide subsurface with ground displacement by the FEM.

In this study, there are three orthoretified aerial photos acquired from

Aerial Survey Office, Forestry Bureau, and they are taken in 2001, 2007 and

2009 respectively. These photos keep the information about displacement of

ground objects due to the Typhoon Morakot (Fig. 1-2). With orthoretified

images, the Yucheliao Landslide can be analyzed and measured by the cross-

correlation method of the PIV technique. The results of the horizontal

displacement near the Yucheliao Landslide are presented as a displacement

vector map. In addition, the PIV technique can show distinguishable regions

by the magnitude of displacement on the study area. Based on the results from

the PIV analysis, some inferences of the Yucheliao Landslide can be made.

For example, the characteristics of slope failure can be inferred, and the

mechanism of the Yucheliao Landslide would be discussed by combining

with other geological data, such as rock mechanics, well drilling, or

geological maps.

In numerical modeling, the shear strength reduction method is applied

for slope stability analysis. The Shear strength reduction method was

introduced by Dawson et al. (1999), and widely applied for slope stability

analysis and estimating potential landslide subsurface (Fig. 1-3). A simplified

slope model for the Yucheliao Landslide is introduced in this study, and the

result from the shear strength reduction will be examined by limit equilibrium method, which is another method applied for slope stability. With the ground displacement from the PIV analysis and the FEM based shear strength reduction method, the interpretation of the landslide subsurface will be on trial with the FEM analysis. The result from the numerical modeling can provide the stability of the Yucheliao Landslide, and the deformation mechanism of the landslide block can be examined with the ground deformation data.
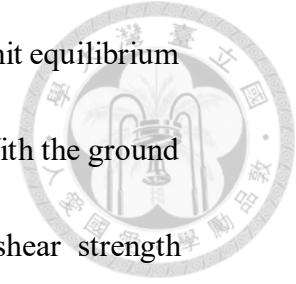
Figure 1-1. The main scarp and lateral scarp are obvious in the photo taken near Yuchelaio landslide (Lin et al., 2014). This photo is taken in the direction toward north.
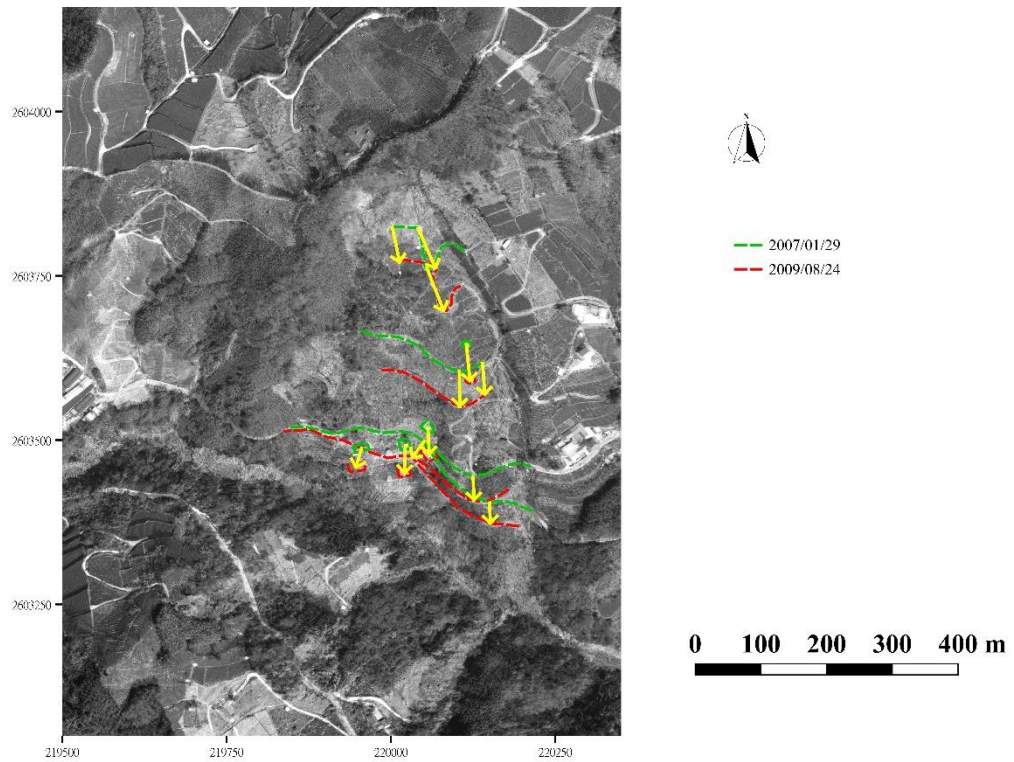
Figure 1-2. Aerial photo taken after Typhoon Morakot overlain on the one taken in the pre-event period. Green lines and green polygons represent roads and construction before failure, and red lines and red polygons represent moved roads and constructions after failure.

(a)

γ = 20 kN/m³

φ = 20°

c = 12·38 kPa

10 m

45°

(b)

Critical log-spiral surface
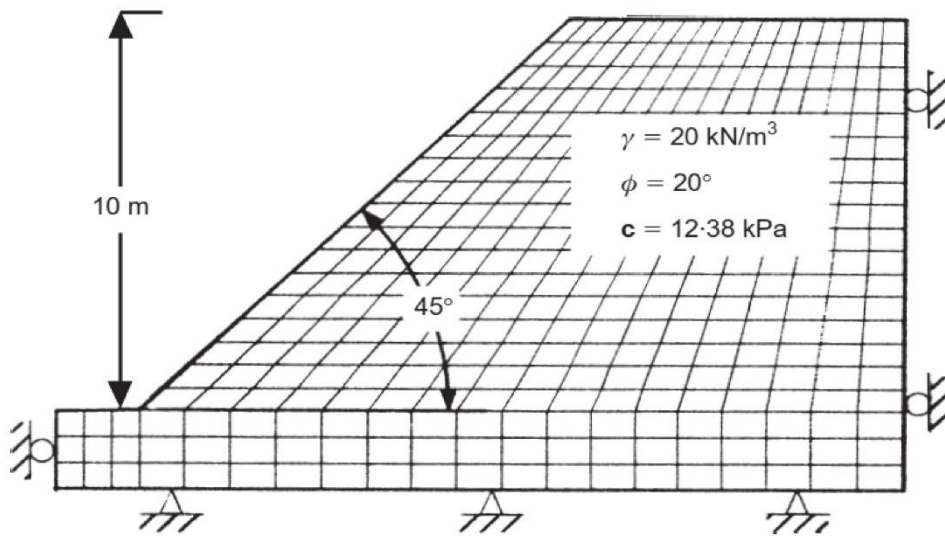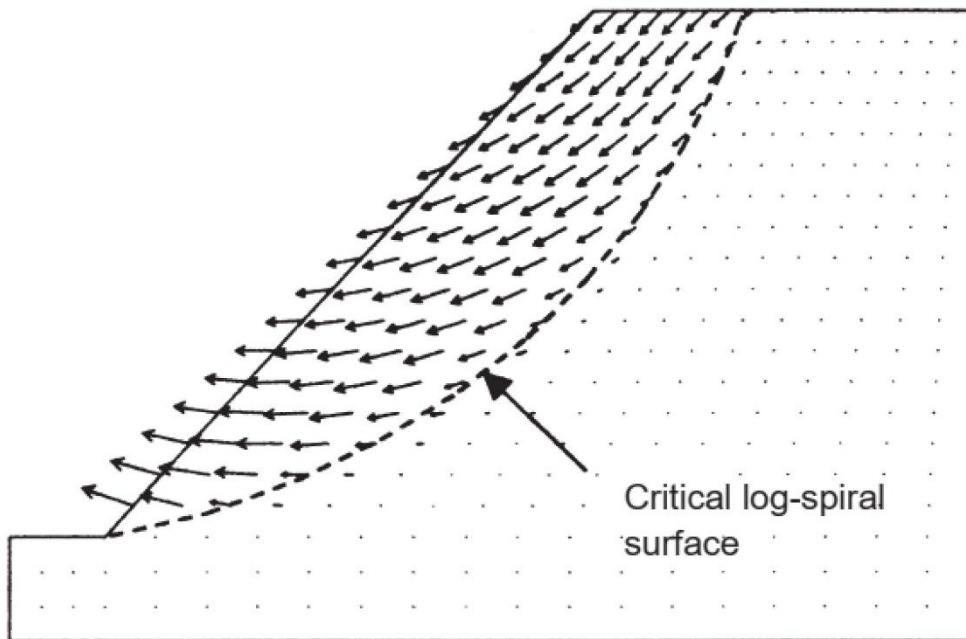
Figure 1-3. Slope model which Dawson et al. applied strength reduction method. (a) Numerical mesh of the slope model composed by homogenous soil. (b) Velocity field at collapse, along with critical log-spiral surface. (Dawson et al., 1999)

10

2. Study Area

In 2009, Typhoon Morakot led to caused landslide events near Taihe Village, Chiayi County in central Taiwan (Fig. 2-1). Near Yucheliao Settlement, Taihe Village, a landslide was trigged due to the heavy rainfall, and this landslide was named as Yucheliao Landslide. The width of the Yucheliao Landslide is 250 m in E-W direction, and the length is 600 m in N-S direction (Fig. 2-2). The height of the main scarp is 30 m, and the height of the lateral scarp is about 5-10 m. Estimated depth of sliding surface is 50 m. The area of landslide body is 14.3 hectares. The average slope angle is 26° (Fig. 2-3). Yucheliao Landslide mainly slipped southwardly and the maximum of displacement is 60 m. After the failure, the southern part of the landslide body blocked the E-W trending river to the south, and a dammed lake formed. The landslide body stayed on the slope after the failure was triggered.

The Yucheliao Landslide is located in the region of Geological map of Taiwan scale 1:50000, Yulin mapsheet (Liu et al., 2004). Rock units in the near region are Miocene sandstone. The Yucheliao Landslide is mainly composed of the Nanchung Formation (Nc) and Kandaoshan Sandstone (Kck) (Fig. 2-4). Based on geological survey and borehole data, the Nanchung

11

Formation could be divided into 4 units: Nc1~Nc4 (CGS, 2010, 2011; Lin et al., 2014). Nc1 and Nc3 are interbedded sandstone and shale, and they contain much sandstone. Nc2 and Nc4 are also interbedded sandstone and shale, but they contain much shale. There are 9 boreholes near the Yucheliao Landslide (Table 2-1). Based on the core of borehole data, it is estimated that the landslide sliding surface is located at the interface between 10 m-thick sandstone and 10-m thick sandstone and shale in Nc2 (Fig. 2-5). The geological map and profile are shown in Figure 2-4 and Figure 2-6.

The geological structure near the Yucheliao Landslide is a system of folds including anticline A, syncline B, and anticline C shown in the geological map. Syncline B and anticline C are proposed to be minor folds with the limbs of the main fold. Anticline A is NE-SW trending and plunged in SW direction. The Yucheliao Landslide is located at the eastern limb of anticline A, and anticline A plunged to the west of Yucheliao Landslide. Controlled by anticline A, the Yucheliao Landslide is inferred to slip along the dip direction of bedding. Therefore, the Yucheliao Landslide can be characterized as a dip slope failure.

12
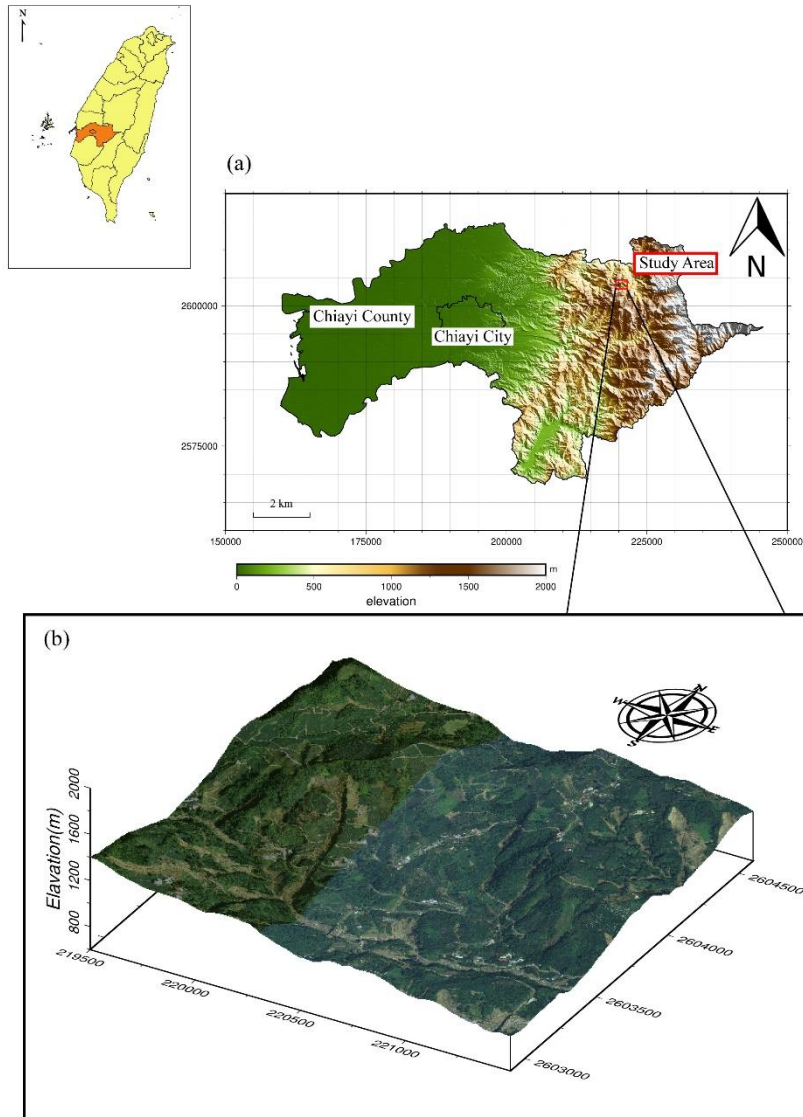
Figure 2-1. (a) Location of the Yucheliao Landslide in Chiayi County, Taiwan. Topography is based on the 40 m resolution DEM. (b) Aerial photo taken on 24/08/2009 around the Yucheliao Landslide, and the photo is draped over topography based on the 5 m resolution DEM. Coordinate system applied on these maps is the Taiwan Datum 1997 (TWD97).
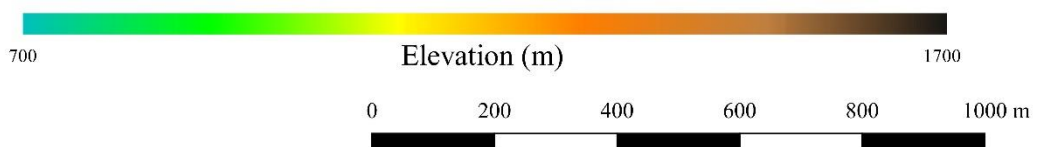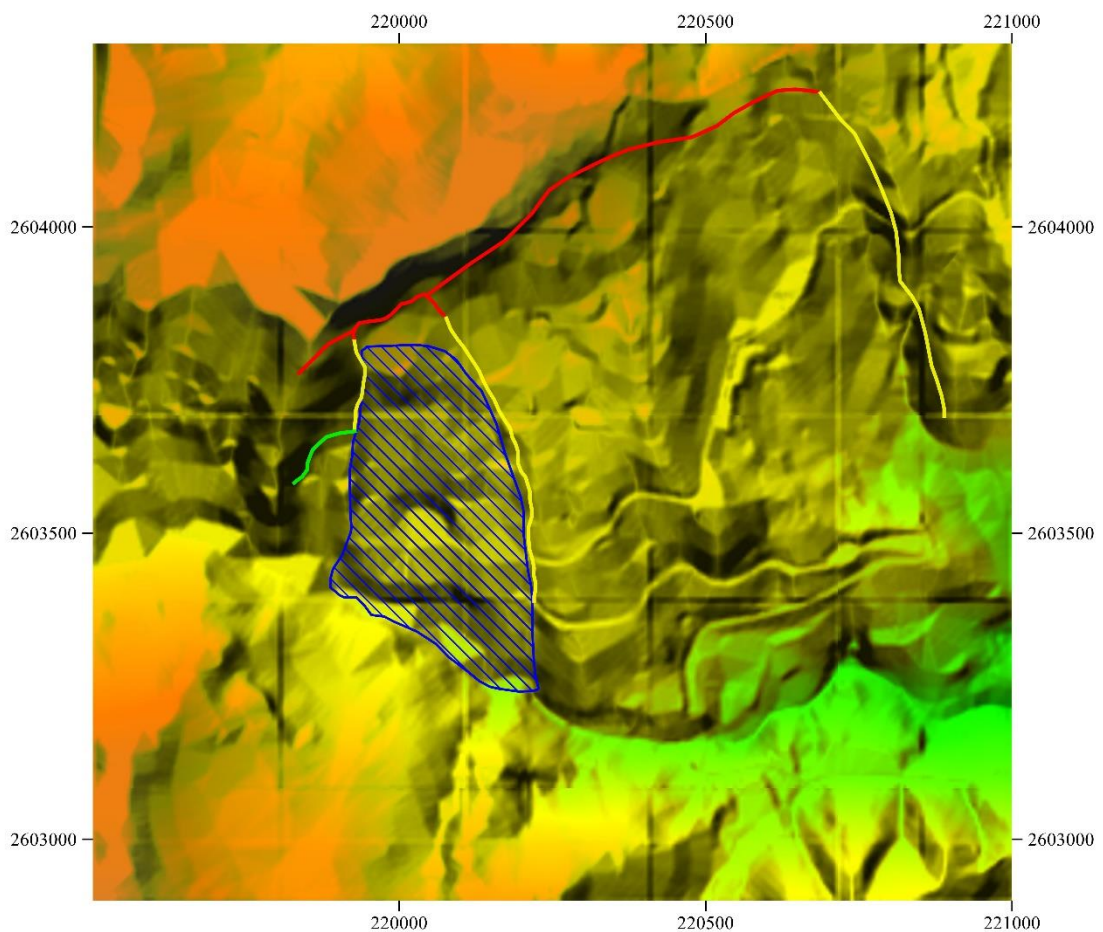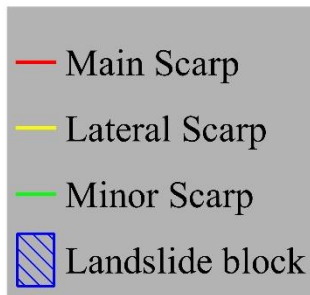
Figure 2-2. Landslide scarps determined from the 5 m resolution DEM and aerial photos.
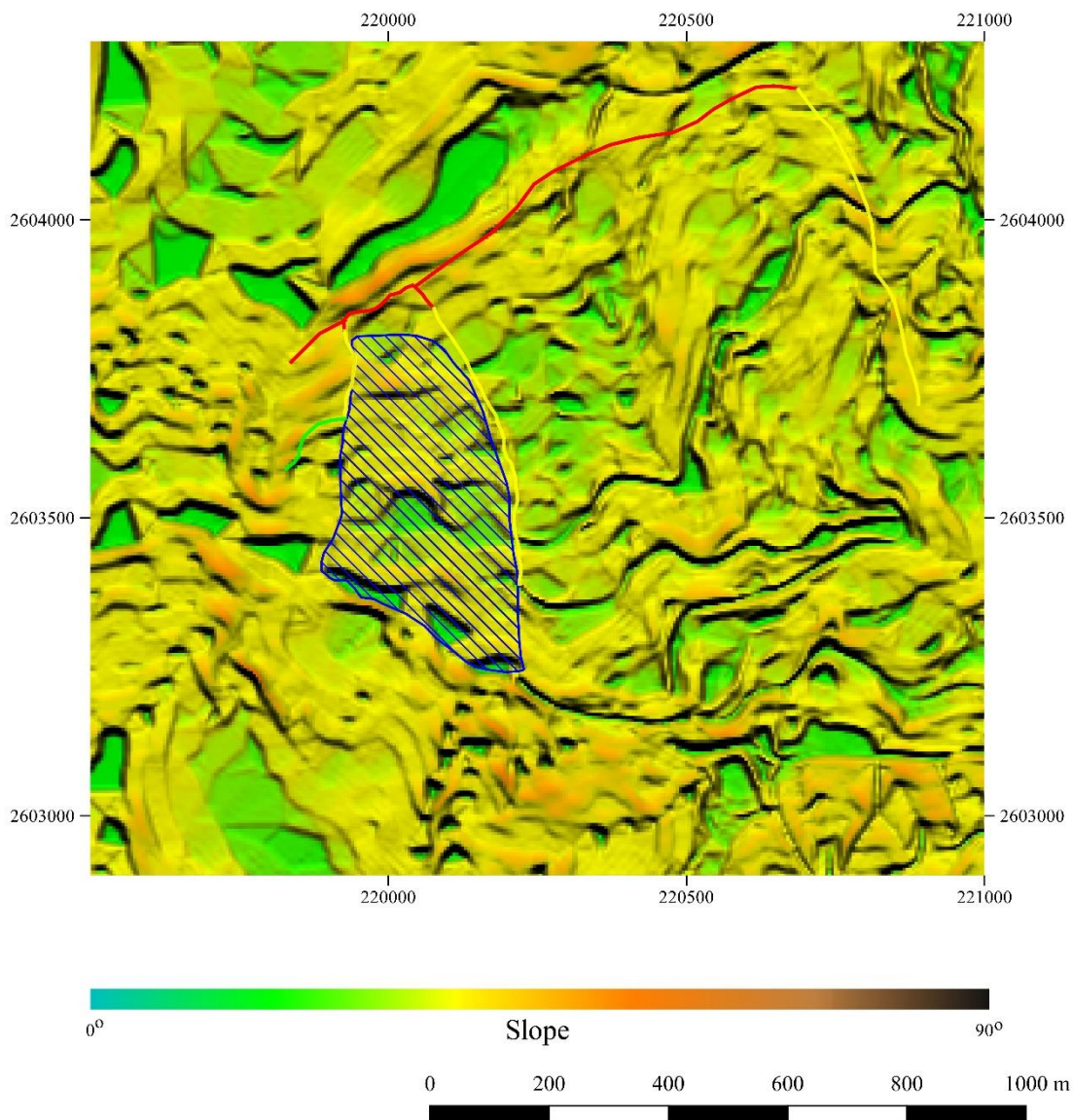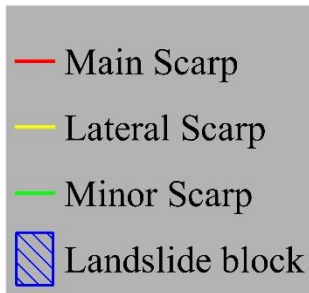
Figure 2-3. Slope map around the Yucheliao Landslide. Generally, slope angle around the Yucheliao Settlement ranges from 20° to 30°.
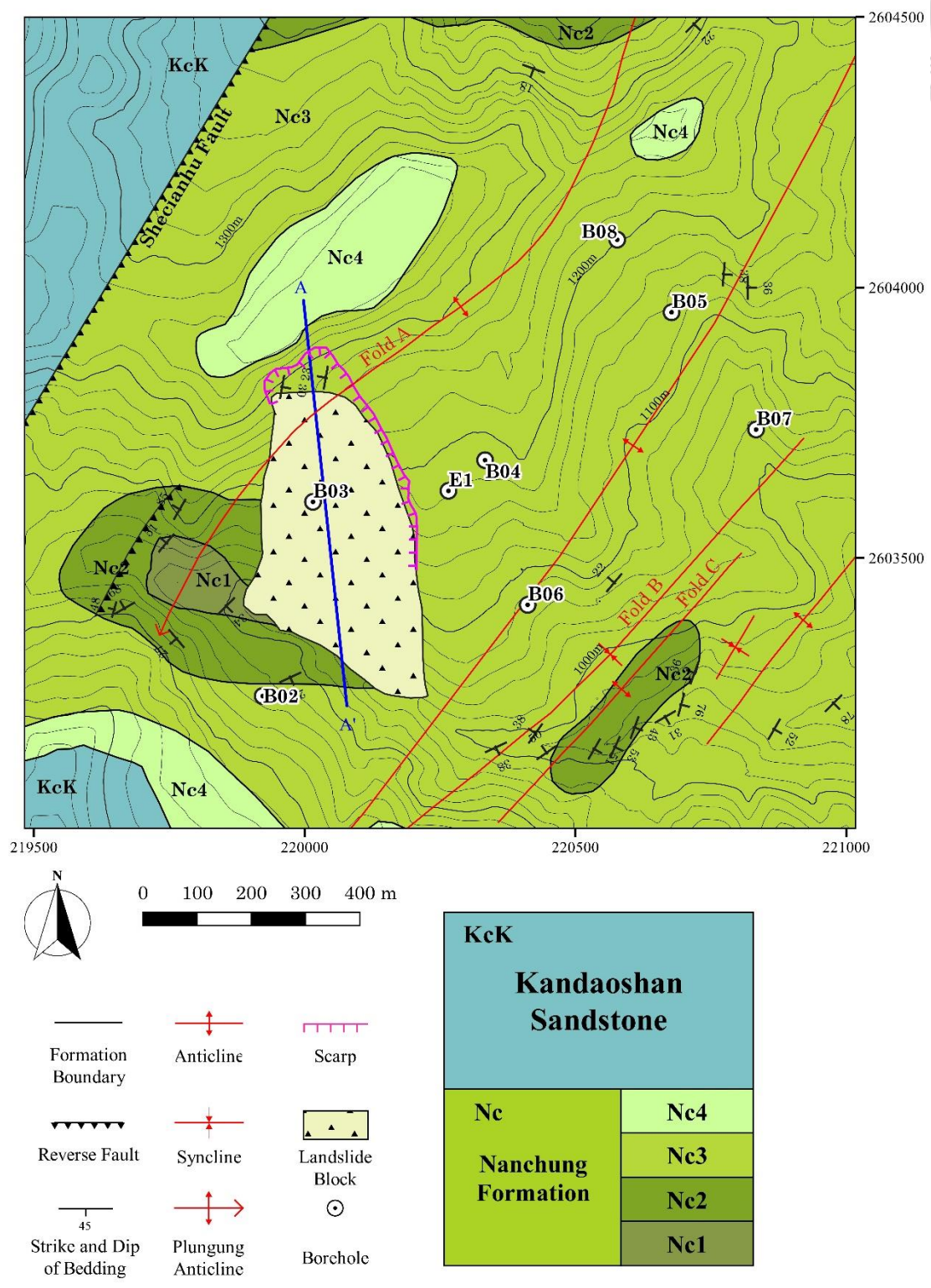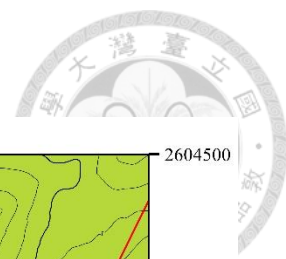
Figure 2-4. The geological map near the Yuchelaio Landslide. Coordinate system applied on the map is TWD97. (modified from Liu et al., 2004; Lin et al., 2014.)

16
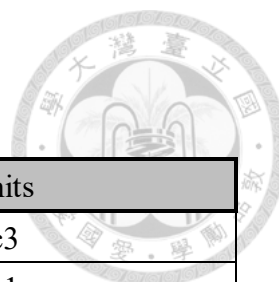
Borehole	Depth (m)	Rock units
B01	100	Nc4, Nc3
B02	80	Nc2, Nc1
B03	80	Nc2
B04	100	Nc3, Nc2, Nc1
B05	80	Nc3, Nc2
B06	80	Nc3, Nc2
B07	80	Nc3, Nc2
B08	60	Nc3, Nc2
E1	80	Nc2

Table 2-1. Rock characteristics revealed by the boreholes near the Yucheliao Landslide.
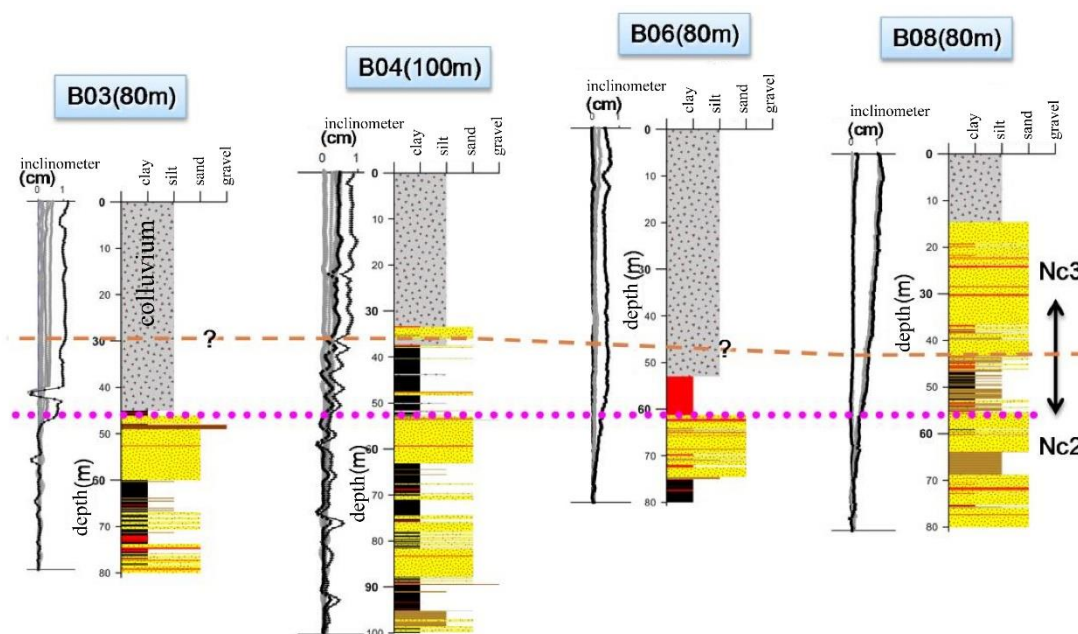
Figure 2-5. Stratigraphic columns derived from the borehole B03, B04, B06 and B08. Red part is interlayer shearing, and the pink dot line is the location of the landslide sliding surface (modified from Lin et al., 2014).
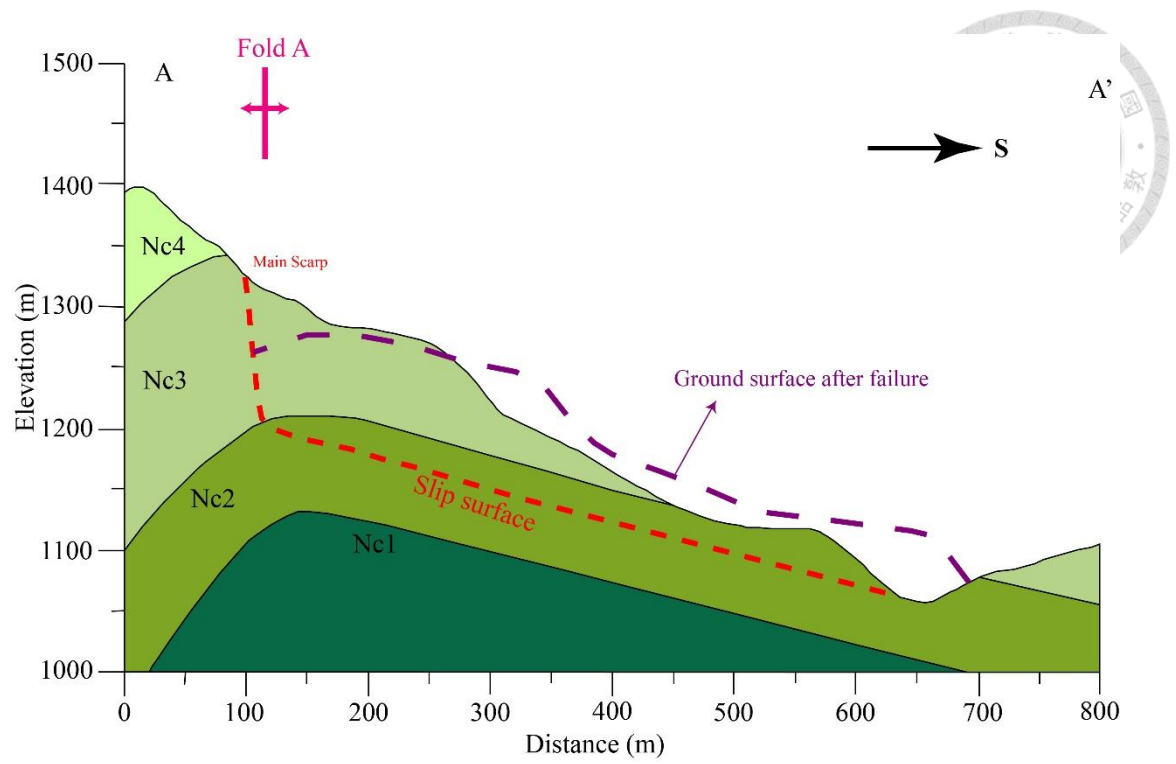
Figure 2-6. The geological profile along A-A' direction in figure 2-4. (modified from Lin et al., 2014)

3.   Methodology

3.1 Particle Image Velocimetry (PIV)

Particle image velocimetry is a whole-flow-field technique which can provide instantaneous velocity vector measurement by the cross-correlation method applied to a flow (Landreth et al., 1988; Adrian, 1991; Lecordier et al., 1994). Originally, the PIV system consists of a double-pulse laser, charge coupled device, target flow, and data analysis (Fig. 3-1). The general method of measuring velocity of the targeted flow is to place sensor in the target. However, this method may cause inaccuracy of velocity due to direct contacting between sensor and target. Without direct contacting, the PIV technique can provide the movement of the targets in two images taken at different times. For measuring displacement, the PIV technique is a convenient method to derive movement from remote sensing images. In this study, the procedure of the PIV analysis contains the cross-correlation and data analysis on the orthorectified aerial photos. The aerial images of Yucheliao Landslide are orthorectified by Aerial Survey Office, Forestry Bureau, and they were taken in 01/2001, 07/2007 and 08/2009, respectively (Fig.3-2 to 3-4). In this study, three image frames are selected in the PIV analysis. Test frame is selected for the parametric test of the PIV processing.

19

Frame A includes the area of the Yucheliao Landslide, and frame B includes

another landslide in the east of Yucheliao landslide. The software for the PIV

analysis is PIVview version 3.6 2C, which is developed by PivTec GmbH,
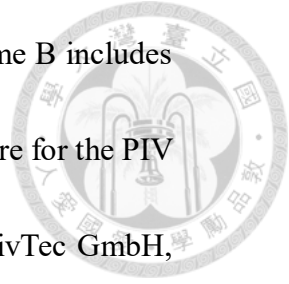
Germany.
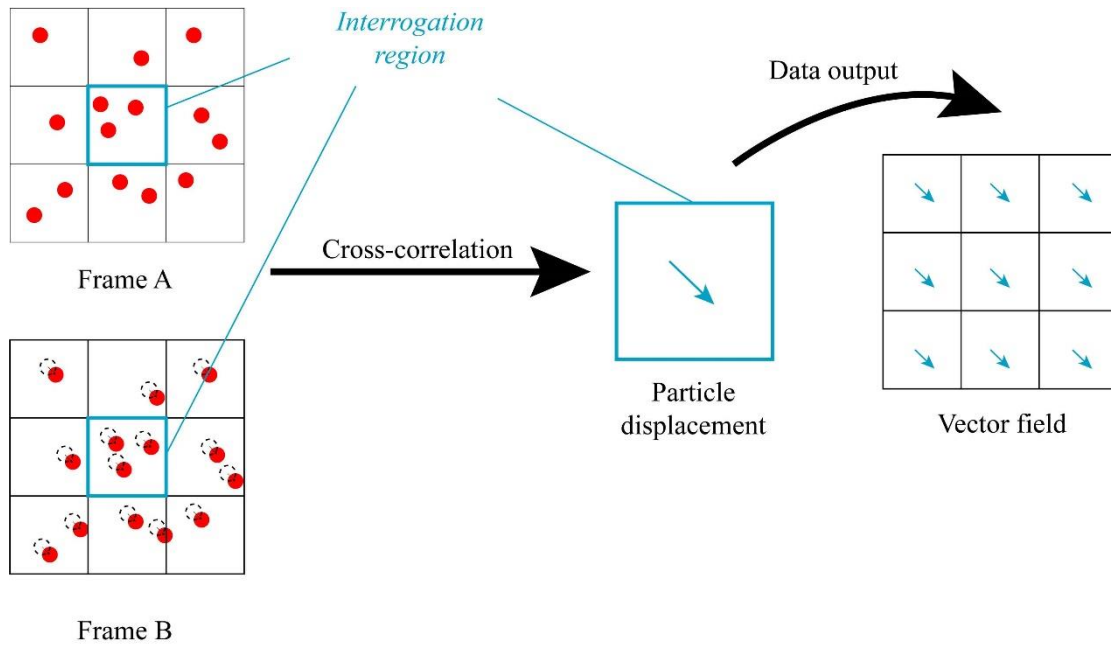
Figure 3-1. The procedure in PIV process.

(a)

(continue)

(b)

(c)

(continue)

22

(d)
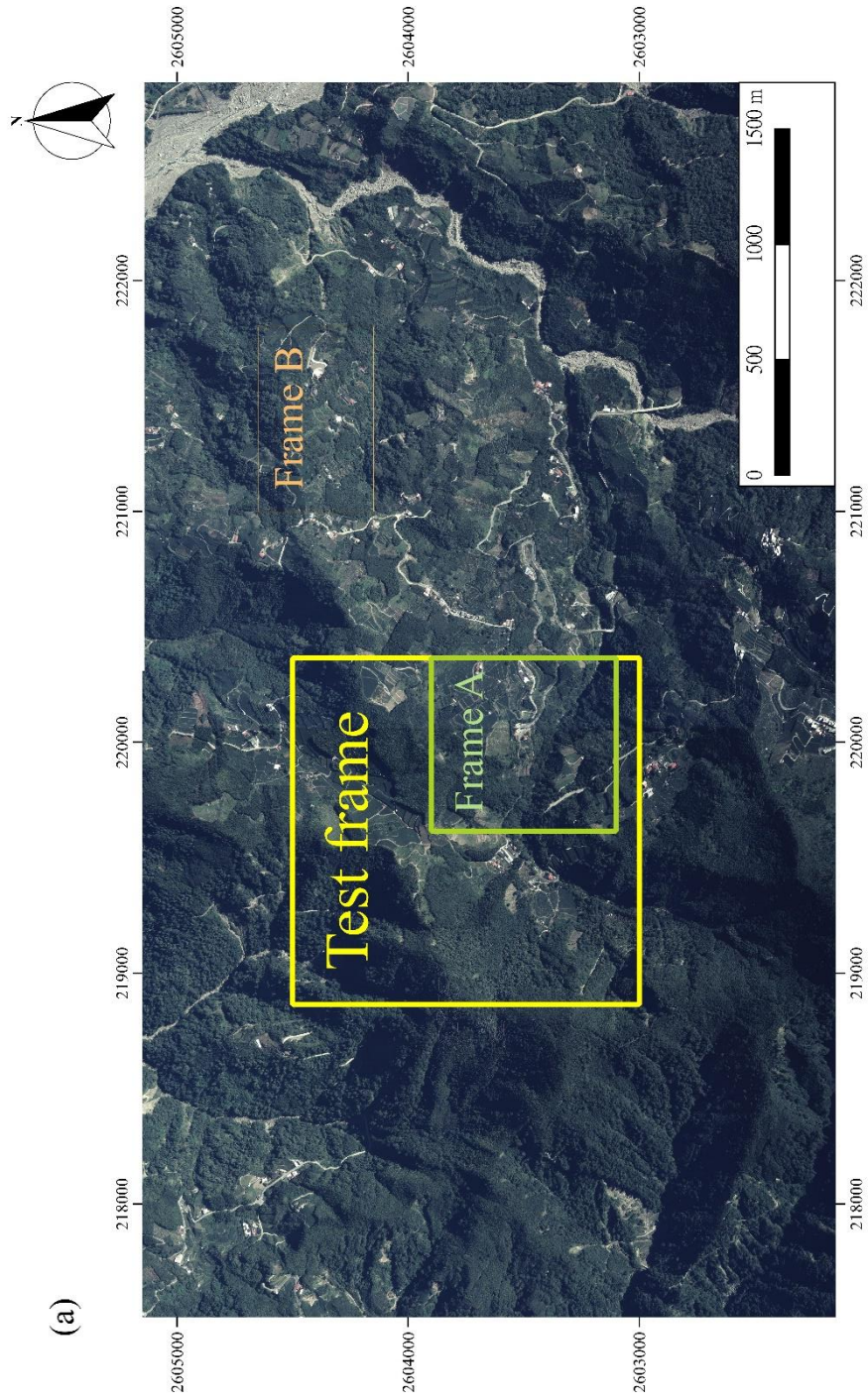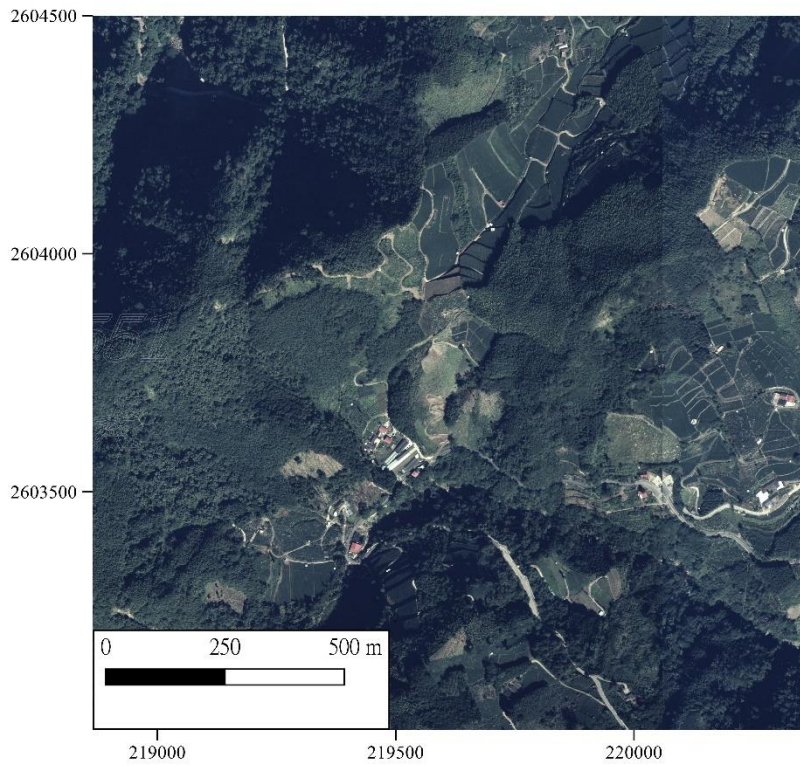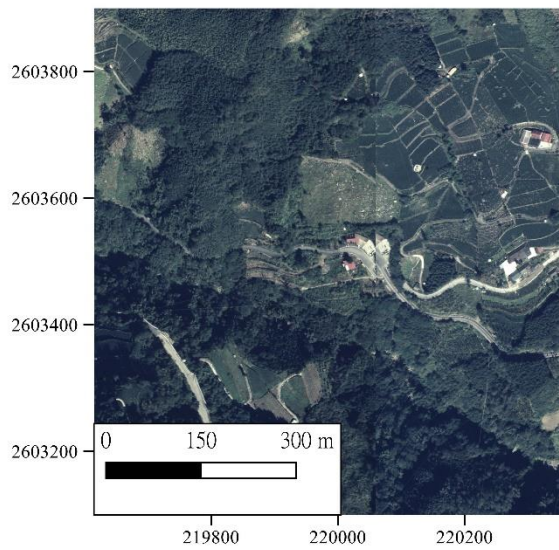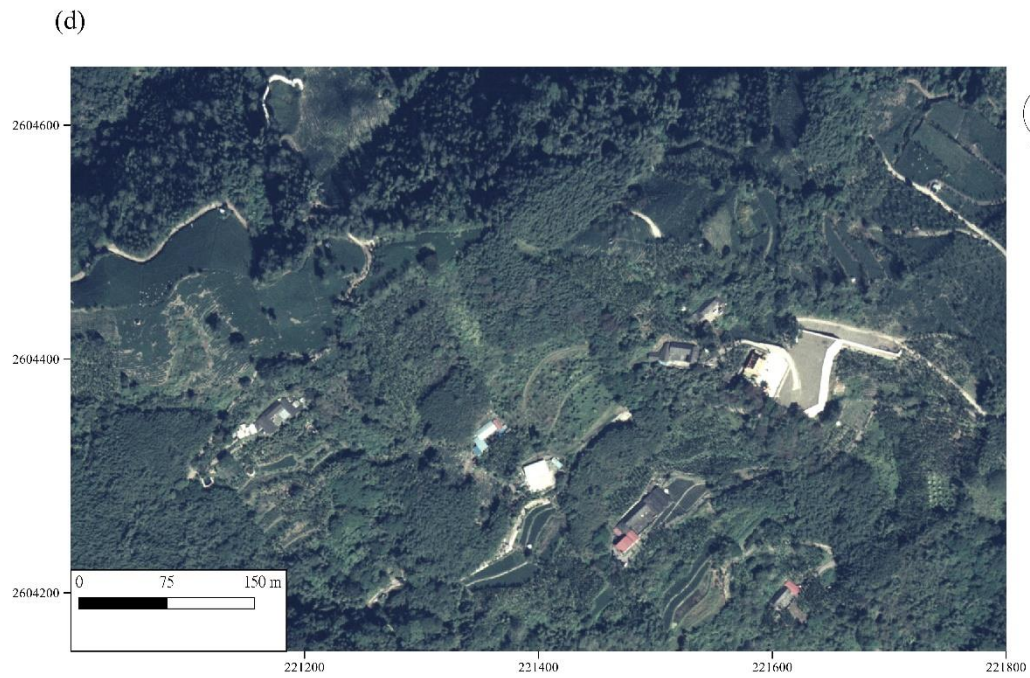
Figure 3-2. Orthorectified aerial photos taken on 2001/01/17 around the Yucheliao Settlement. The resolution of each image is 0.5 m/pixel. (a) The whole region of the original image. (b) Aerial image in the test frame. (c) Aerial image in frame A. (d) Aerial image in frame B.

23

(a)

(continue)

(b)

(c)

(continue)

25

(d)
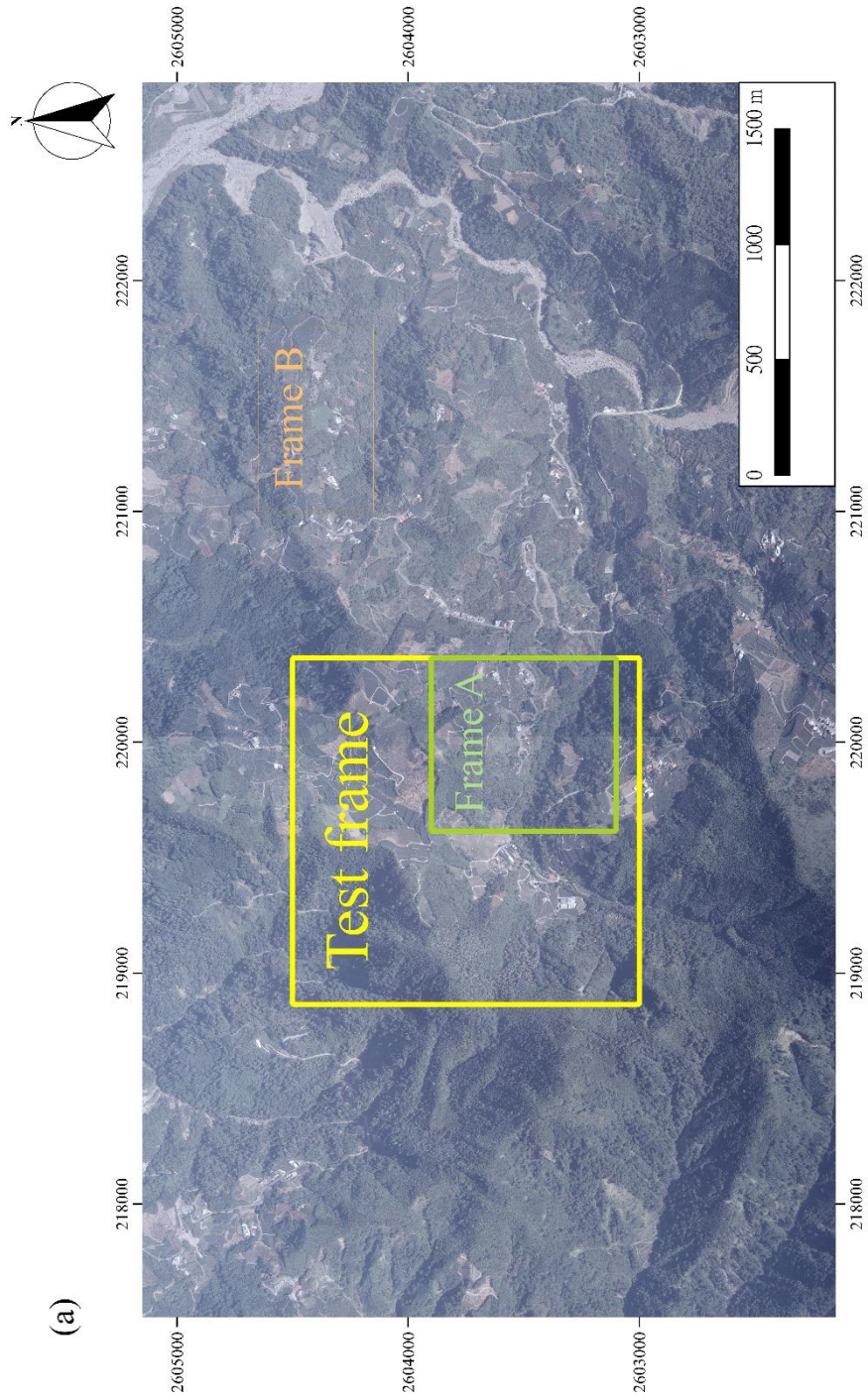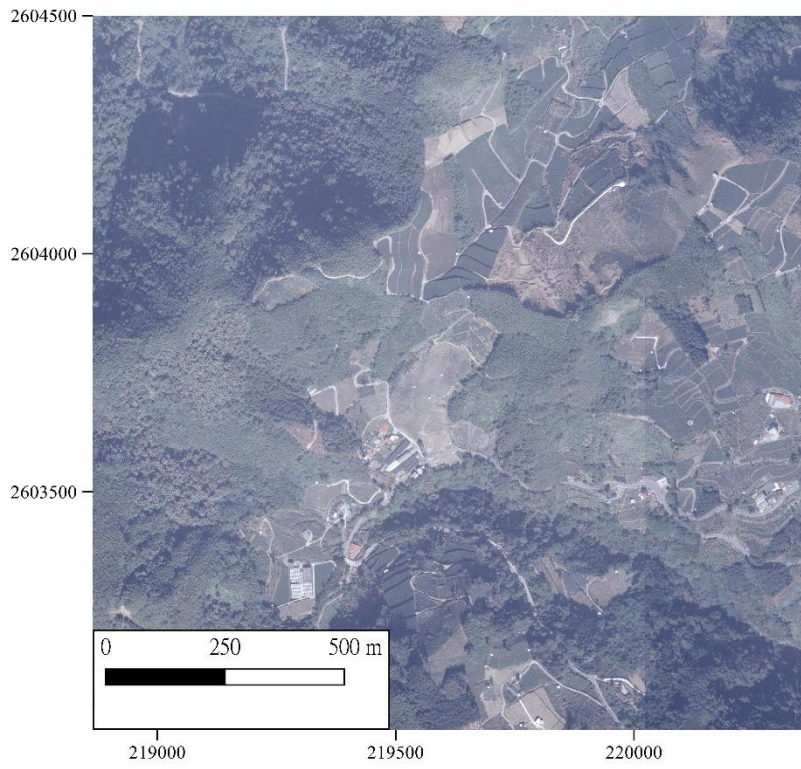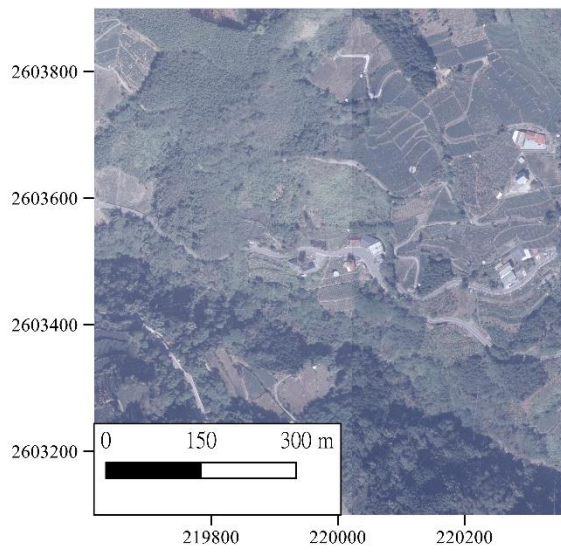
Figure 3-3. Orthorectified aerial photos taken on 2007/01/29 around the Yucheliao Settlement. The resolution of each image is 0.25 m/pixel. (a) The whole region of the original image. (b) Aerial image in the test frame. (c) Aerial image in frame A. (d) Aerial image in frame B.

(a)

(continue)

(b)

(c)

(continue)

28

(d)
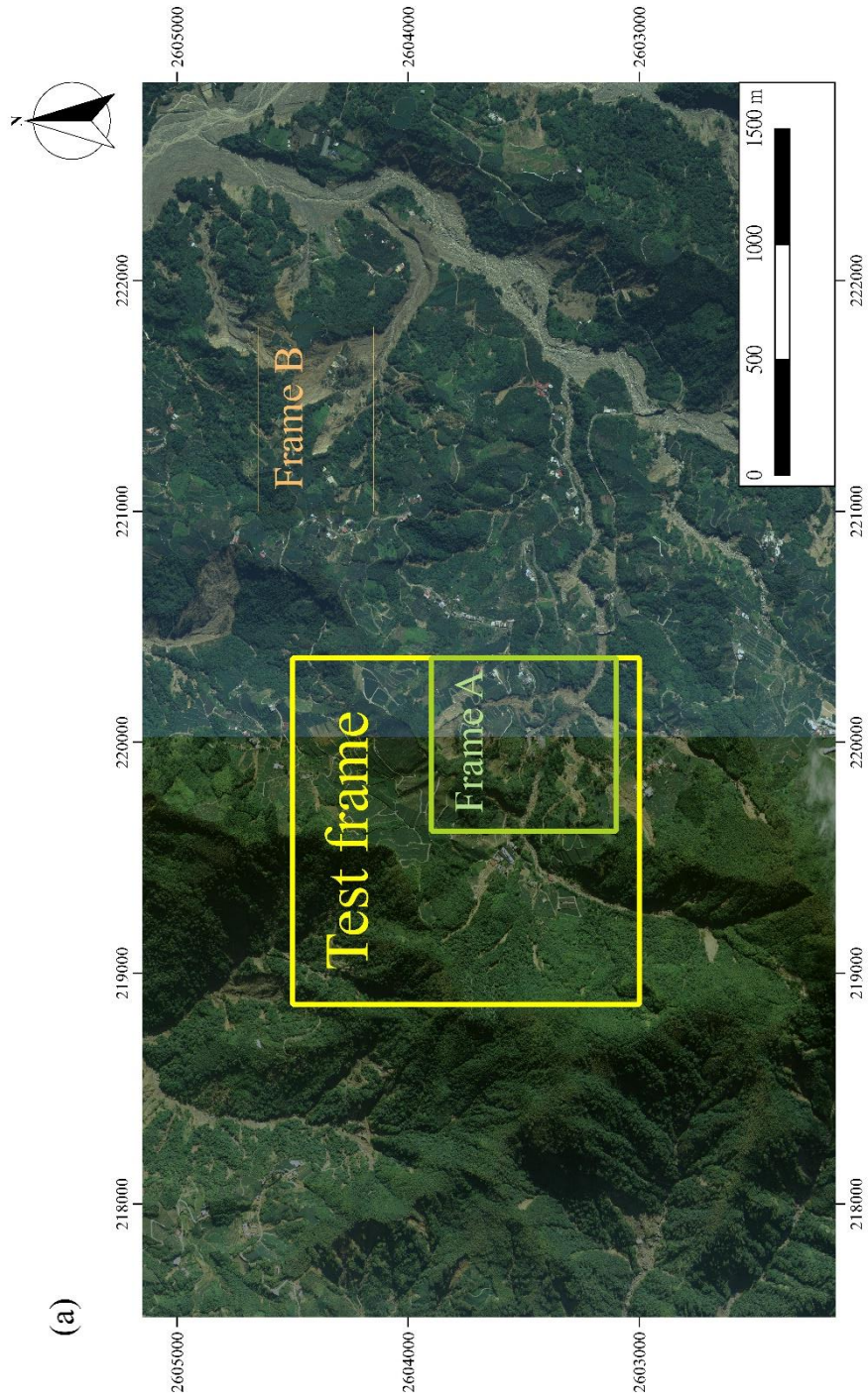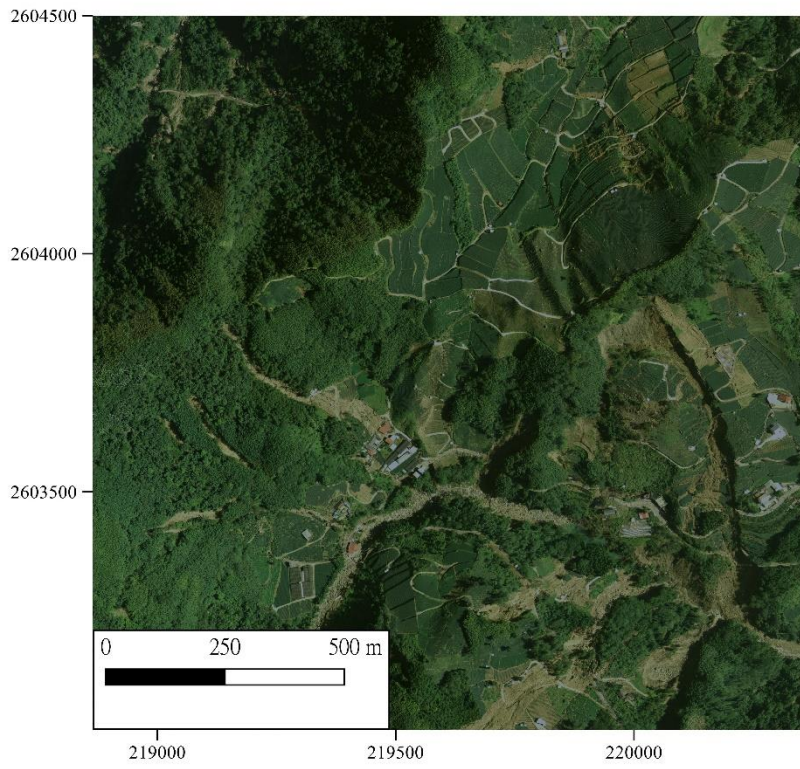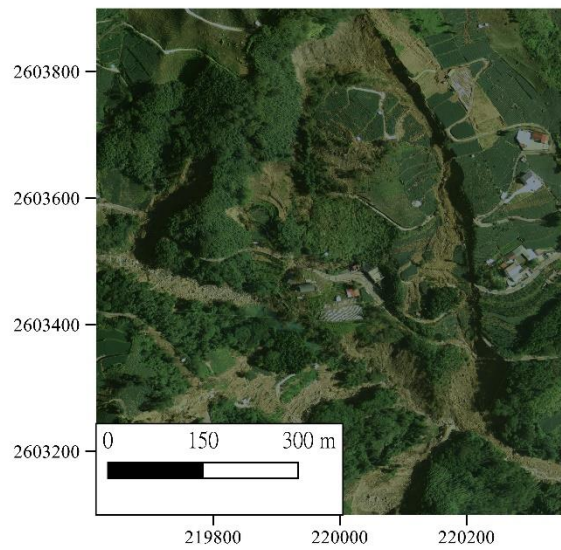
Figure 3-4. Orthorectified aerial photos taken on 2009/08/24 around the Yucheliao Settlement. The resolution of each image is 0.25 m/pixel. (a) The whole region of the original image. (b) Aerial image in the test frame. (c) Aerial image in frame A. (d) Aerial image in frame B.

3.1.1 Image preprocessing

Before importing images to the PIVview, image preprocessing is needed. In the PIV processing, the cross-correlation method is applied for calculation on grayscale value of images. That is, images must be transformed to grayscale images if images are colored. Besides, whether images in the same pair are in the same resolution is concerned. In the PIVview, coordinates of the imported images are not based on geodetic datum but the size of images (Fig. 3-5). In this research, the resolution of all images is adjusted to 0.5

m/pixel. Moreover, the brightness and contrast of the images are also adjusted.

The same objects in the images taken in different times would be obviously

different in brightness and contrast due to the difference in sunlight (Fig. 3-
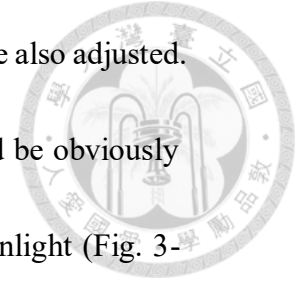
6). The procedure of image preprocessing in this study is shown in Figure 3-

7. Detailed information of the parametric tests on the image preprocessing is

shown in Table A-1.

(a)

(b)
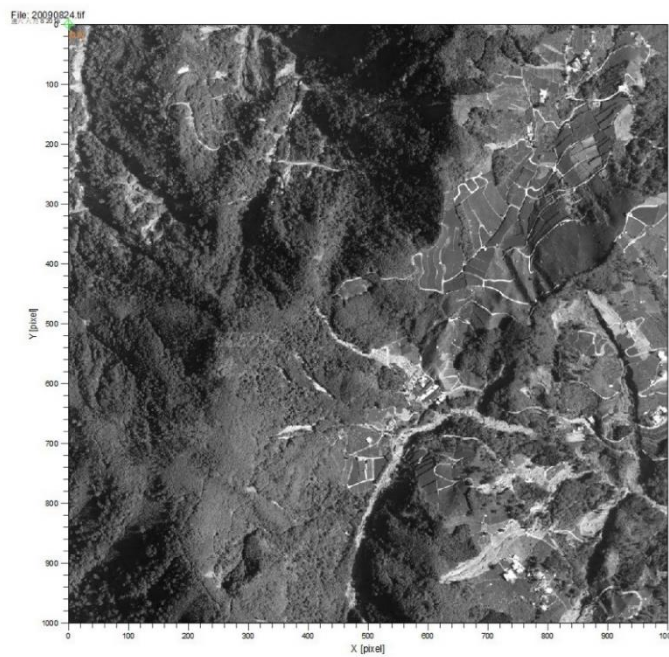
Figure 3-5. The aerial photo near the Yucheliao Landslide. (a) Original image exported from GIS software. The datum of the coordinate system is TWD97. (b) is grayscale image with 2.0 m/pixel resolution imported into the PIVview. The coordinate system is based on number of pixels.

31

(a)   **(b)**
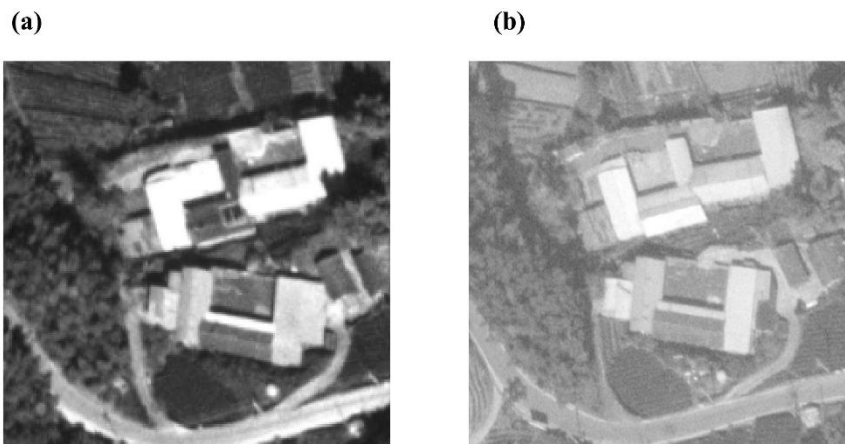
Figure 3-6. The same construction shown in the grayscale images. (a) from the image taken on 2001/01/17, and (b) from the image taken on 2007/01/29.

Transform images into grayscale images	→	Adjust brightness and contrast	→	Resample images into the same resloution
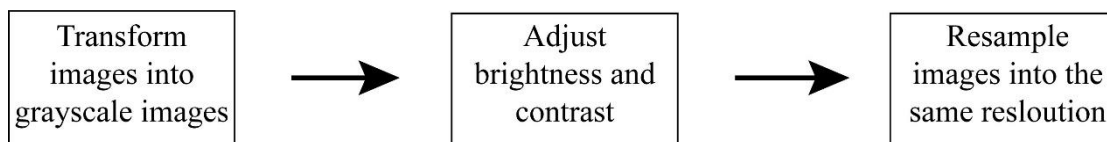
Figure 3-7. Procedure of image preprocessing.

3.1.2 Cross-correlation

To obtain precise results, the cross-correlation is a standard method estimating the degree to which two series are correlated. It is also one of the methods for the PIV technique to evaluate the displacement of every pixel which may include ground objects, such as roads, trees, houses, and etc. (Fig. 1-2). Each pixel has its gray-scale value distinguishing itself from other pixels. The cross-correlation operations are conducted in the frequency domain by executing the fast Fourier transform (FFT) on each patch to reduce the time of computation.

32
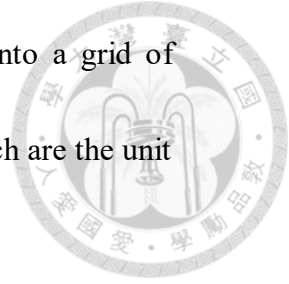
In the cross-correlation, the input images are divided into a grid of patches. Each patch consists of the image matrix of pixels which are the unit of the calculation of the cross-correlation.

The equation for cross-correlation is:

$$C(s) = \iint_{IA} I_1(X) \cdot I_2(X + s) \, dX$$

(Eq. 3-1)

$C(s)$ is the degree of correlation, I_1 and I_2 are interrogation area (IA, Chrominance matrix), and s is displacement.

The cross-correlation of $I_1(X)$ and $I_2(X+s)$ is evaluated, and normalizes by the square root of the sum of the square values of $I_2(X+s)$ over the range of X occupied by the I_1 patch. The correlation value $C(s)$ indicates the degree of match between I_1 and I_2 over the displacements. In interrogation window, the degree of correlation at all position would be calculated, and where the peak value locates would be determined as the location of moved pixel (Fig. 3-8). Therefore, the displacement in each interrogation window can be derived.

33
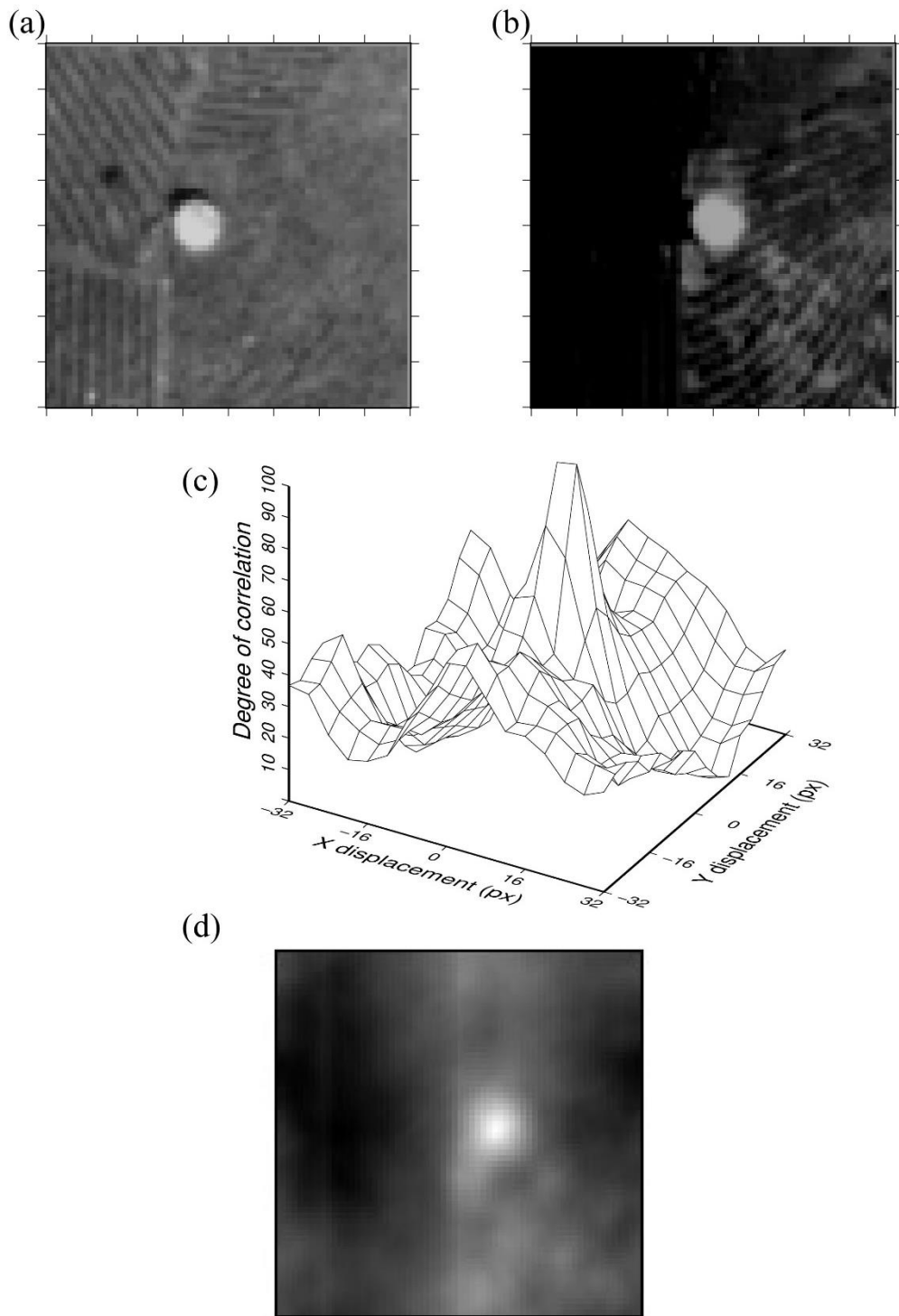
Figure 3-8. Correlation peak location corresponds to the separation of the two images. (a) and (b) are interrogation windows of the sample images taken on 2007/01/29 and 2009/08/24, respectively. (c) is the correlation plot of the interrogation window. (d) is correlation map in plane view in grayscale, and brightest region indicates the peak value of correlation.

34

3.1.3 Sub-pixel peak interpolation

The PIVview provides following peak fit algorithms to recover the sub-pixel displacement of the cross-correlation peak (PIVview User Manual, 2015).
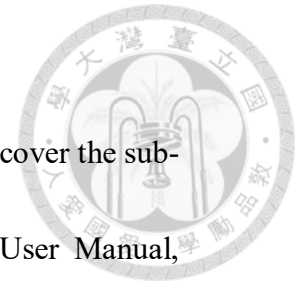
(1) 3-Point Gauss Fit: It gathers the four closest neighbors of the highest correlation to fit a 3-pont Gaussian.

(2) Least Squares Gauss Fit: It is similar to the 3-point Gauss fit but gathers surrounding eight points. The noise in the results is less than that with more simple fits, because it gathers more data for the position of the correlation peak.

(3) 3-Point Parabolic: It is similar to 3-point Gauss fit expect that it only fits a parabola through the three points.

(4) Center-of-Mass Fit: This algorithm gathers specific number of correlation values surrounding the maximum, and then calculates the associated first moment or center of mass. Generally, it is not suitable for the narrow correlation peaks which are recovered from typical images, and it could be well applied for images with lager features.

(5) Whittaker Reconstruction: It reconstructs the correlation function

from all the correlation value along horizontal and vertical direction which crossed the brightest correlation peak. Then, it estimates the maximum correlation value from the function.
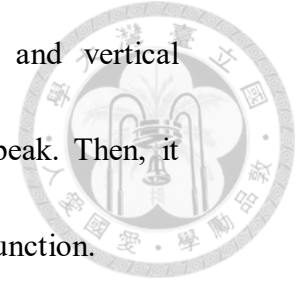
(6) Nonlinear Peak Fit: This method gathers up to N^2 points for parametric fit to a Gaussian-shaped function which allows for peak ellipticity. The peak shape is estimated by the auto-correlation function of the input images which may reduce processing speed.

3.1.4 Patch size

The unit of calculation of the PIV analysis within an image is a patch consisting of a matrix of specified pixel intensity in the range from 0 to 255. In thr PIV analysis, patch size affects the result from the cross-correlation method. White et al. (2003) tested a series of six PIV analyses, in which the whole 500 pixels $\times$ 500 pixels random image was covered in square patches with the side length to be 8, 16, and 32 pixels. Each PIV result revealed a scatter of values, being distributed close to zero. Large patches produced less scatter and improved precision (Fig. 3-9)

The empirically derived curve UB in Figure 3-9 is an upper bound on the precision error, and is given by the following equation: (White et al.,2003)

36

$$\rho = \frac{0.6}{L} + \frac{150000}{L^8}$$
(Eq. 3-2)

ρ is the precision error determined by the image width in pixels, and L is patch size.

The patch size can decide the reasonable magnitude of displacement. That, from the test above, larger patches in the PIV analysis improve. However, smaller patches allow input images to have larger number displacement gradient precision, but are worse in precision. Thus, a series of tests are needed in the PIV analysis. Results of parametric tests on patch size are shown in Table A-2. Considering the results of parametric tests and recorded maximum displacement of Yucheliao landslide, the size of the interrogation window is set to be 32 pixels in the pre-event pair, and it is set to be 256 pixels in the post-event pair.
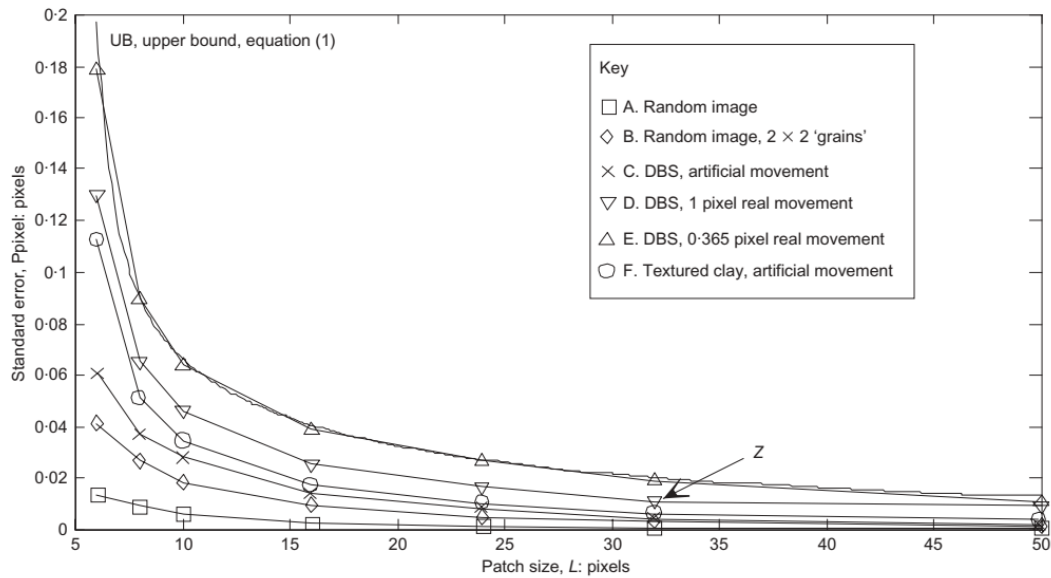
Figure 3-9. The precision of the PIV technique against patch size. In these experiments, DBS means Dog's Bay Sand in Ireland. (White et al., 2003)

3.1.5 Multi-pass and multi-grid interrogation

In the PIVview, three interrogation methods are available to define correlations applied on images (PIVview User Manual, 2015).

(1) Standard, single-pass interrogation: In the single pass interrogation, classical interrogation would be applied without additional passes to improve the result. Generally, standard interrogation is preferred while starting the PIV processing with a new image set in unknown signal quality.

(2) Multiple-pass interrogation: In this interrogation method, the interrogation of the image is repeated at least once. In following passes, the image sample positions are offset by the integer

38

determined in the preceding pass. Once the residual shifts are less

than one pixel, the re-evaluation is no longer necessary.
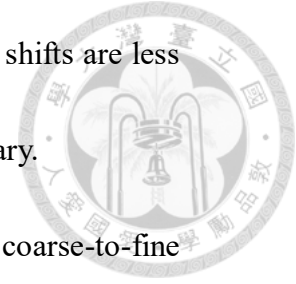
(3) Multi-grid interrogation: This method uses a coarse-to-fine

pyramid approach by starting with larger interrogation windows on

a coarse grid and refining windows in each pass.

Results of parametric tests on interrogation methods are shown in Table

A-2.

3.2 Finite Element Method (FEM)

Finite Element Method is a method for numerical simulation. For

engineering, calculating the strain or the stress of a complex model is

impossible since the simultaneous equation of this model is hardly derived.

In the FEM, a complex object could be divided into several small units, which

are called elements. Since the geometry of each element is simplified after

dividing the object, the equation for the deformation of each element can be

derived.

In this study, the software for the FEM analysis is Abaqus version 2018,

which is developed by Dassault Systèmes, France. Abaqus includes following

three modules: standard, explicit, and pre- and post-processing. The first two

modules are applied for the FEM analysis, and they can process structural

39

analysis, and non-linear, transient and dynamic analysis. The third module

provides numerical analysis and displays results, such as stain-stress contour,

vector maps, and user-defined X-Y plot.

3.2.1 Basic of FEM

The concept of the FEM is that any continuous quantity can be

approximated by discontinuous functions, and the boundary of each

discontinuous function is a continuous quantity. In physical condition, the

continuous quantity is divided into several units (elements), and the stiffness

equation of each unit can be derived. After the stiffness matrix composed of

the stiffness equation is derived, the simultaneous equations can be solved by

matrix method. Then, the approximation of the target can be derived.

There are two methods of FEM: displacement method and energy

method.

In displacement method, it is assumed that the variation of physical

property is continuous. The displacement on a node is the nodal displacement,

and the force on a node is the nodal force. According to the Hooke's Law:

$$F=KX \tag{Eq. 3-3}$$

(F: force; K: elastic modulus; X: displacement)

In each unit, this relationship could be expressed as:

40

$$[f]=\{k\}[x] \tag{Eq. 3-4}$$

([f]: nodal force; [k]: element stiffness matrix; [x]: displacement matrix)

According to the relationship between nodes, all elements could be combined to the global stiffness equation:

$$[F]=\{K\}[X] \tag{Eq. 3-5}$$

([F]: global nodal force; [K]: global stiffness matrix; [X]: global nodal displacement)

Then, Gaussian elimination method and iteration method are applied to solve the matrix, and the displacement, force or other physical quantities could be derived.

However, displacement method is hardly applied on two-dimensional or three-dimensional continuums because the stiffness matrix cannot be directly derived. Therefore, the energy method is considered.

First, the object could be divided into smaller units (elements). The shape of the element is fixed, and the shape function of the element is fixed. Considering the elastic behavior, the strain energy is:

$$U = \int Fdx \tag{Eq. 3-6}$$

Taking one-dimensional rod element as example, if the deformation of the rod element is linear approximation, the displacement function is:

41

$$u = A_0 + A_1 x \qquad \text{(Eq. 3-7)}$$

The eq. 3-7 could be expressed in matrix form:

$$u \equiv [1 \ x] \begin{Bmatrix} A_0 \\ A_1 \end{Bmatrix} \qquad \text{(Eq. 3-8)}$$

While x=0, u=u_1. While x=1, u=u_2. Then eq. 3-6 could be expressed

as:

$$\begin{Bmatrix} u_1 \\ u_2 \end{Bmatrix} = \begin{bmatrix} 1 & 0 \\ 1 & 1 \end{bmatrix} \begin{Bmatrix} A_0 \\ A_1 \end{Bmatrix} \qquad \text{(Eq. 3-9)}$$

or:

$$d = CA \qquad \text{(Eq. 3-10)}$$

d is modal displacement.

From eq. 3-7, matrix A could be derived.

$$\begin{Bmatrix} A_0 \\ A_1 \end{Bmatrix} = \begin{bmatrix} 1 & 0 \\ -1/l & 1/l \end{bmatrix} \begin{bmatrix} u_1 \\ u_2 \end{bmatrix} \qquad \text{(Eq. 3-11)}$$

From eq. 3-6 and eq. 3-7, u and A could be expressed as:

$$u = (\alpha C^{-1})d = Nd$$
$$A = C^{-1}d \qquad \text{(Eq. 3-12)}$$

N is called as shape function or shape matrix and expressed as:

$$N = \alpha C^{-1} = [1 \quad x] \begin{bmatrix} 1 & 0 \\ -1/l & 1/l \end{bmatrix} \qquad \text{(Eq. 3-13)}$$

The relationship between strain and displacement function is:

$$\varepsilon_x = \frac{du}{dx} = \begin{bmatrix} \frac{dn}{dx} \end{bmatrix} d = [\frac{-1}{l} \quad \frac{1}{l}] \begin{Bmatrix} u_1 \\ u_2 \end{Bmatrix} \qquad \text{(Eq. 3-14)}$$

or:

42

$$\varepsilon_x = Bd \qquad\qquad\qquad\qquad\qquad\qquad \text{(Eq. 3-15)}$$

If the volume of the rod element is V, and strain energy could be

expressed as:

$$U_p = \frac{1}{2}\int_v \sigma_x^t \varepsilon_x dV \qquad\qquad\qquad\qquad \text{(Eq. 3-16)}$$

For elastic deformation:

$$\sigma^x = E\varepsilon^x \qquad\qquad\qquad\qquad\qquad\qquad \text{(Eq. 3-17)}$$

E: Young's modulus

With eq. 3-15 and eq. 3-17, eq. 3-16 could be expressed as:

$$U_p = \frac{1}{2}\int_v \sigma_x^t \varepsilon_x dV = \frac{1}{2}\int_v d^t B^t EBd dV = \frac{1}{2}d^t(\int_v B^t EBdV)d \qquad \text{(Eq. 3-18)}$$

If K is defined as:

$$K = \int_v B^t EBdV \qquad\qquad\qquad\qquad\qquad \text{(Eq. 3-19)}$$

Then, the strain energy is:

$$U_p = \frac{1}{2}d^t Kd \qquad\qquad\qquad\qquad\qquad \text{(Eq. 3-20)}$$

The work form force is:

$$W = d^t F \qquad\qquad\qquad\qquad\qquad\qquad \text{(Eq. 3-21)}$$

So that, the total potential is:

$$\prod_p = U_p - W = \frac{1}{2}d^t Kd - d^t F \qquad\qquad\qquad \text{(Eq. 3-22)}$$

Considering principle of minimum potential energy, then

43

$$\frac{\partial \Pi_p}{\partial d} = \frac{\partial U_p}{\partial d} - \frac{\partial W}{\partial d} = 0 \qquad \text{(Eq. 3-23)}$$

Therefore, it could be derived that:

$$KD - F = 0 \qquad \text{(Eq. 3-24)}$$

or:

$$F = KD \qquad \text{(Eq. 3-25)}$$

The matrix equation derived from the energy method is same as eq. 3-5

derived from the displacement method, and it coincides with the force

equilibrium   and the principle of minimum potential energy.

3.2.2 Mohr-Coulomb yield criterion and Extended Drucker-Prager yield criterion in Abaqus

In Abaqus, two models are applied for the plastic part of the elastic-

plastic behavior. One is the Mohr -Coulomb model, and the other one is the

Extended Drucker-Prager model (Abaqus Analysis User's Guide, 2014).

The Mohr-Coulomb failure or strength criterion has been widely used

for geotechnical applications. Indeed, a large number of the routine design

calculations in the geotechnical area are still performed using the Mohr-

Coulomb criterion.

The Mohr-Coulomb criterion assumes that failure is controlled by the

maximum shear stress and that this failure shear stress depends on the normal

44
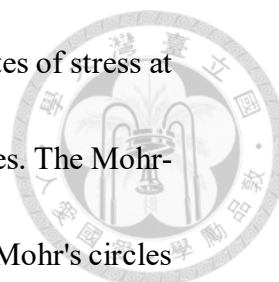
stress. This can be represented by plotting Mohr's circle for states of stress at

failure in terms of the maximum and minimum principal stresses. The Mohr-

Coulomb failure line is the best straight line that touch es these Mohr's circles

(Fig. 3-10). Thus, the Mohr-Coulomb criterion can be written as

$$\tau = c + \sigma \tan \varphi \qquad \text{(Eq. 3-26)}$$

Where τ is shear strength, c is cohesion, σ is average normal stress, and

φ is internal friction angle.
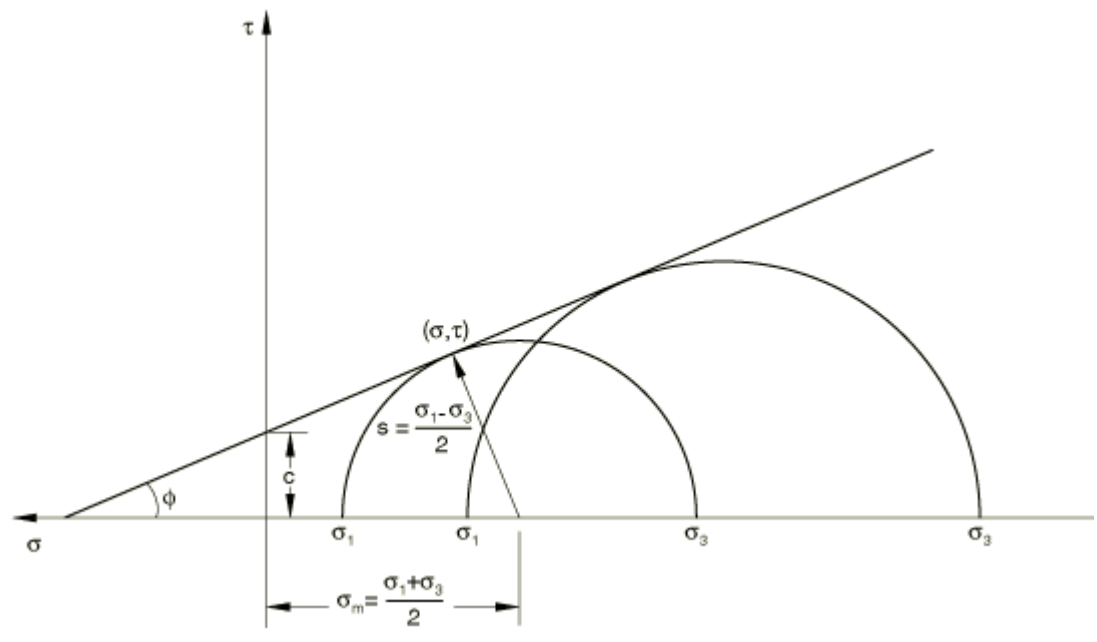
Figure 3-10. The diagram of Mohr-Coulomb criterion (Abaqus Analysis User's Guide, 2014).

From Mohr's circle,

$$\tau = s \cos \varphi \qquad \text{(Eq. 3-27)}$$

$$\sigma = \sigma_m + s \sin \varphi \qquad \text{(Eq. 3-28)}$$

Substituting for τ and φ, the Mohr-Coulomb criterion can be rewritten

45

as:

$$s + \sigma_m \sin\varphi - c \cos\varphi = 0 \qquad \text{(Eq. 3-29)}$$

where

$$s = \frac{\sigma_1 - \sigma_3}{2} \qquad \text{(Eq. 3-30)}$$

$$\sigma_m = \frac{\sigma_1 + \sigma_3}{2} \qquad \text{(Eq. 3-31)}$$

In Drucker-Prager yield criterion, the yield strength is controlled by confining pressure, and the yield function is:

$$f(I_1, J_2) = \sqrt{J_2} - \alpha I_1 - k \qquad \text{(Eq. 3-32)}$$

(k: unconfined shear strength; I_1: first invariant of stress tensor; J_2: second invariant of stress deviator tensor)

The definition of I_1 is:

$$I_1 = \sigma_x + \sigma_y + \sigma_z = \sigma_u \qquad \text{(Eq. 3-33)}$$

The definition of J_2 is:

$$J_2 = \frac{1}{6}\left[(\sigma_x - \sigma_y)^2 + (\sigma_y - \sigma_z)^2 + (\sigma_x - \sigma_z)^2\right] +$$
$$\tau_{xy}^2 + \tau_{yz}^2 + \tau_{yz}^2 = \frac{1}{2}s_{ij}s_{ij} \qquad \text{(Eq. 3-34)}$$

The eq. 3-32 could be modified to:

$$f(\xi, \rho) = \rho - \sqrt{6}\alpha\xi - \sqrt{2}k \qquad \text{(Eq. 3-35)}$$

In eq. 3-27:

46

$$\xi = I_1/\sqrt{3}$$

$$\rho = \sqrt{2J_2}$$

In eq. 3-27, k and α could be compared with cohesion and angle of internal friction in Mohr-Coulomb criterion. Figure 3-11 shows the eq. 3-32 plotted on stress space. The Drucker-Prager yield criterion displays as a circular cone and the radius increases with the confining pressure.

Drucker-Prager yield criterion in Abaqus is an extended Drucker-Prager elastoplastic model as the following equation (Hibbitt et al., 1996, 1997):

$$f = t - p \tan\beta - d = 0 \tag{Eq. 3-36}$$

In eq. 3-36:

$$t = \frac{1}{2}q\left[1 + \frac{1}{K} - \left(1 - \frac{1}{K}\right)\left(\frac{r}{q}\right)^3\right] \tag{Eq. 3-37}$$

$$d = \left(1 - \frac{1}{3}\tan\beta\right)\sigma_c \tag{Eq. 3-38}$$

$$p = \frac{1}{3}(\sigma_1 + \sigma_2 + \sigma_3) = \frac{1}{3}I_1 \tag{Eq. 3-39}$$

$$q = \sqrt{\frac{3}{2}S_{ij}S_{ij}} = \sqrt{3J_2} \tag{Eq. 3-40}$$

$$r = \sqrt[3]{\frac{9}{2}S_{ij}S_{jk}S_{ik}} = 3\sqrt[3]{\frac{1}{2}J_3} \tag{Eq. 3-41}$$

(β, d, k: material parameter; σ_c: uniaxial compressive strength)

Comparing with Mohr-Coulomb criterion, β is similar to angle of internal friction, and d is similar to cohesion. In triaxial condition, the

47

relationship between β, d and ϕ, c listed below:
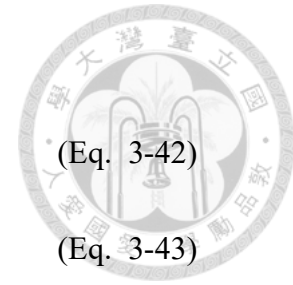
$$\tan \beta = \frac{6 \sin \phi}{3 - \sin \phi}$$ (Eq. 3-42)

$$d = 6c \frac{\cos \phi}{3 - \sin \phi}$$ (Eq. 3-43)

In Abaqus, eq. 3-37 is applied to simulate Mohr-Coulomb criterion by substituting parameters related to K (Desai et al.,1977), and K is:

$$K = \frac{3 - \sin \phi}{3 + \sin \phi}$$ (Eq. 3-44)

Figure 3-12 displays the relationship between extended Drucker-Prager criterion and Mohr-Coulomb criterion in in the deviatoric plane. Unlike the Drucker-Prager criterion, the Mohr-Coulomb criterion assumes that failure is independent of the value of the intermediate principal stress. The failure of typical geotechnical materials generally includes some small dependence on the intermediate principal stress, but the Mohr-Coulomb model is generally considered to be sufficiently accurate for most applications. In eq. 3-44, to keep the yield surface as a convex surface in the Drucker-Prager criterion, K should be in the range from 0.778 to 1.0. Thus, φ is suggested to be less than 22° when the Drucker-Prager model is applied. Generally, most geotechnical materials have $\varphi > 22°$. In this study, the Mohr-Coulomb criterion is considered since the materials in numerical simulation are not suitable for the Drucker-Prager criterion.

48
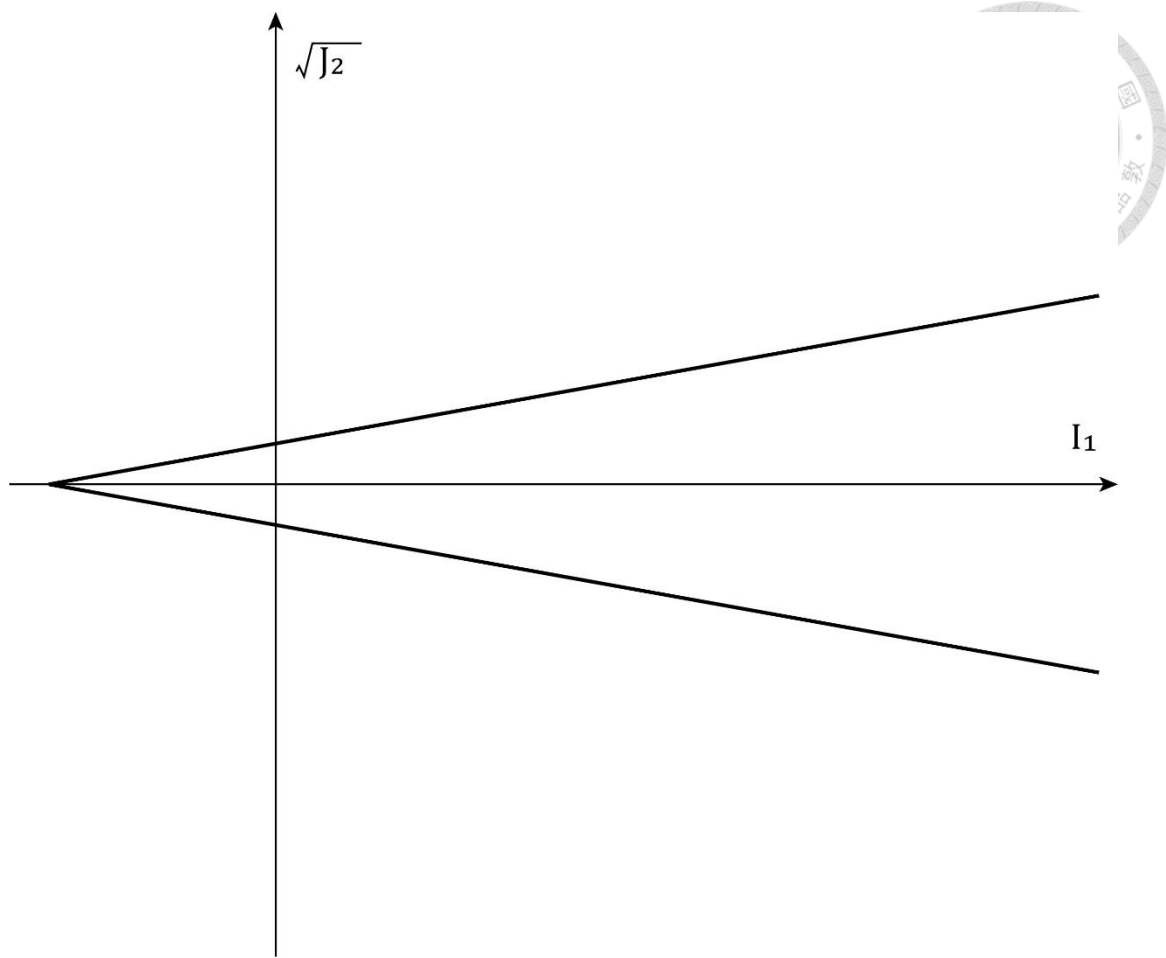
Figure 3-11. Drucker-Prager yield criterion on the stress meridian plane.
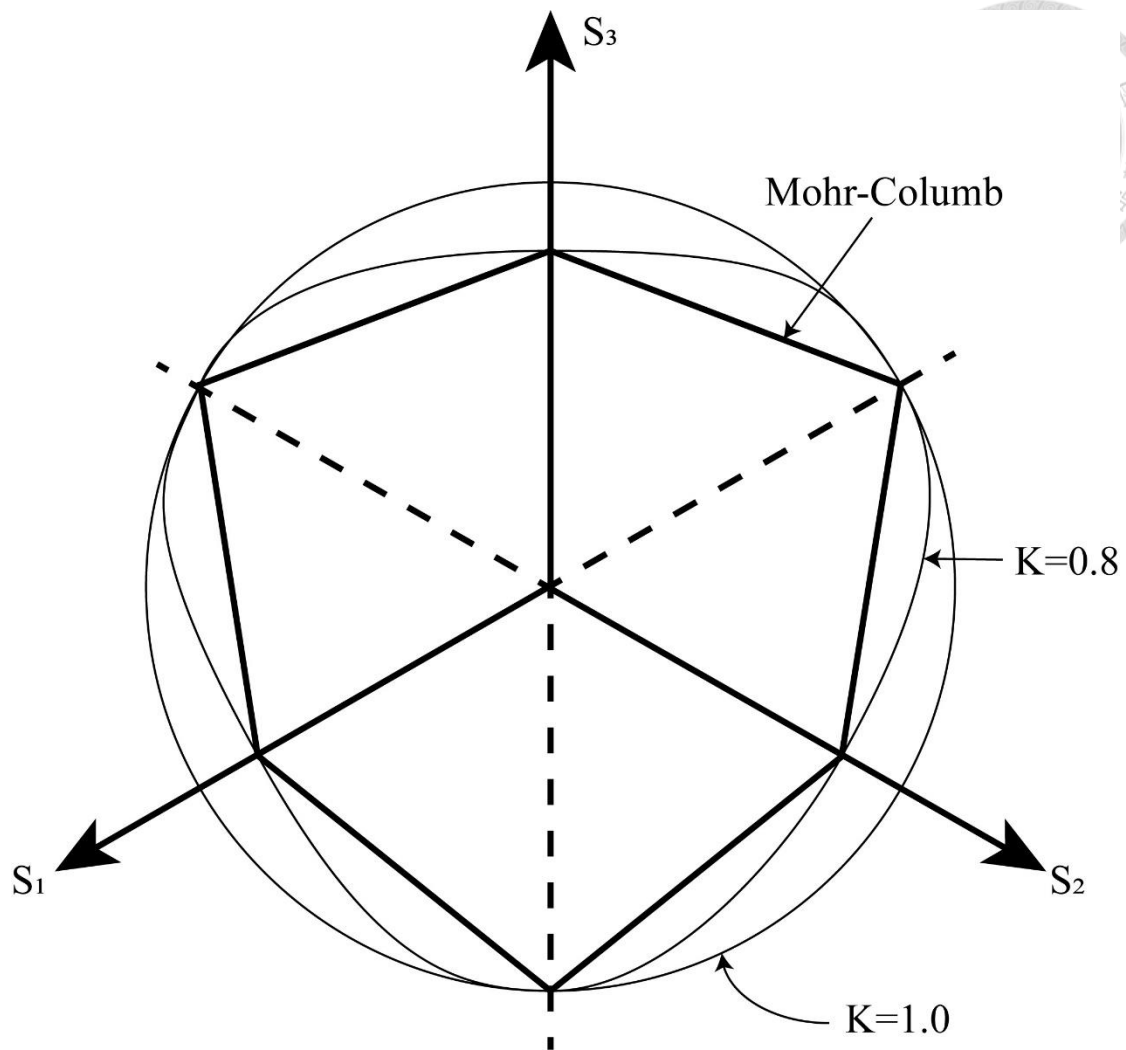
Figure 3-12. Extended Drucker-Prager yield criterion in Abaqus and Mohr-Coulomb criterion on the deviatoric plane.

3.2.1 Shear Strength Reduction Analysis

FEM models of slopes are established based on the elastic behavior in this study. The elastic behavior of the material in a slope is assumed to be linear elastic which is defined by the Young's modulus, E, and the Poisson's ratio, υ.

The Mohr-Coulomb failure is chosen to simulate the plastic behavior of the material in slope and follows the eq. 3-26. The shear strength reduction

50

(SSR) technique (Zienkiewicz et al. 1975; Griffiths and Lane 1999; Griffiths and Marquez 2007; Liu et al. 2015) is adopted to determine the factor of safety (FOS) of a slope. The shear strength parameters in the Mohr-Coulomb failure criterion shown in eq. 3-26 are divided by a series of strength reduction factors (R) until the slope failure starts.

$$c_R = \frac{c}{R}; \ \tan \phi_R = \frac{\tan \phi}{R} \qquad \text{(Eq. 3-45)}$$

While the failure starts during shear strength reduction, the corresponding value of R equals to the factor of safety (FOS). Various shear strength reduction strategies may influence the estimated FOS values (Pantelidis and Griffiths 2013; Zhao et al. 2015). The definition of a slope failure is the key issue in the shear strength reduction analysis and different criterions are proposed (Zienkiewicz et al, 1975; Matsui and San, 1992; Dawson et al.,1999; Griffiths and Lane,1999; Kanungo et al., 2013). In this study, the criterion of slope failure is followed the concept introduced by Dawson et al. (1999). In this criterion, the non-convergence of the solution was the symptom of the initial failure, and then the distribution of strain accumulation

51

3.2.3 Interpretation of landslide sliding surface

From the numerical modeling or remote sensing, the ground deformation would also be estimated. In a 2D-profile, the deformation can be expressed as a function related to the spatial distribution, and the displacement vector consists of two components in horizontal and vertical direction.

$$\vec{D}(x, y) = u(x, y)i + v(x, y)j \qquad \text{(Eq. 3-46)}$$

D: displacement vector

u: horizontal displacement

v: vertical displacement

If the surface deformation is only considered, the variation of deformation with depth could be ignored, and eq. 3-41 could simplified as:

$$\vec{D}(x) = u(x)i + v(x)j \qquad \text{(Eq. 3-47)}$$

Therefore, two fitting curves of displacement could be derived. One curve is to fit the horizontal displacement, and the other one is to fit vertical displacement. In this study, the fitting curve is applied as a boundary condition in the numerical simulation. From the deformation in the FEM analysis, the geometry of landslide slip surface could be roughly estimated.

3.2.4 Models in Numerical Simulation
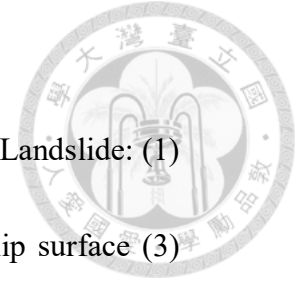
There are three models applied to simulate the Yucheliao Landslide: (1) Slope with homogeneous rock (2) Slope with pre-existing slip surface (3) Slope with layered rock (Fig. 3-13). The geometry of these models is 2D-section along AA' in Figure 2-4. The height of the slope model is 350 m, and the width is 1100 m.

In model (1), the slope is composed of homogenous sandstone, and this model is aimed to roughly characterize the behavior of a rock slope. Model (2) follows the concept of slope stability analysis by Lin et al. (2014). In this model, the pre-existing failure surface is defined. Model (3) are based on the borehole data of B03 shown in Figure 2-4, and sandstone-shale interlayering is adopted instead of pre-existing failure surface.

There are five parameters of each material defined in the numerical simulation: Young's modulus, Poisson ratio, density, cohesion, and internal friction angle. Parameters of sandstone and shale are based on the artificial rocks by Wang (2000). For material applied for failure surface, Young's modulus and Poisson ratio are based on the fault rocks by Isaacs et al. (2008), and other parameters are based on slip surface by Lin et al. (2014). The parameters applied in the modeling are shown in Table 3-1.

(a)

Sandstone

200 m

(b)

Sandstone

Slip surface

200 m

(countune)

54

(c)

Sandstone
Shale

Borehole

200 m
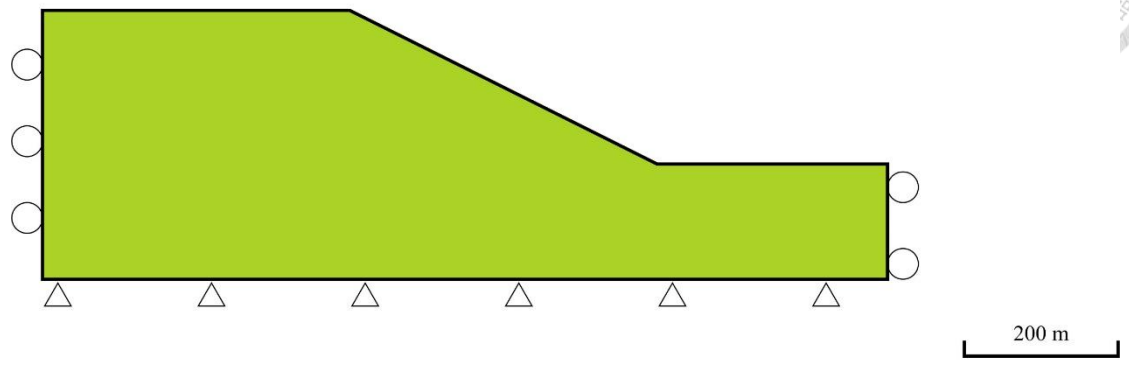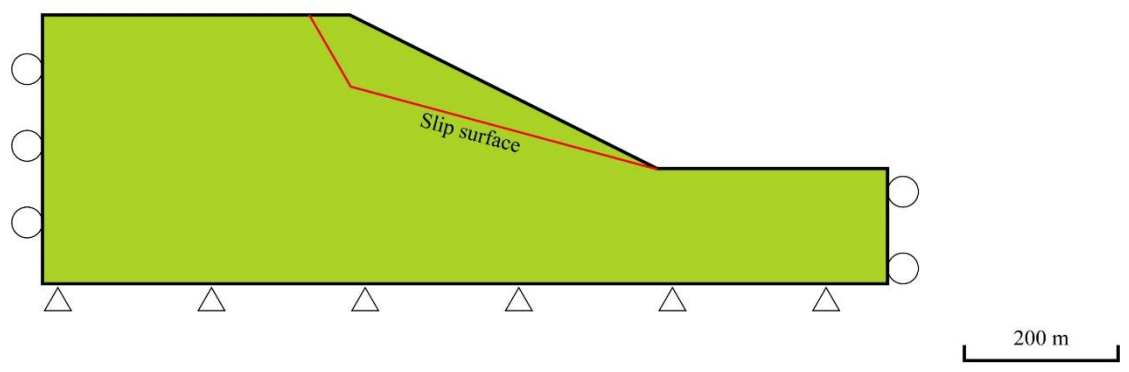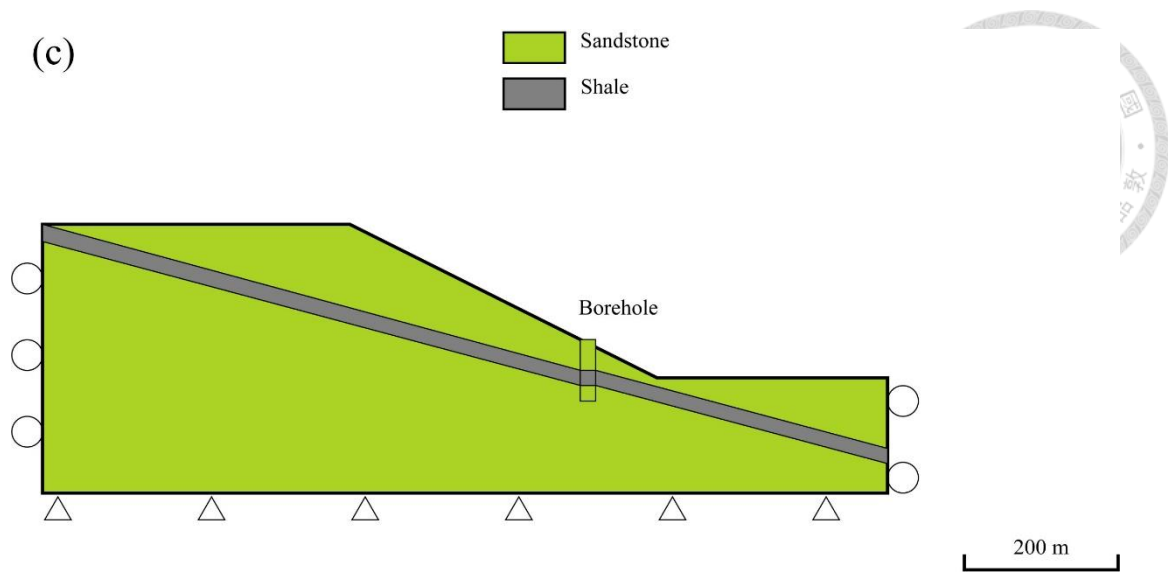
Figure 3-13. Slope models of the Yucheliao Landslide for numerical simulation. (a) Model (1): slope with homogenous sandstone. (b) Model (2): slope with pre-existing slip surface. (c) Model (3): slope with sandstone-shale interbedding.

Table 3-1. Parameters applied in Abaqus.

	Sandstone	Shear zone	Shale
Young's modulus, E (GPa)	1.84	16.2	1.3
Poisson ratio, ν	0.34	0.263	0.21
Unit weight, (kN/m^3)	17.4	20.59	18.1
Cohesion, c (kN/m^2)	2100	98.06	2300
Internal friction angle, φ (°)	34	20	16

4. Results

4.1 PIV analysis

In the PIV analysis, directions and magnitude of displacement of the Yucheliao Landslide were calculated and described. The analyzed cases include the time interval through Typhoon Morakot and the time interval before Typhoon Morakot.

4.1.1 Pre-event: Before Typhoon Morakot

In the time interval of pre-event, 2001/01/17 ~ 2007/01/29 was chosed. Displacement vectors in frame A revealed by the PIV analysis are shown near the Yucheliao Landslide. (Fig. 4-1). The displacement magnitude ranges from 0 to 17 m. The largest magnitude is about 17.11 m, and average magnitude is about 5.52 m. Both slip direction and distribution of the Yucheliao Landslide are hardly defined (Fig. 4-2 and 4-3). Similarly, displacement vectors shown within frame B displays no significant displacement in the pre-event pair (Fig. 4-4 to 4-6).

56

Figure 4-1. Vector map of the pre-event pair derived from the PIV within frame A.

57

Figure 4-2. Scatter map of displacement vectors in the pre-event image pair within frame A.
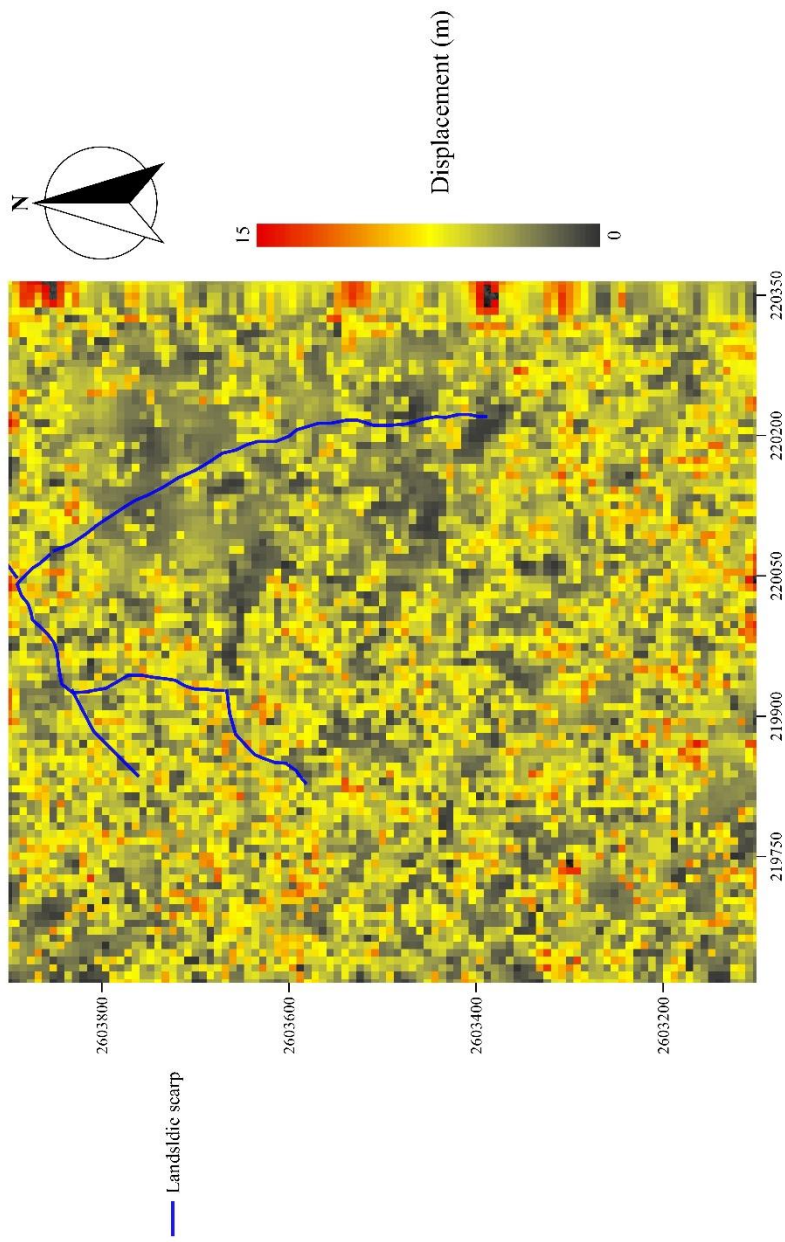
Figure 4-3. The magnitude of displacement in the pre-event pair within frame A.
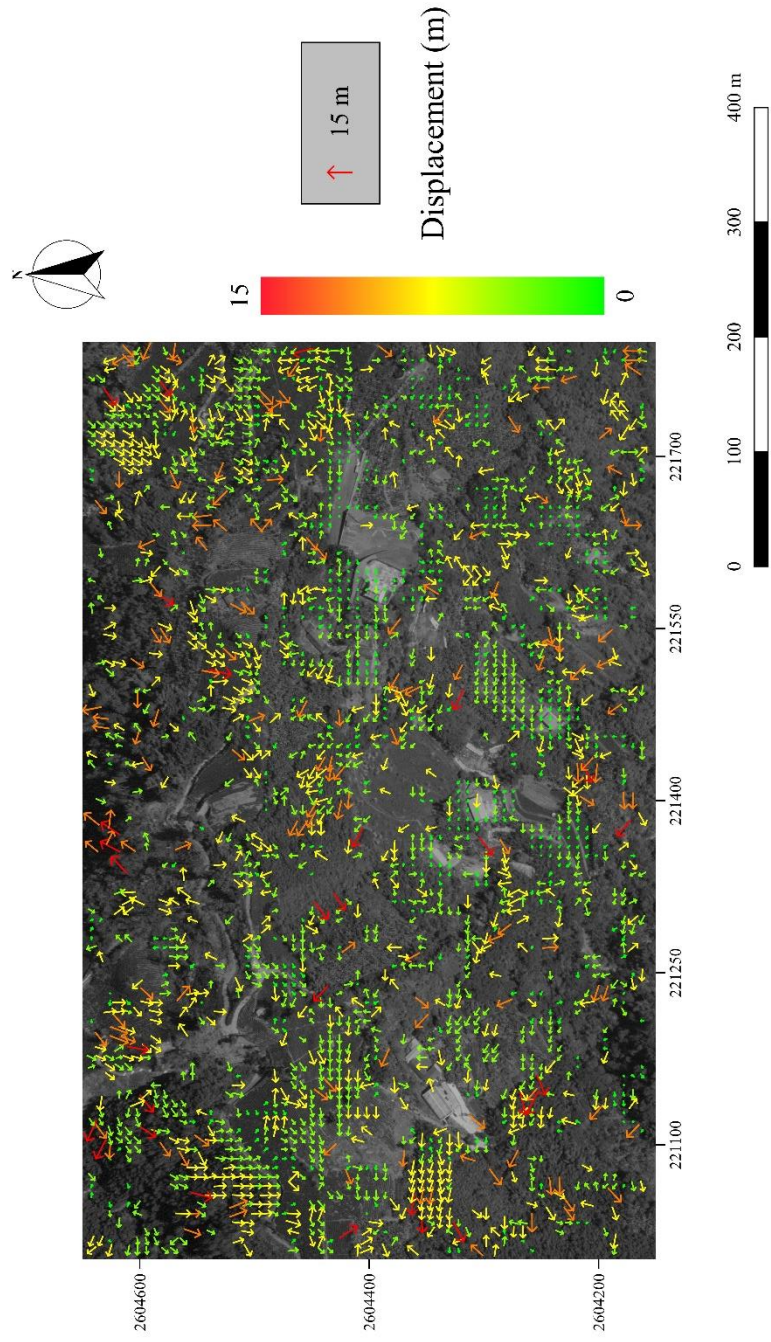
Figure 4-4. Vector map of the pre-event pair derived from PIV within frame B.

60
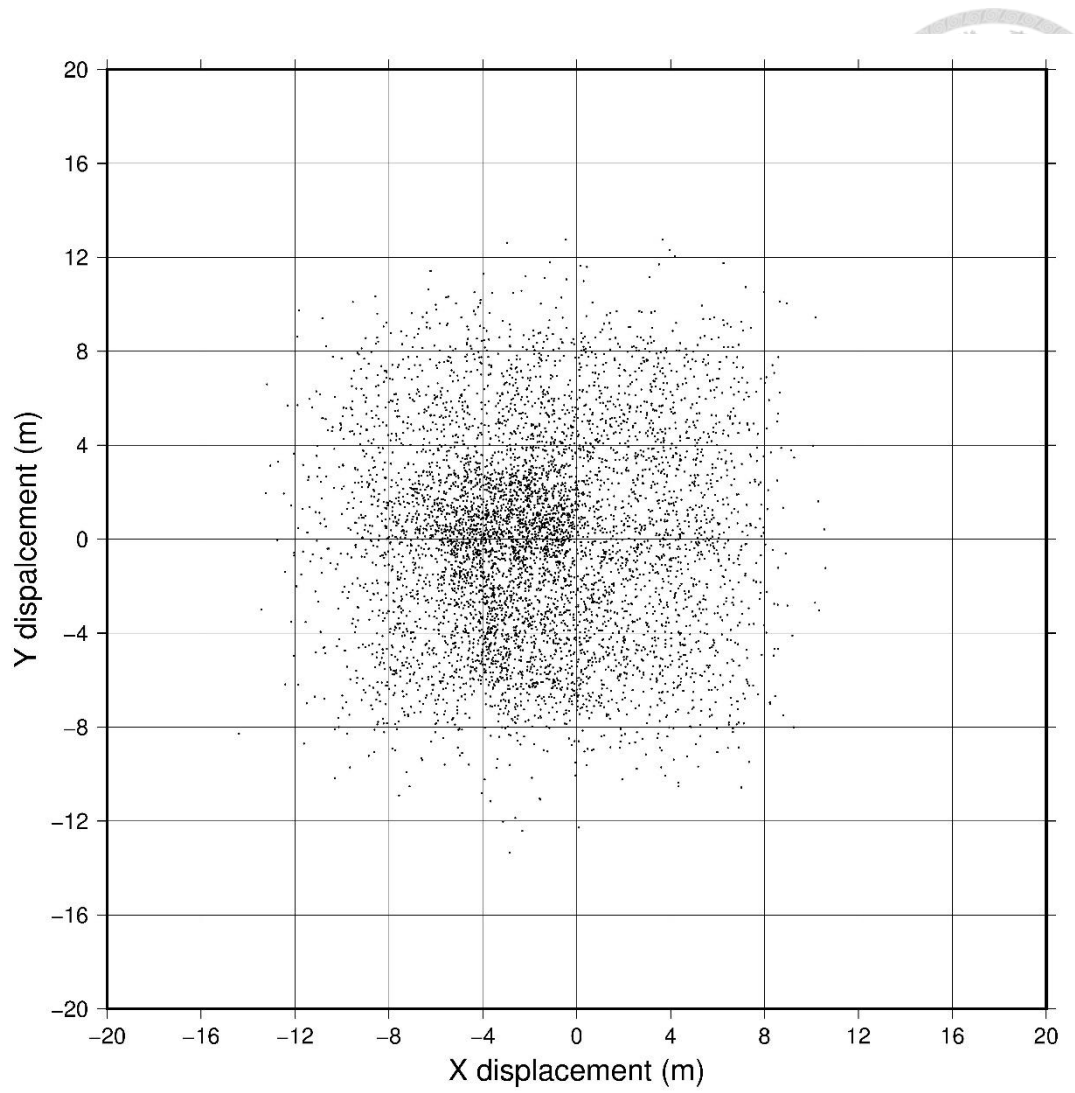
Figure 4-5. Scatter map of displacement vectors in the pre-event image pair within frame B.
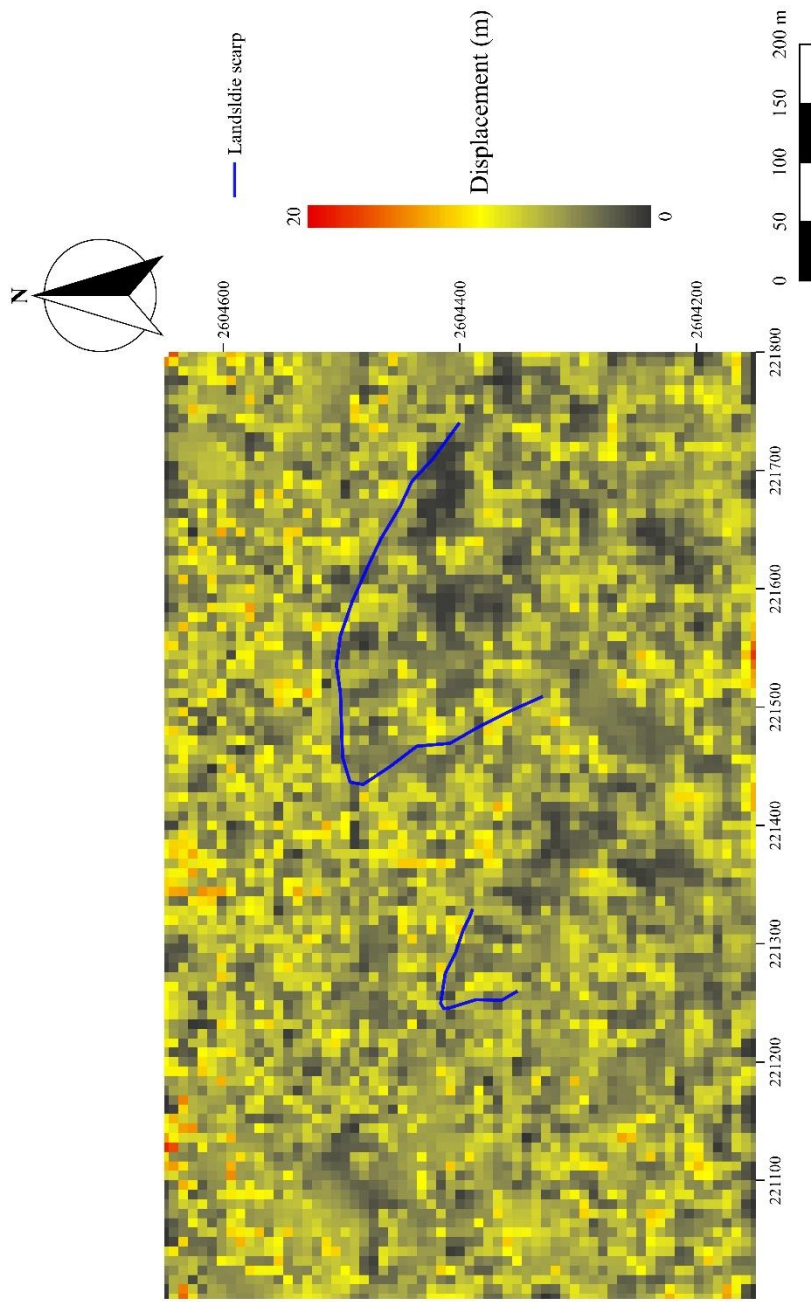
Figure 4-6. The magnitude of displacement in the pre-event pair within frame B.

4.1.2 Post-event: Through Typhoon Morakot

The image pair of the post-event were taken on 2007/01/29 and 2009/08/24, relatively. The time interval through this image pair crosses when Typhoon Morakot hit. In the image taken on 2009/08/24, the main scarp and lateral scarp can be observed in frame A and frame B. From the PIV analysis, the displacement of the Yucheliao Landslide is revealed (Fig 4-7). Within frame A, the maximum of magnitude derived from the PIV analysis is about 120 m, and the average is 32.61 m. Displacement vectors of the block is near the recorded data in the previous studies. The direction of displacement within the landslide body is mainly south (Fig. 4-8), which matches the direction after the landslide triggered. The higher magnitude is roughly concentrated in the landslide region (Fig. 4-9). Within frame B, the vector map does not show the displacement in a uniform direction (Fig. 4-10 and 4-11), and the higher magnitude is also roughly concentrated in the landslide region (Fig. 4-12).
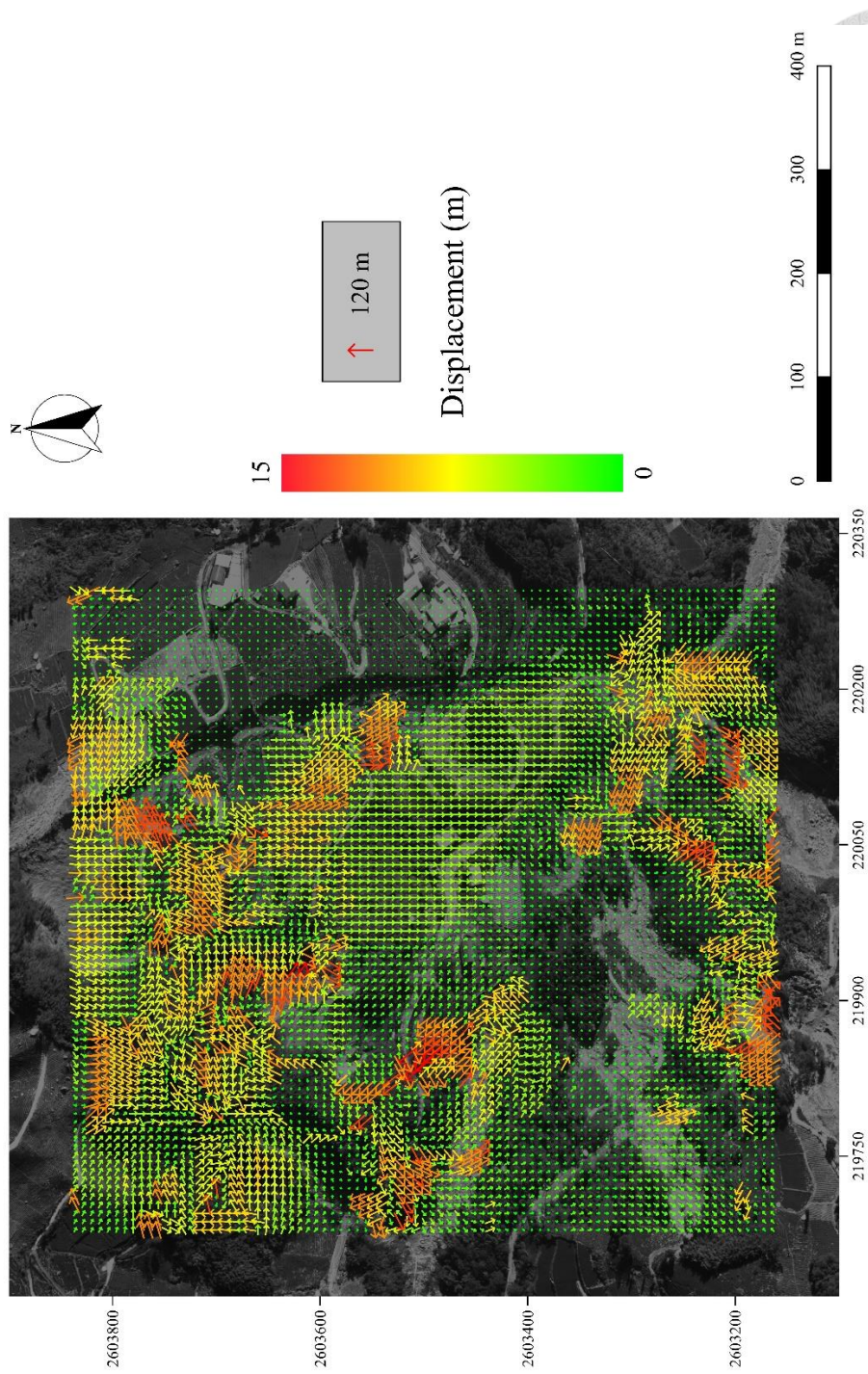
Figure 4-7. Vector map of the post-event pair derived from PIV within frame A.

64
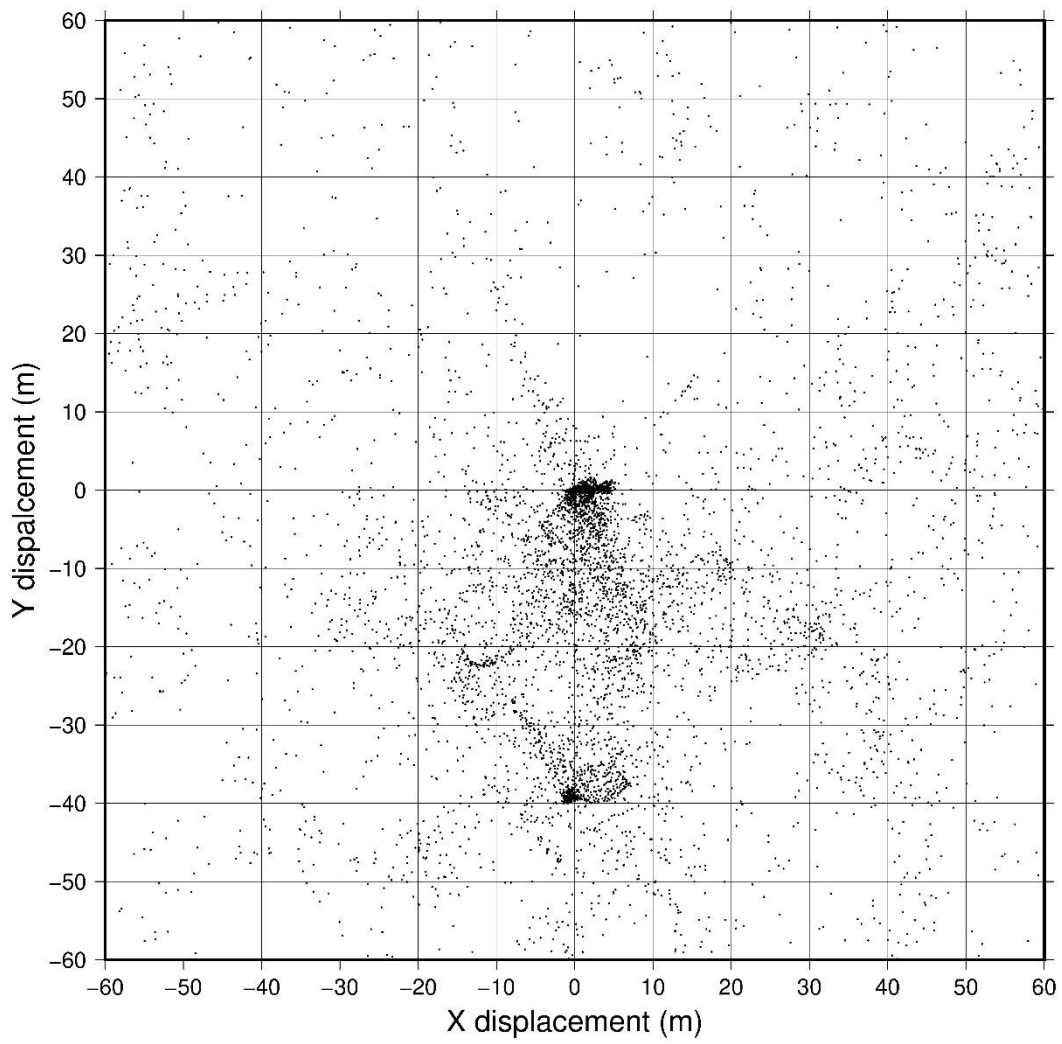
Figure 4-8. Scatter map of displacement vectors in the post-event image pair within frame A.
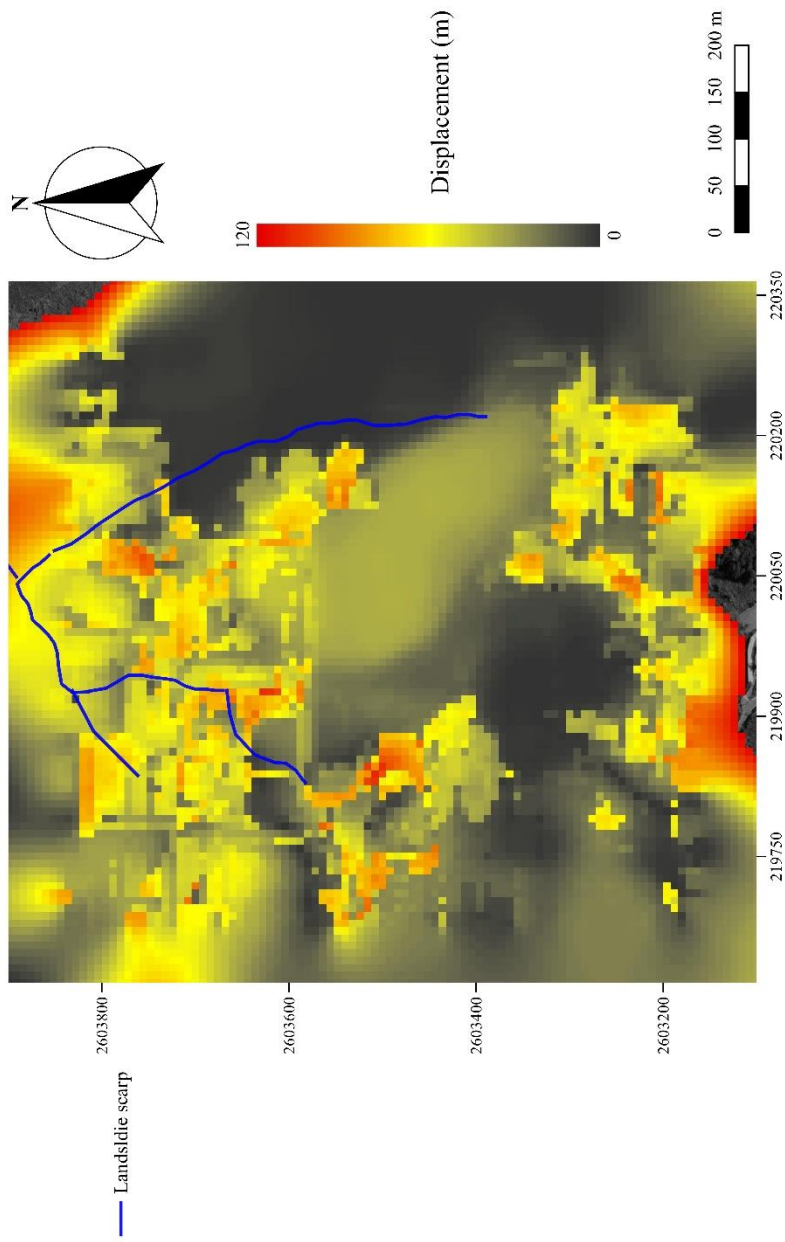
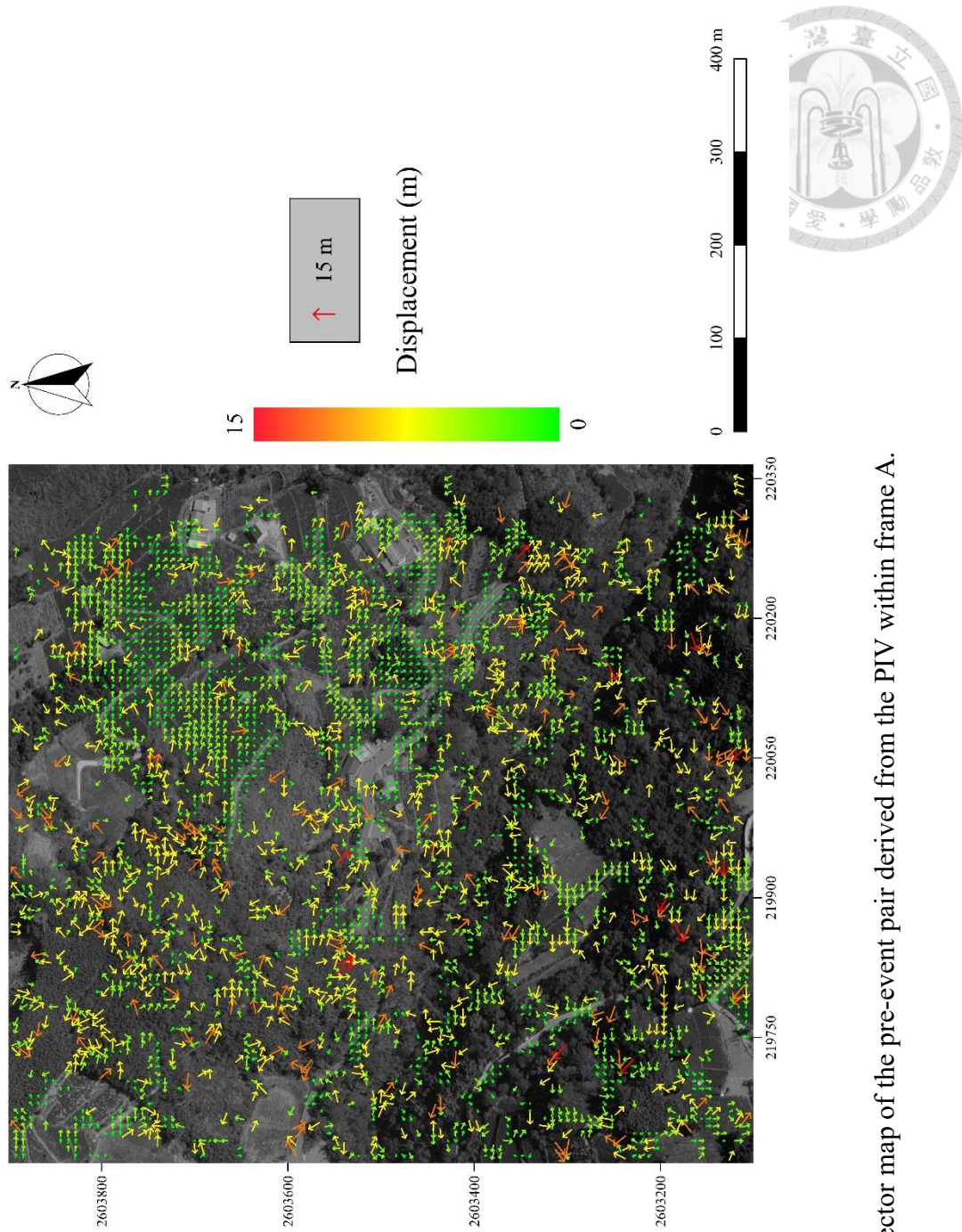**Figure 4-9.** The magnitude of displacement in the post-event pair within frame A.

66
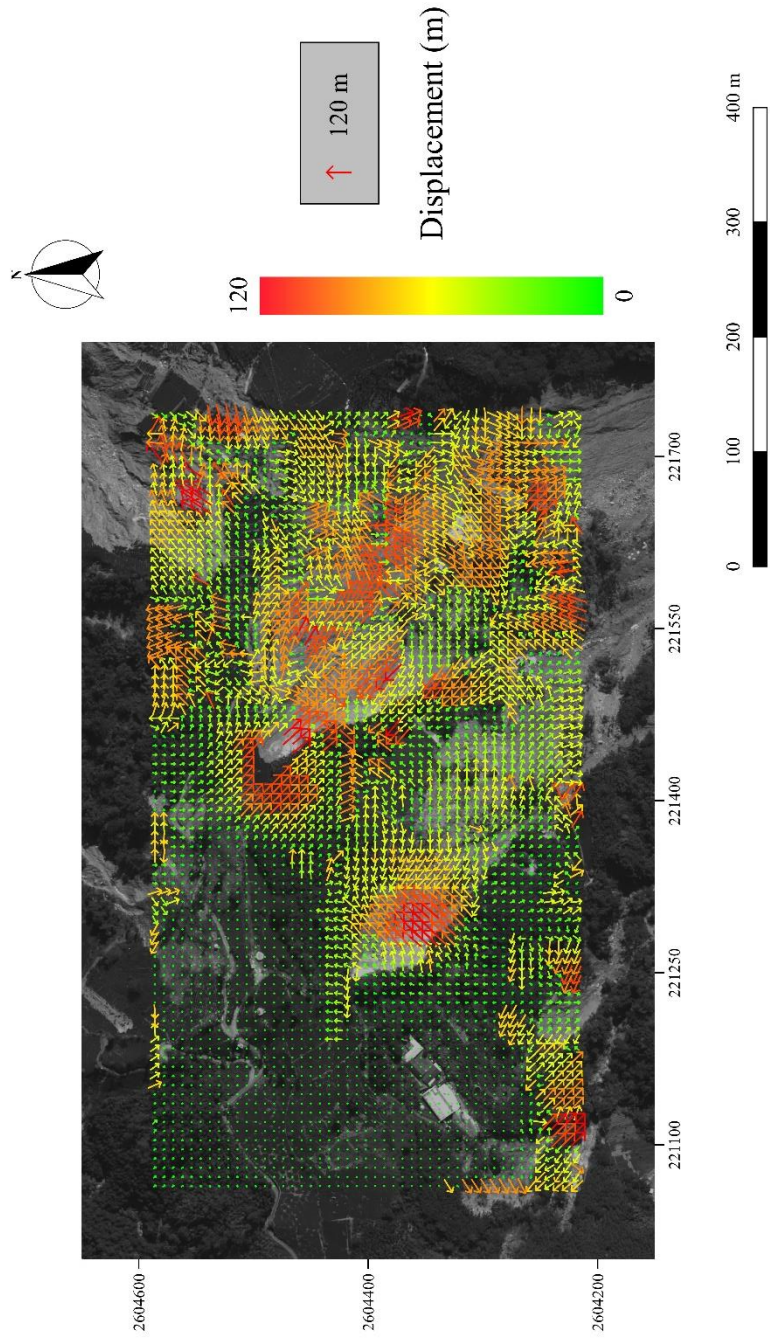
Figure 4-10. Vector map of the post-event pair derived from PIV within frame B.
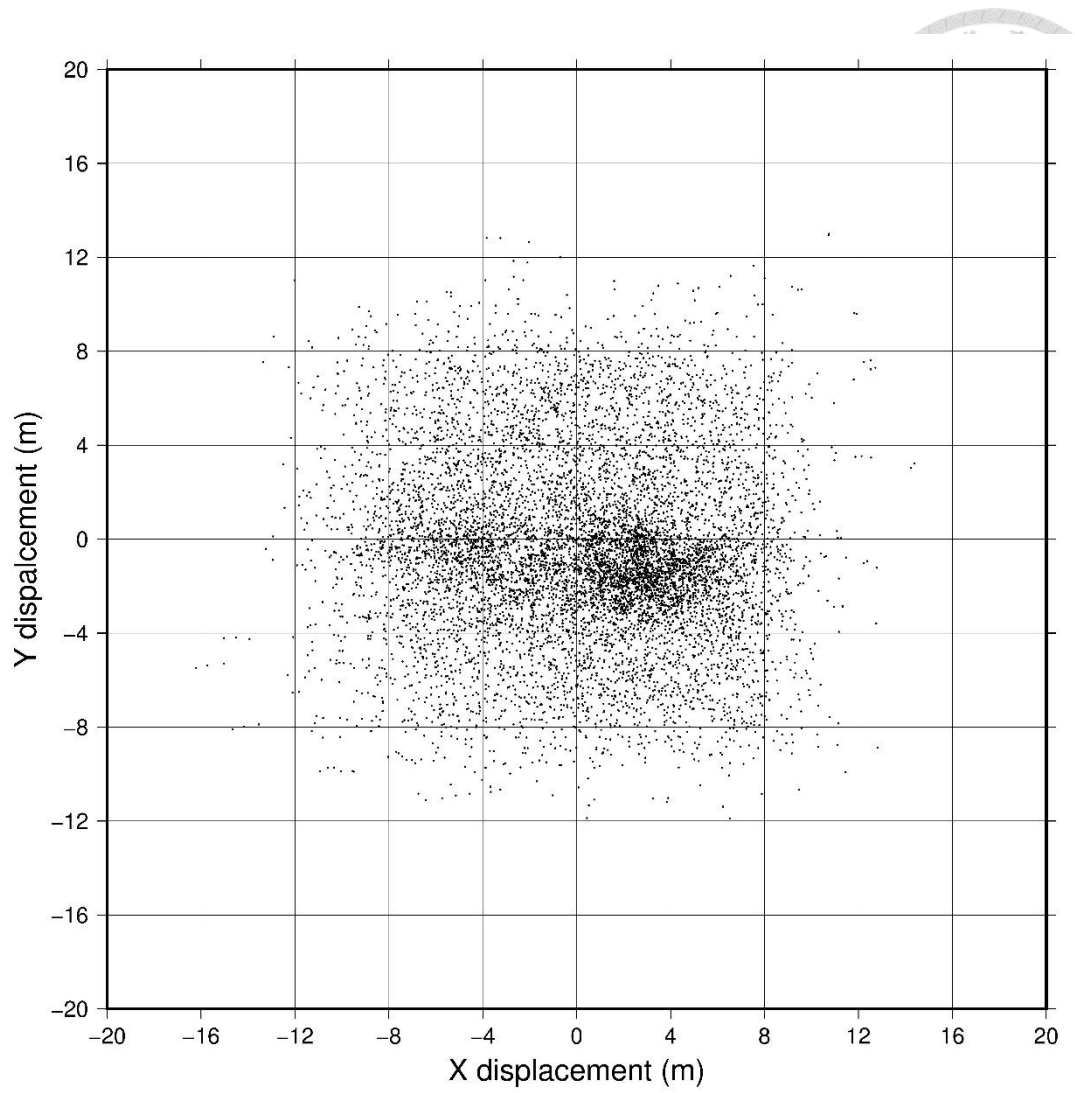
67
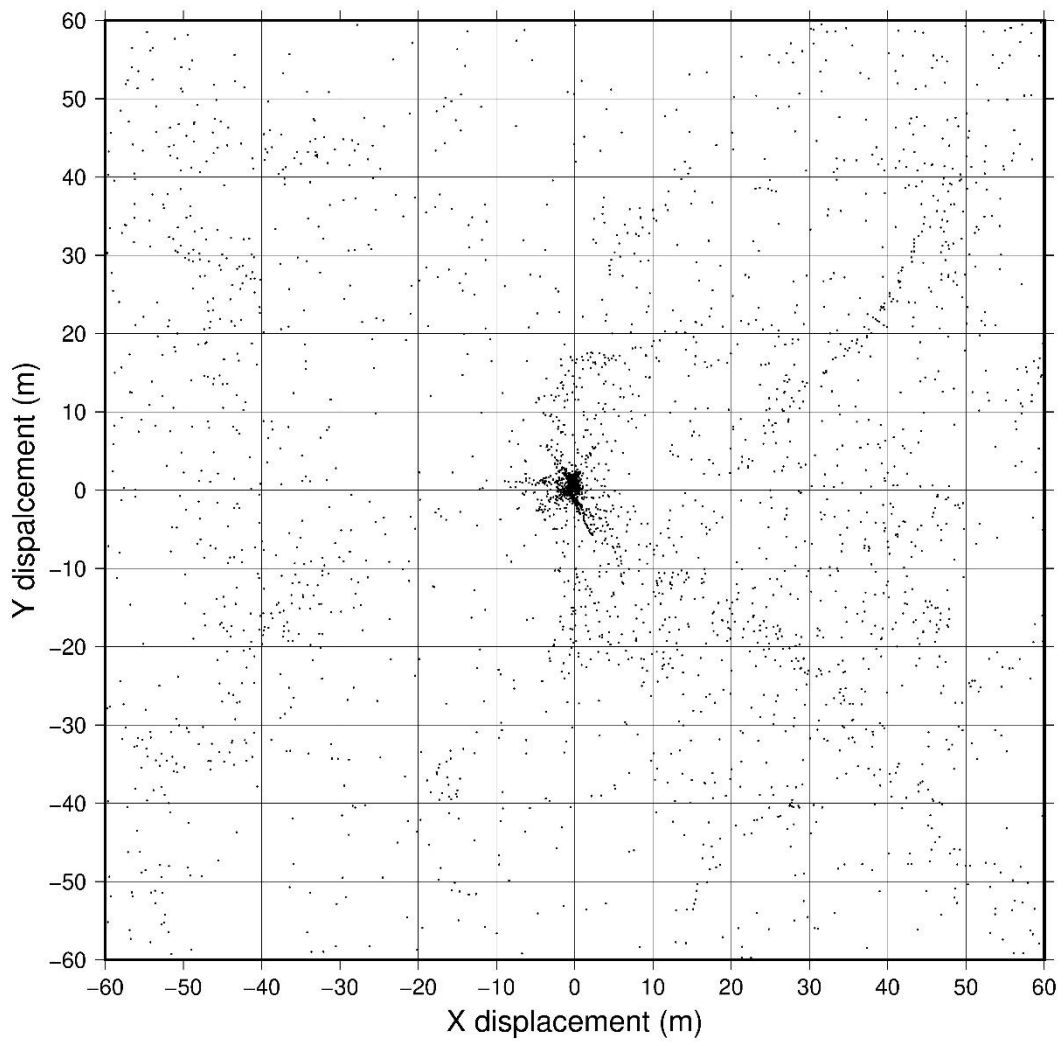
Figure 4-11. Scatter map of displacement vectors in the post-event image pair within
frame B.

68
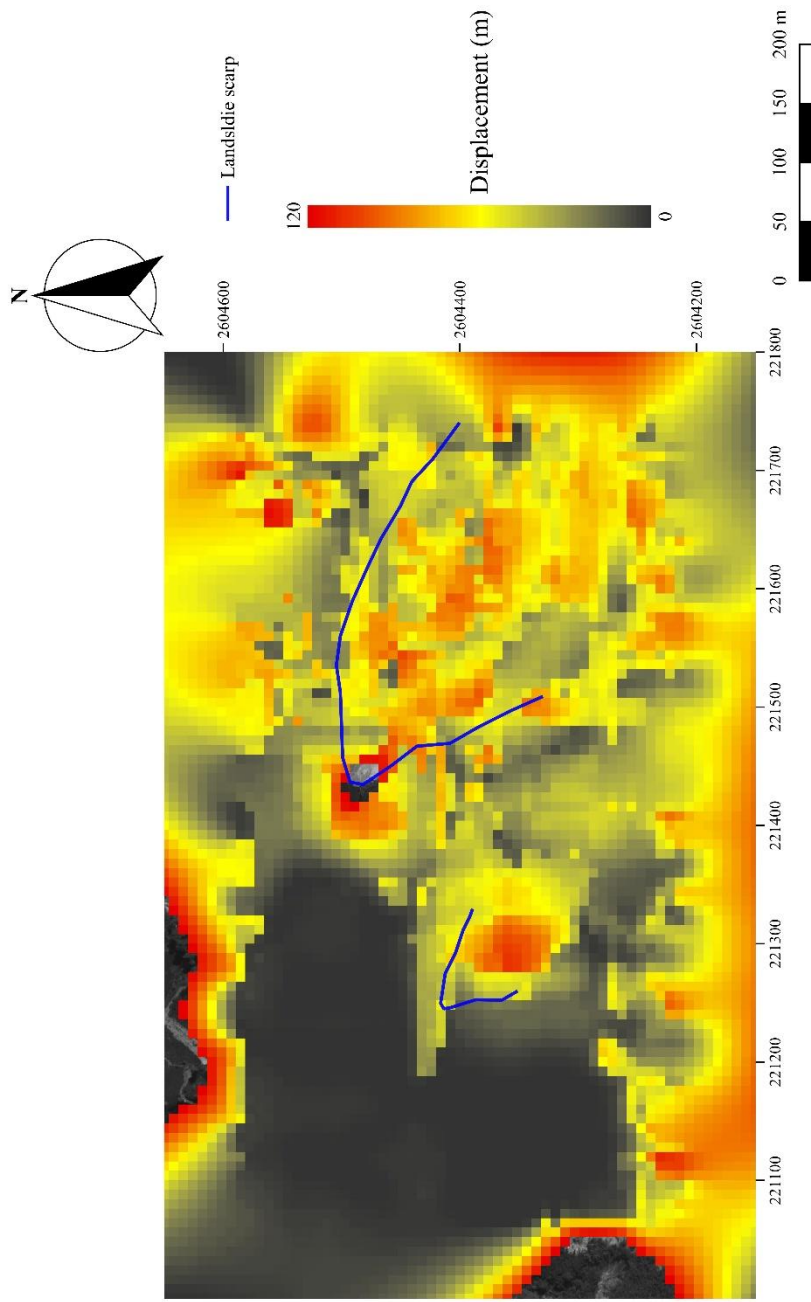
Figure 4-12. The magnitude of the displacement in the post-event pair within frame B.

4.2 Numerical modeling

In the numerical modeling, three models are introduced for the slope stability analysis by the FEM based shear strength reduction method (Fig. 3-13). Then, the displacement along the slope surface would be set as the boundary condition in the FEM analysis to interpret the potential slip surface of the landslide.

4.2.1 Model (1): Slope with homogeneous rock

In model (1), the factor of safety derived from the shear strength reduction method is about 6.53 (Fig. 4-13). From the displacement map, it is estimated that a circular failure will develop in model (1) and the depth of slip surface is about 80 m (Fig. 4-14). The magnitude of displacement along the slope surface is shown in Figure 4-15. Figure 4-16 shows the X distance shown in Figure 4-15. Then, curves in Figure 4-15 is set as a boundary condition in the static analysis of the FEM, and the distribution of displacement displays the potential slide area (Fig. 4-17). Comparing with the result from the shear strength reduction, the geometry of failure surface is also a circular surface. However, the estimated depth is about 50 m and obviously less than the previous result.

70
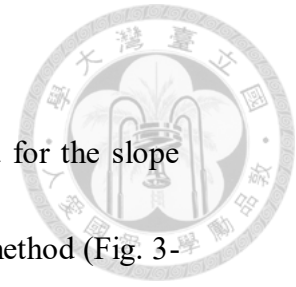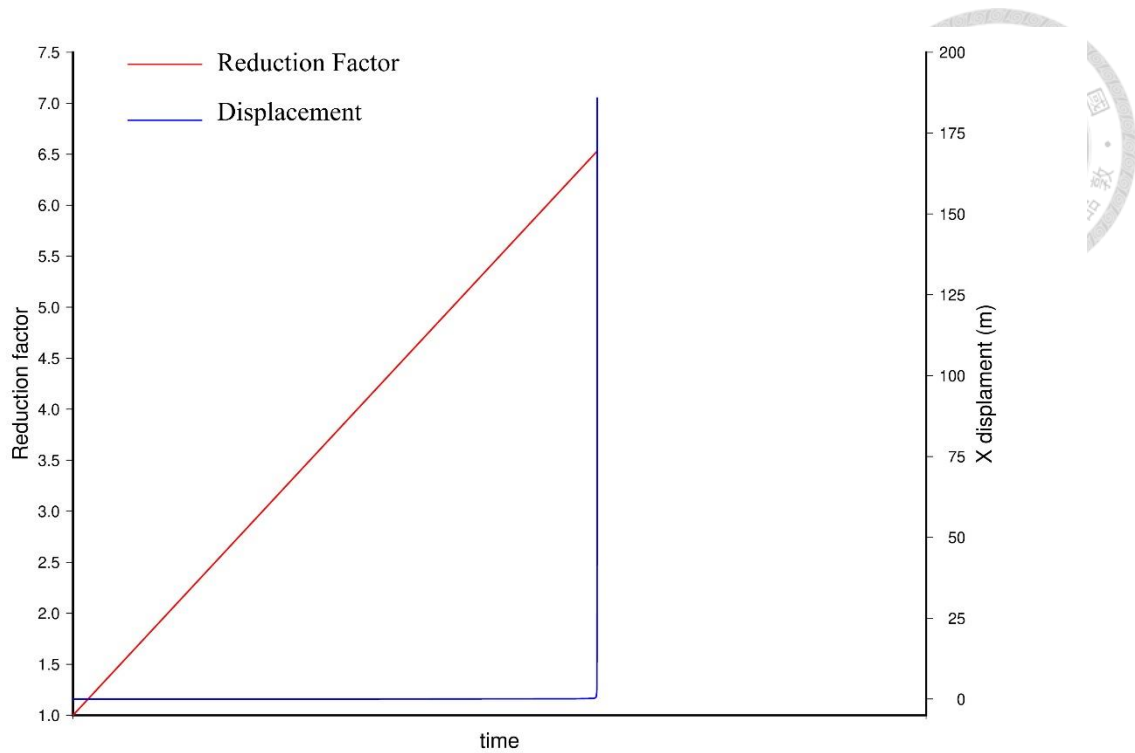
Figure 4-13. The reduction factor – displacement curve of model (1).
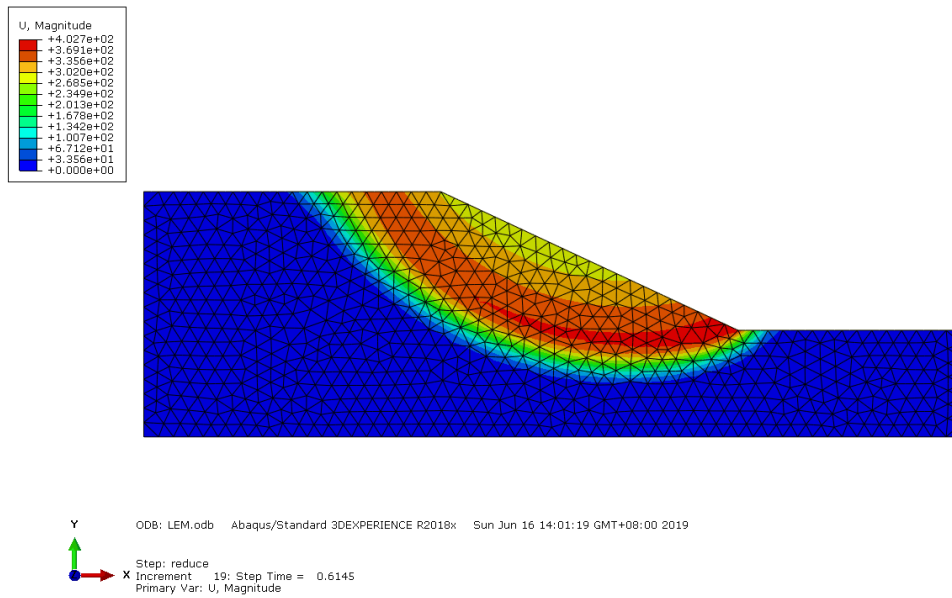
Figure 4-14. Displacement contour map of model (1). Unit for the displacement is meter in the legend.
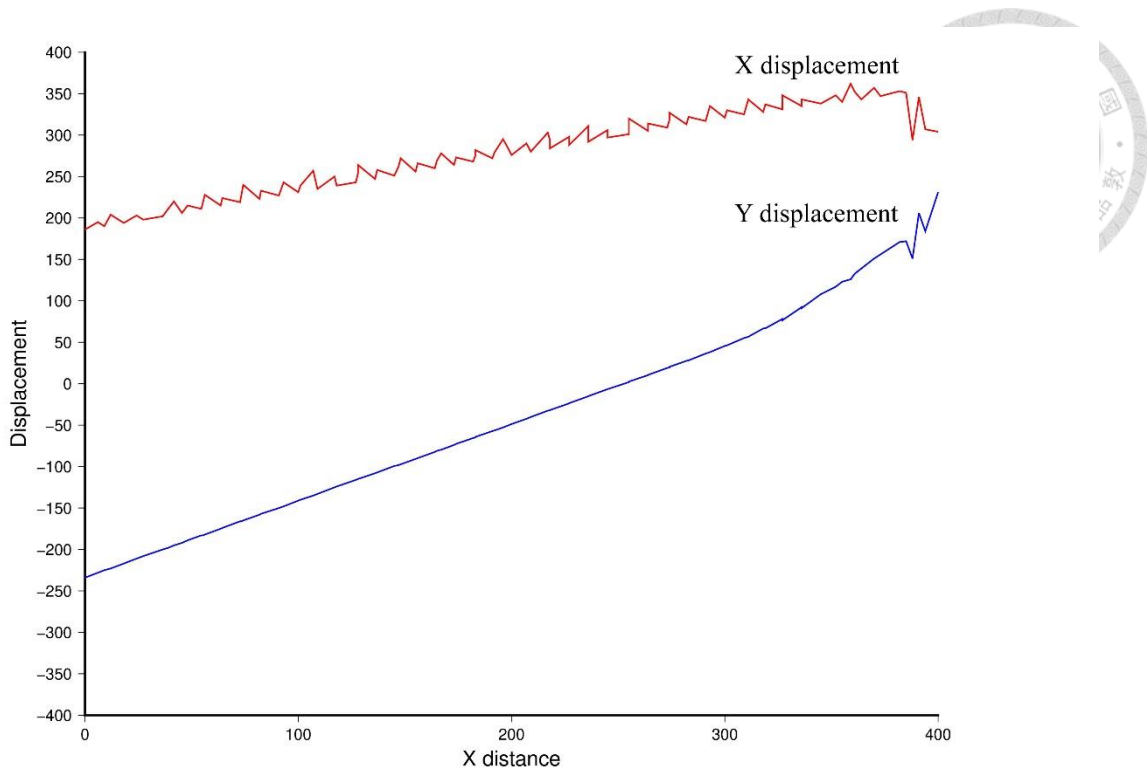
Figure 4-15. Displacement curves along slope the surface in model (1)
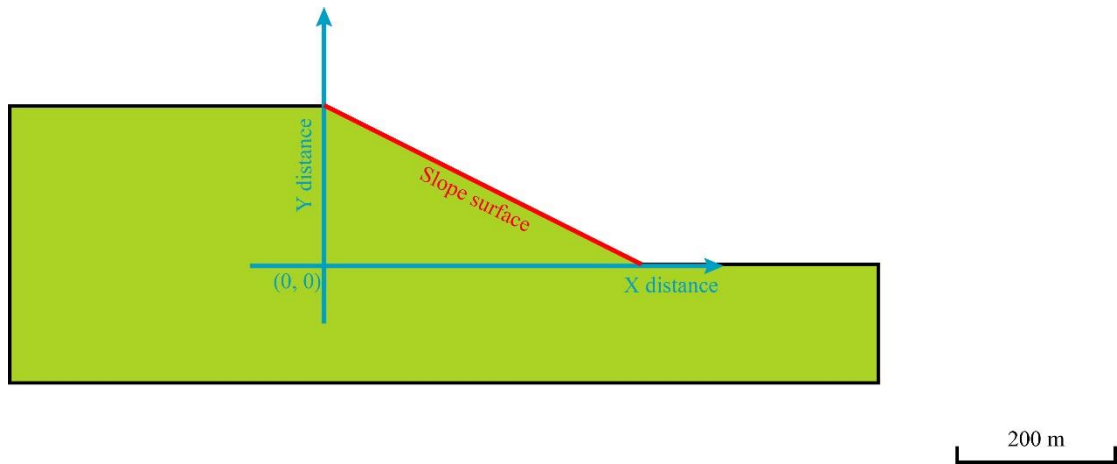
Figure 4-16. The axis of X distance and Y distance in the slope model. The length of the slope surface in X direction is 400 m.

72

U, Magnitude
+1.487e+00
+1.363e+00
+1.239e+00
+1.115e+00
+9.911e-01
+8.672e-01
+7.433e-01
+6.194e-01
+4.955e-01
+3.716e-01
+2.478e-01
+1.239e-01
+0.000e+00

Y

X
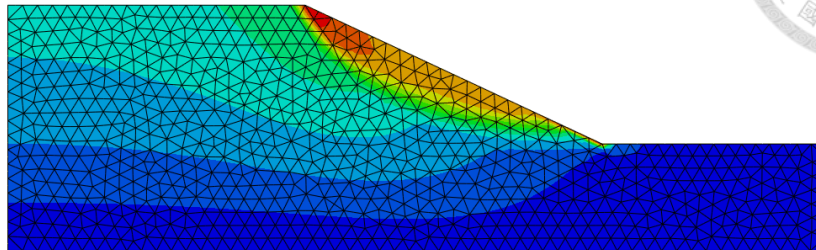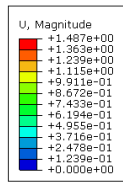
ODB: Deform.odb   Abaqus/Standard 3DEXPERIENCE R2018x   Sun Jun 16 15:39:57 GMT+08:00 2019

Step: deform
Increment   77: Step Time = 8.6532E-02
Primary Var: U, Magnitude

Figure 4-17. Displacement contour map of model (1) when the displacement curve is set as boundary condition.

4.2.2 Model (2): Slope with pre-existing slip surface

In model (2), the factor of safety derived from the shear strength reduction method is about 1.60 (Fig. 4-18). From the displacement map, it is obvious that failure will develop along the pre-existing failure surface in model (2) (Fig. 4-19). The magnitude of displacement along the slope surface is shown Figure 4-20. Figure 4-16 shows the X distance shown in Figure 4-20. Then, curves in Figure 4-20 is set as a boundary condition in the static analysis of the FEM, and the distribution of displacement displays the potential slide area (Fig. 4-21). Comparing with the result from the shear strength reduction, the geometry of failure surface is similar to the result from the shear strength reduction method.

73
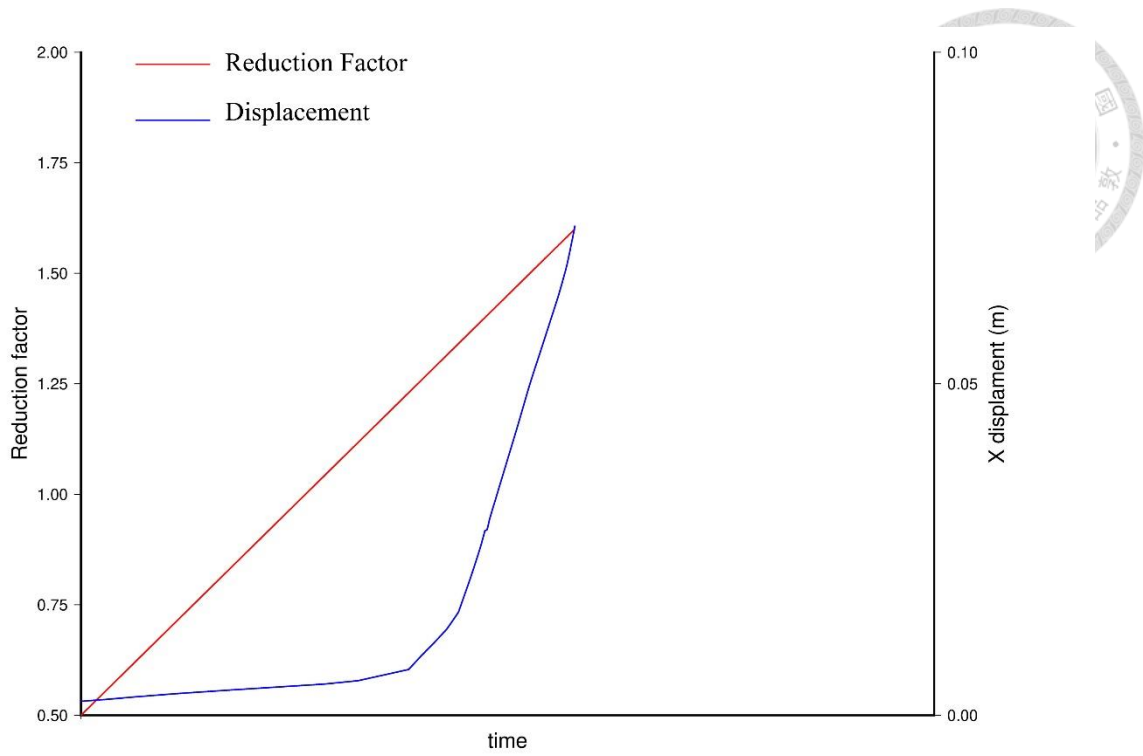
Figure 4-18. The reduction factor – displacement curve of model (2).
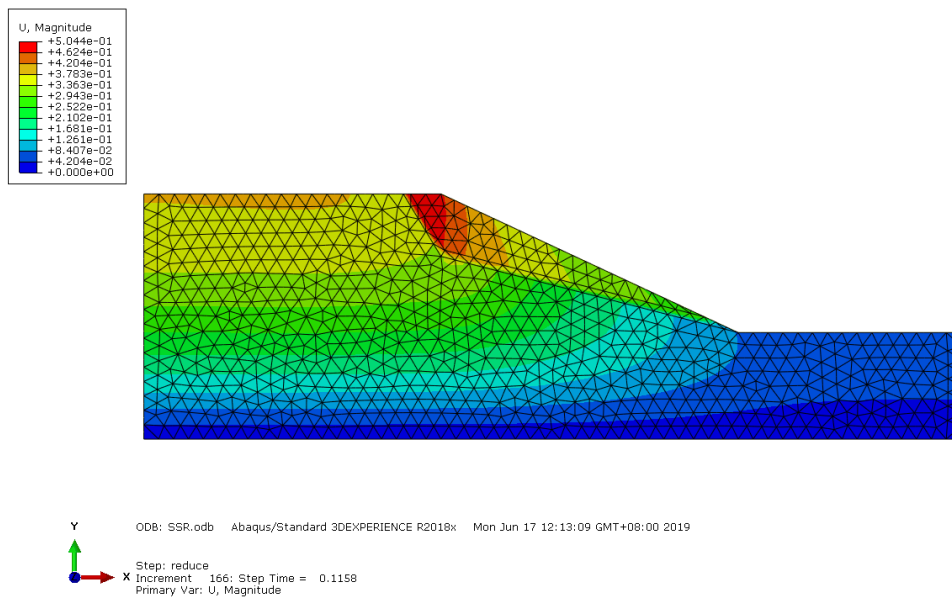
Figure 4-19. Displacement contour map of model (2). Unit for the displacement is meter in the legend.
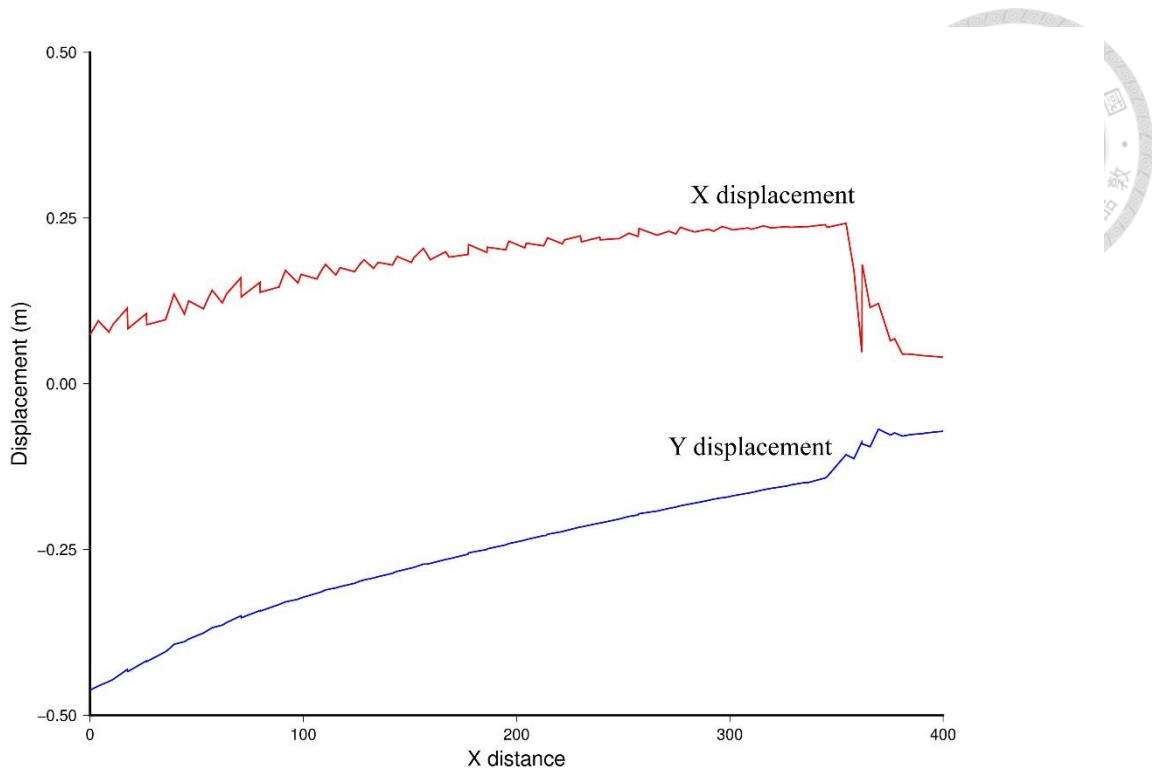
Figure 4-20. Displacement curves along slope surface in model (2)
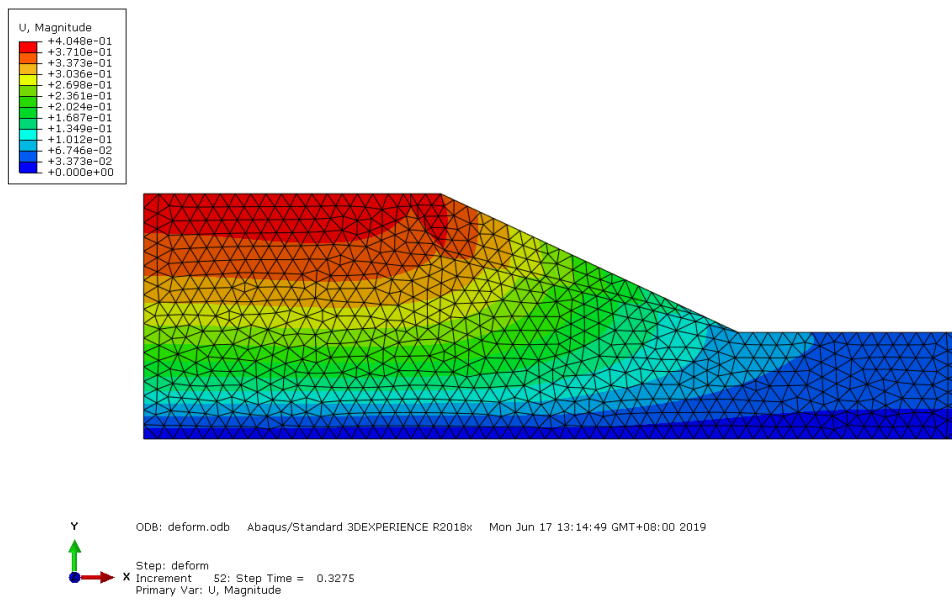
Figure 4-21. Displacement contour map of model (2) when the displacement curve is set as boundary condition.

75

4.2.3 Model (3): Slope with sandstone-shale interbedding

In model (3), the factor of safety derived from the shear strength reduction method is about 6.47 (Fig. 4-22). From the displacement map, it is estimated that a circular failure will develop in model (3) and the depth of slip surface is about 60 m (Fig. 4-23). The magnitude of displacement along the slope surface is shown in Figure 4-24. Figure 4-16 shows the X distance shown in Figure 4-24. Then, curves in Figure 4-24 are set as a boundary condition in the static analysis of the FEM, and the distribution of displacement displays the potential slide area (Fig. 4-25). Comparing with the result from the shear strength reduction, the geometry of failure surface is nearly a planar surface, and the estimated depth is about 40 m.
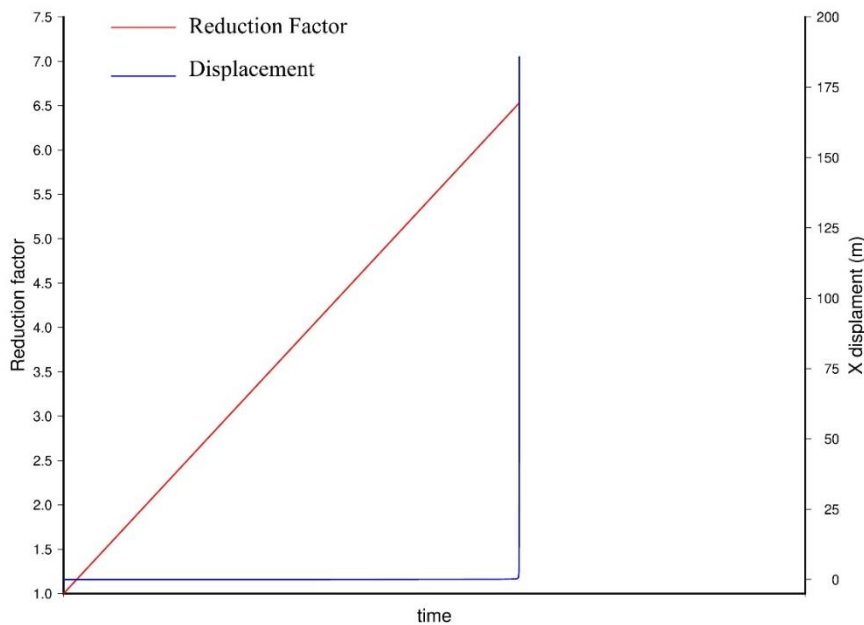
Figure 4-22. The reduction factor – displacement curve of model (3).
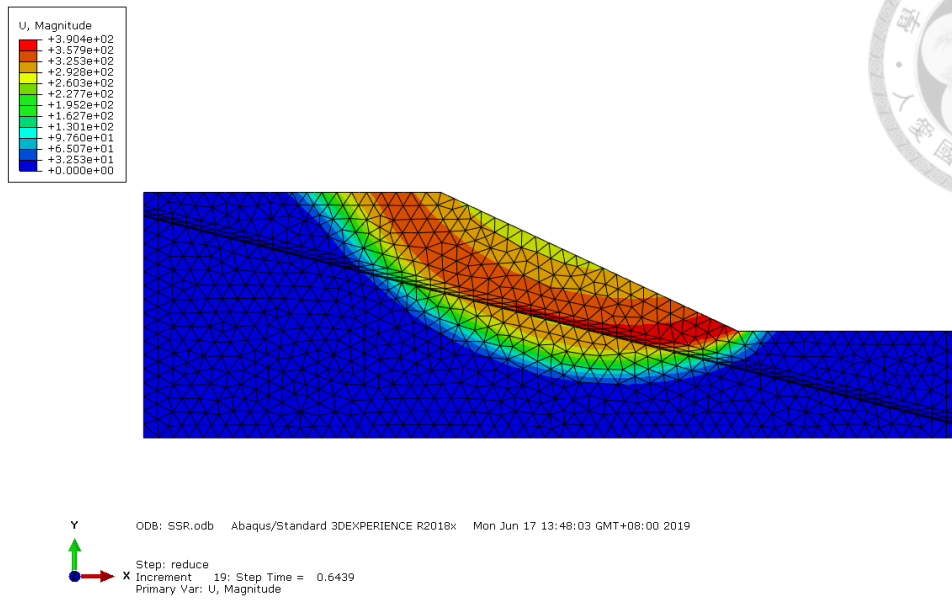
Figure 4-23. Displacement contour map of model (3). Unit for the displacement is meter in the legend.
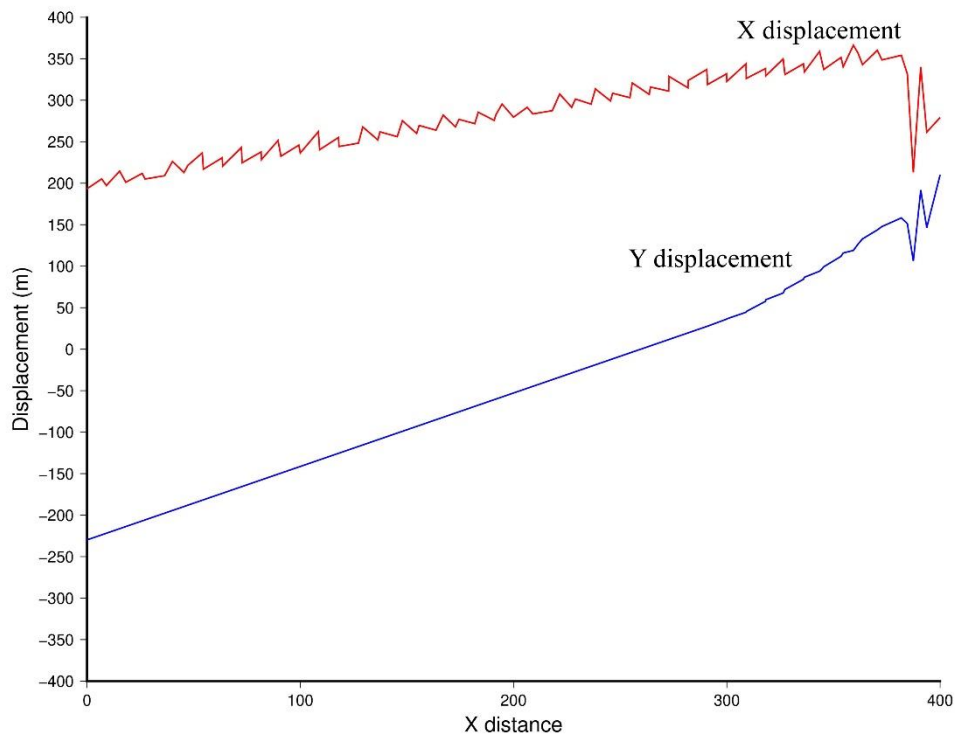
Figure 4-24. Displacement curves along the slope surface in model (3).
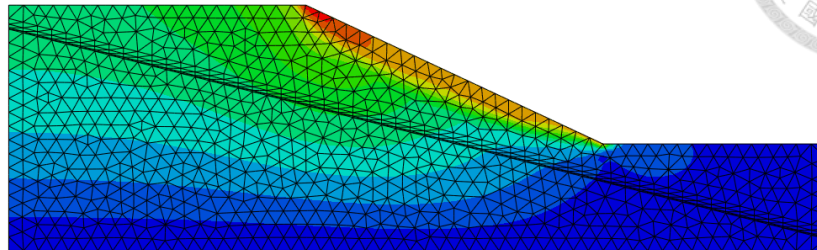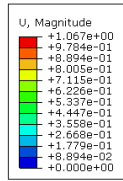
77

Figure. 4-25. Displacement contour map of model (3) when the displacement curve is set as boundary condition.

4.2.4 Interpreting landslide sliding surface from PIV displacement data

The position of numerical model is along the A-A' profile shown in Figure 2-4 and similar to N-S direction. For the boundary condition on the slope surface, the X displacement is set to be 60 m, which is the maximum displacement within landslide block, and Y displacement is set to be 0 m to 30 m, which is based on the height of the main scarp (Fig. 4-26). This boundary condition is applied to model (2) and model (3) in the static analysis of the FEM, and the distribution of displacement displays the potential slide area (Fig. 4-27). The depth estimated in model (2) is about 50 m, and that estimated in model (3) is about 30 m.

78
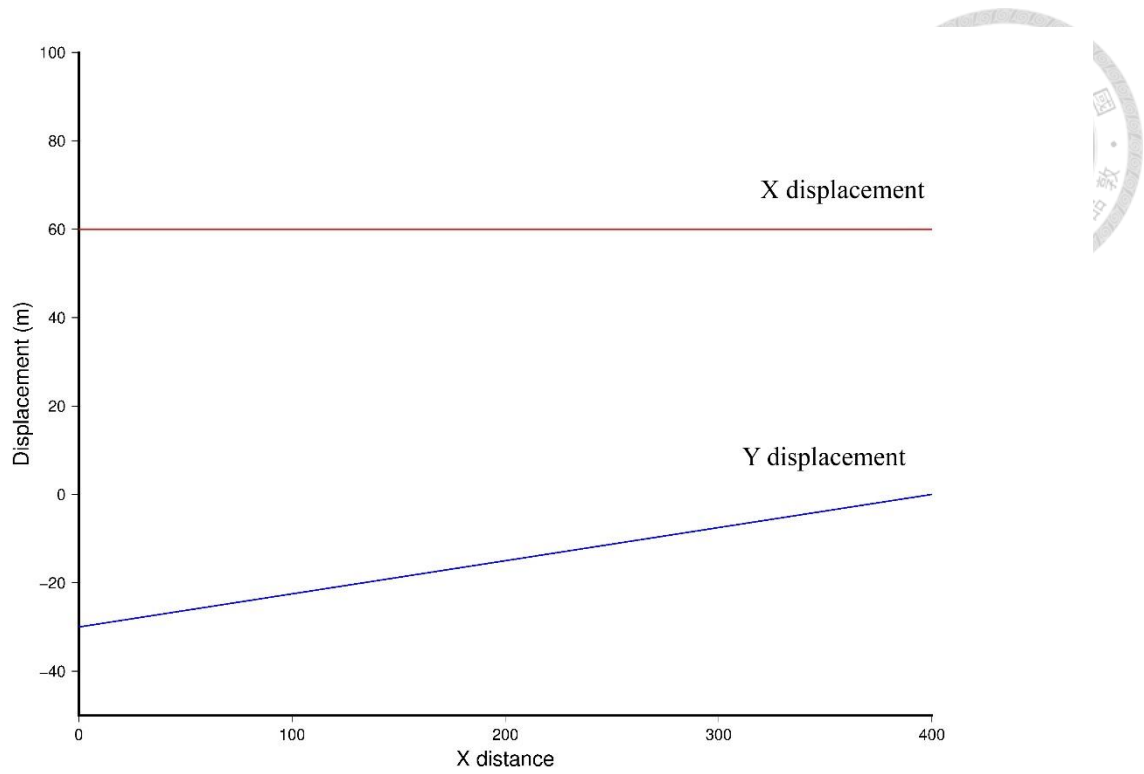
Figure 4-26. Displacement curve applied for interpreting landslide sliding surface.

(a)

U, Magnitude
+3.933e-01
+3.605e-01
+3.277e-01
+2.949e-01
+2.622e-01
+2.294e-01
+1.966e-01
+1.639e-01
+1.311e-01
+9.831e-02
+6.554e-02
+3.277e-02
+0.000e+00

Y
X

ODB: model02.odb   Abaqus/Standard 3DEXPERIENCE R2018x   Mon Jun 17 15:18:16 GMT+08:00 2019

Step: deform
Increment   30: Step Time =   3.6042E-02
Primary Var: U, Magnitude

(b)

U, Magnitude
+1.681e+00
+1.541e+00
+1.401e+00
+1.261e+00
+1.121e+00
+9.808e-01
+8.407e-01
+7.006e-01
+5.605e-01
+4.203e-01
+2.802e-01
+1.401e-01
+0.000e+00

Y
X

ODB: model03.odb   Abaqus/Standard 3DEXPERIENCE R2018x   Mon Jun 17 15:18:21 GMT+08:00 2019

Step: deform
Increment   108: Step Time =   0.2105
Primary Var: U, Magnitude

Figure. 4-27. Displacement contour map in the numerical model when the PIV displacement is set as a boundary condition. (a): PIV displacement applied to model (2). (b): PIV displacement applied to model (3).

80

5. Discussion

5.1 Feasibility assessment on PIV analysis

In the pre-event pair of images, the obvious problem is that the displacement derived from the PIV could not display the distribution of landslide and the slip direction. The displacement derived from the PIV analysis is mainly affected by the size of the interrogation window and correlation between the images in the same pair. Considering the size of the interrogation window, the size of interrogation window is set to be 32 pixels x 32 pixels in pair 1. With small interrogation window, the small displacement of one target (or ground objects) could be detected. However, the displacement derived from small interrogation window is doubted once the target is larger than interrogation window (Fig 5-1). In the contrast, larger window size may include other target and cause errors (Fig 5-1f). Moreover, the displacement would be overestimated in the PIV analysis while larger interrogation window is applied (Table 5-1). Considering the degree of correlation, the peak value of the cross-correlation is estimated as the same object in PIV analysis. However, in the case of change in land cover, the location of peak value would change because the original position is occupied by other thing instead of the original target (Fig. 5-2), and the degree of

81

correlation would decrease. To eliminate the error from change in land cover, filtering the displacement vector with lower correlation is considered.

(a)

(b)

(c)

(d)

(e)

(f)
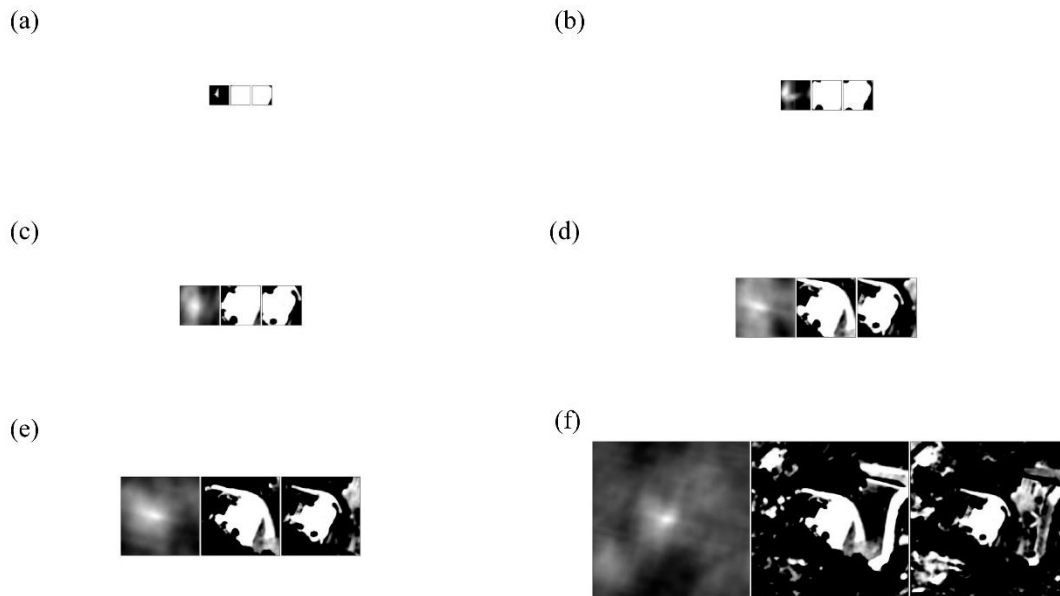
Figure 5-1. Correlation plane of the unmoved construction in different sizes of the interrogation window. (a) 32 pixels x 32 pixels (b) 48 pixels x 48 pixels (c) 64 pixels x 64 pixels (d) 96 pixels x 96 pixels (e) 128 pixels x 128 pixels (f) 256 pixels x 256 pixels.

Window size (pixel)	X displacement (pixel)
32	6.78
48	5.18
64	7.46
96	11.1
128	8.35
256	8.21

Table 5-1. Displacement of the construction in Figure 5-1 derived from different window size in the PIV analysis.
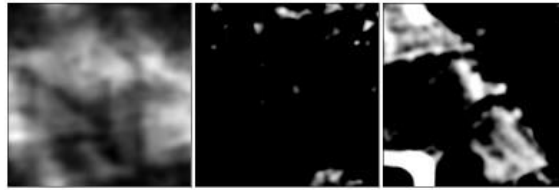
Figure 5-2. Correlation plane of the location where the forest area has been transformed to the farmland.

In the post-event pair, the distribution of landslide region could be roughly determined in the magnitude map, but it is hard to determine the slip direction from the vector map. (Fig. 4-7 to 4-12). Averagely, the degree of correlation is lower in the post-event pair than in the pre-event pair due to severe change in land cover and larger interrogation window size (Fig. 5-3). Change in land cover is mainly caused by erosion when Typhoon Morakot hit and the formation of the landslide scarp. Larger interrogation window is set to detect larger displacement, but the degree of correlation would decrease expectedly. Generally, it is difficult to distinguish the error from change in land cover or size of interrogation window while window size is adjusted to be larger to detect larger displacement. Therefore, once the slip distance of the landslide is large enough, the accuracy would decrease in the region of whole image while interrogation window is needed to be large to detect real

83

displacements.

The result from both image pairs shows that a series of test on window size is needed before the PIV analysis. In the case that the deformation is not obvious, the windows size should be smaller, but it cannot be smaller than the average size of targets in the image. In the base that deformation is obvious, the window size can be larger, but it would affect the result while the size is too large, or an interrogation window include two or more objects.

(a)

(b)
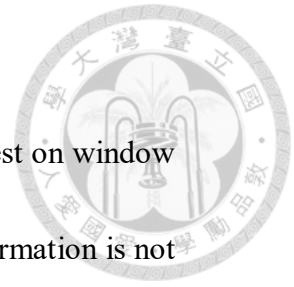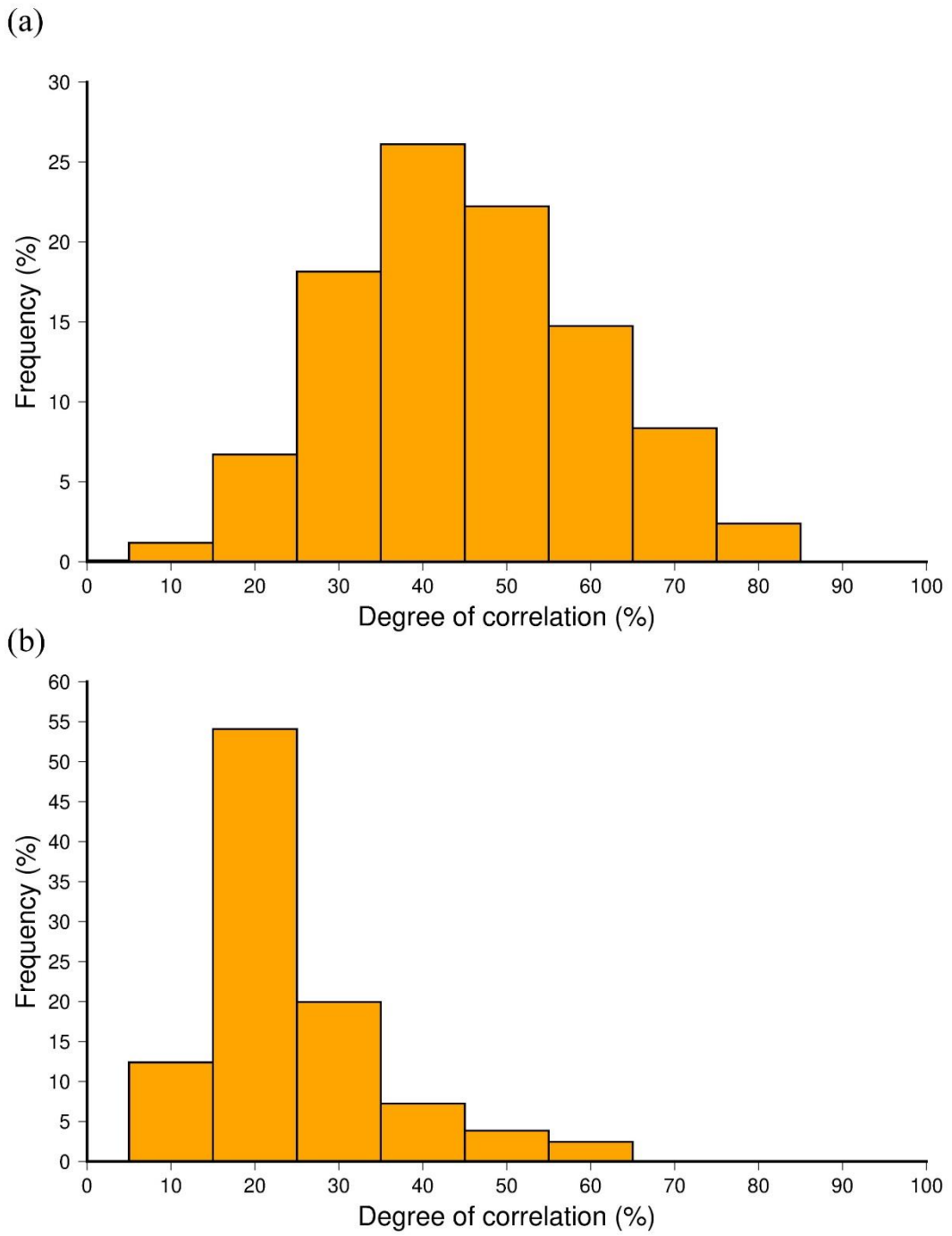
Figure 5-3. Histogram of correlation of vectors in different pairs within frame A. (a) is the result in the pre-event pair, and the window size is 32 pixels x 32 pixels. (b) is the result in post-event pair, and the window size is 256 pixels x 256 pixels.

5.2 Result from PIV analysis
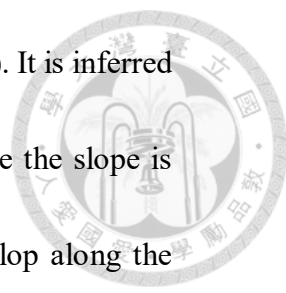
In frame A, where the Yucheliao Landslide is, the result from the PIV analysis shows a southward slip in the post-event pair (Fig. 4-7 to 4-9). Within the landslide block, the magnitude of displacement reaches 60 m in the upper part, and that in the lower part is average 40 m. The difference in displacement between upper part and lower part of the Yucheliao Landslide indicates that the slip rate of the lower part is lower than the upper part while the landslide is triggered.

In the frame B, only a small part of the landslide block remained on the slope after the landslide event. From the magnitude map in the post-event pair, the highest displacement concentrates where the scarp is. However, most of the high value results from the severe change in the land cover. The slip direction of the landslide in frame B is estimated from the original aerial photo, and it is in S-E direction.

5.3 Numerical modeling

The results of the slope stability analysis on model (1) to model (3) show that slope is relative stable before the slip surface develops (Fig 4-13, 4-17 and 4-21). In the comparison between model (1) and model (3), the geometry of the potential slip surface is mainly circular, but the displacement would
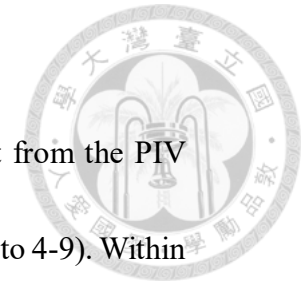
occur little along sandstone-shale interface (Fig. 4-14 and 4-22). It is inferred that the failure would tend to develop as a planar failure while the slope is composed by layered rocks, and the deformation would develop along the boundary between the different rocks. From the model (2), it is noticed that the stability decreases in the slope the with pre-existing slip surface. Considering the model (3), the landslide block tends to deform along the formation boundary first. If the pre-existing deformation or fracture along the boundary is considered, the stability of a slope with layered rock may be overestimated.

From model (1) to model (3), the trial on interpreting the slip surface by ground deformation is applied, and the displacement derived from the PIV analysis is applied to model (2) and model (3). In model (2), the deformation is highly controlled by the pre-existing slip surface so the estimated slip surface is close to the pre-existing slip surface (Fig. 4-20 and 4-25b). Both in model (1) and (3), the estimated slip surface is shallower than the slip surface derived from the shear strength reduction method, and the geometry tends to be planar. In this study, only the displacement of the ground surface is considered in the static analysis of the FEM, while the change in displacement with depth is ignored. Therefore, both the depth of the slip surface and the

87

underground displacement are underestimated. To solve this problem, the

model for interpretation could be applied with other approaches, like

balanced cross-section (Bishop, 1999) or elastic dislocation (Okada, 1985,

1992).
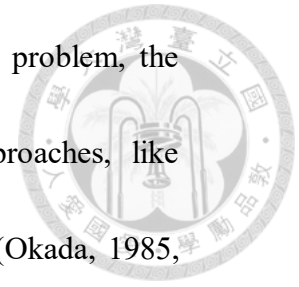
6. Conclusion

● **PIV analysis**

The PIV analysis is applied for the displacement and distribution of the Yucheliao Landslide. In the PIV analysis, velocity vector measurement on the Yucheliao Landslide can be derived by the cross-correlation method.

1. In the pre-event pair of images, the displacement derived from small interrogation window is doubted once the target is larger than interrogation window.

2. In the post-event pair of images, larger interrogation window is set to detect larger displacement, but the degree of correlation would decrease expectedly.

3. In both the pre-event pair and the post-event pair, the change in land cover obviously caused the errors of the displacements derived from PIV analysis. Especially, change in land cover is mainly caused by erosion when Typhoon Morakot hit and the formation of the landslide scarp in the post-event pair.

4. Parametric tests on the size of the interrogation window is needed before the PIV analysis to avoid inaccuracy in result. Larger displacement can be detected when large interrogation window is

set, but the degree of correlation would decrease.

5. The distribution of landslide region in the Yucheliao Landslide and other landslides can be roughly determined since the region with larger displacement tends to occur within the landslide region. The direction of displacement vectors indicates that the slip direction of the Yucheliao Landslide is mainly southward.

● **Numerical modeling**
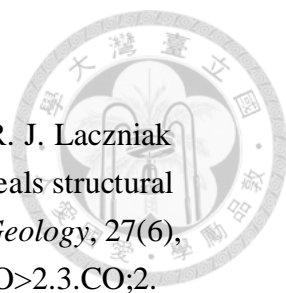
In the numerical modeling, the slope stability analysis by shear strength reduction method is applied, and the geometry of landslide slip surface is interpreted by the FEM analysis.
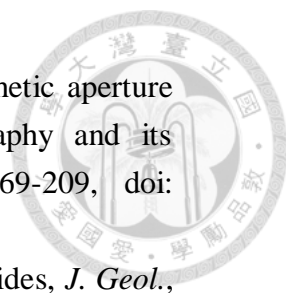
1. By the shear strength reduction method, the results show that both the slope with homogeneous rocks and the slope with layered rocks are relatively stable than slope with the pre-existing slip surface.

2. If the previous deformation or fracture along the strata boundary is considered, the stability of a slope with layered rocks may be overestimated.

3. The slip surface interpreted by surface displacement derived from the numerical modeling is shallower than the slip surface derived by the shear strength reduction method.
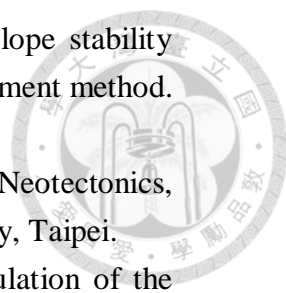
4. The geometry of the interpreted slip surface tends to be a planar

   failure, which is different from the geometry of slip surface derived

   by the shear strength reduction method.
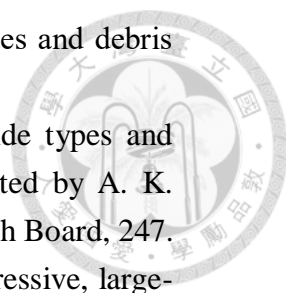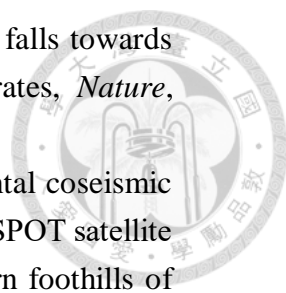
Reference
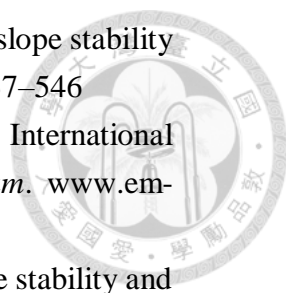
Amelung, F., D. L. Galloway, J. W. Bell, H. A. Zebker, and R. J. Laczniak (1999), Sensing the ups and downs of Las Vegas: InSAR reveals structural control of land subsidence and aquifer-system deformation, *Geology*, 27(6), 483-486, doi: 10.1130/0091- 7613(1999)027<0483:STUADO>2.3.CO;2.

Amitrano, D., M. Costantini, D. Dell'Aglio, A. Iodice, F. Malvarosa, F. Minati, D. Riccio, and Ruello, G. (2018, September). Landslide Monitoring Using Sar Sub-Pixel Offset Tracking. In 2018 IEEE 4th International Forum on Research and Technology for Society and Industry (RTSI) (pp. 1-4). IEEE.

Adrian, R. J., (1991). Particle imaging techniques for experimental fluid mechanics. *Ann. Rev. Fluid Mech.,* 23, 261-304.

Bishop, K. M. (1999). Determination of translational landslide slip surface depth using balanced cross sections. *Environ. Eng. Geosci.*, (2), 147-156.

Bell, J.W., F. Amelung, A. Ferretti, M. Bianchi, and F. Novali (2008), Permanent scatterer InSAR reveals seasonal and long-term aquifer pumping and artificial recharge, *Water Resour. Res.*, 44(2), doi: 10.1029/2007WR006152.

Berardino, P., G. Fornaro, R. Lanari, and E. Sansosti (2002), A new algorithm for surface deformation monitoring based on small baseline differential SAR interferograms. *IEEE Trans. Geosci. Remote Sensing*, 40(11), 2375-2383, doi: 10.1109/TGRS.2002.803792.

Bovenga, F., R. Nutricato, A. Refice, and J. Wasowski (2006), Application of multi-temporal differential interferometry to slope instability detection in urban/peri-urban areas, *Eng. Geol.*, 88(3), 218-239, doi: 10.1016/j.enggeo.2006.09.015.

Bovenga, F., J. Wasowski, D. O. Nitti, R. Nutricato, and M. T. Chiaradia (2012), Using COSMO/SkyMed X-band and ENVISAT C-band SAR interferometry for landslides analysis, *Remote Sens. Environ.*, 119, 272-285, doi: 10.1016/j.rse.2011.12.013.

Bozzano, F., C. Esposito, S. Franchi, P. Mazzanti, D. Perissin, A. Rocca, and E. Romano, (2015), Understanding the subsidence process of a quaternary plain by combining geological and hydrogeological modelling with satellite InSAR data: The Acque Albule Plain case study, *Remote Sens. Environ.*, 168, 219-238, doi: 10.1016/j.rse.2015.07.010.
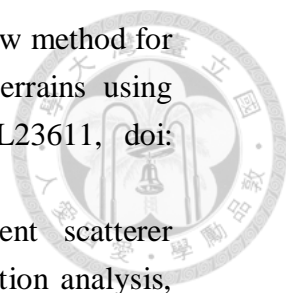
Bürgmann, R., P. A. Rosen, and E. J. Fielding (2000), Synthetic aperture radar interferometry to measure Earth's surface topography and its deformation, *Ann. Rev. Earth Planet. Sci.*, 28(1), 169-209, doi: 10.1146/annurev.earth.28.1.169

Campbell, C. S. (1989), Self-lubrication for long runout landslides, *J. Geol.*, 653-665.

Carter, M., and S. P. Bentley (1985). The geometry of slip surfaces beneath landslides: predictions from surface measurements. *Can. Geotec. J.*, 22(2), 234-238.

Cascini, L., G. Fornaro, and D. Peduto (2009), Analysis at medium scale of low-resolution

DInSAR data in slow-moving landslide-affected areas, *ISPRS J. Photogramm. Remote Sens.*, 64(6), 598-611, doi: 10.1016/j.isprsjprs.2009.05.003.

Castaldo, R., P. Tizzani, P. Lollino, F. Calò, F. Ardizzone, R. Lanari, F. Guzzetti, and M. Manunta (2015), Landslide kinematical analysis through inverse numerical modelling and differential SAR interferometry. *Pure Appl. Geophys.*, 172(11), 3067-3080, doi: 10.1007/s00024-014-1008-3.

Central Geological Survey (2011a). Final report to monitoring, expansion and maintenance of the warming system for the north slope of Lushan hot spring district, 63 pp., MOEA, Taipei.

Central Geological Survey (2011b). Observation of mechanisms of large-scale potential landslide areas and slope stability monitoring (1/4), 325 pp., MOEA, Taipei.

Central Geological Survey (2012a), The analysis for potential large-scale landslide areas of Typhoon Morakot disaster zone in southern Taiwan, 33 pp., MOEA, Taipei.

Central Geological Survey (2012b). Observation of mechanisms of large-scale potential landslide areas and slope stability monitoring (2/4), 384 pp., MOEA, Taipei.

Central Geological Survey (2013a), The analysis for potential large-scale landslide areas of Typhoon Morakot disaster zone in central Taiwan, 54 pp., MOEA, Taipei.

Central Geological Survey (2013b), The analysis for potential large-scale landslide areas of Typhoon Morakot disaster zone in eastern Taiwan, 52 pp., MOEA, Taipei.
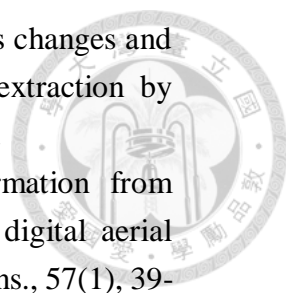
Chen, X., L. Zhang, L. Chen, X. Li, and D. Liu, (2019). Slope stability analysis based on the Coupled Eulerian-Lagrangian finite element method. *B. Eng. Geol. Environ.*, 1-13.

Chang, K.-J. (1998). Physical and Numerical Modeling of Neotectonics, Western Taiwan (Master Thesis). National Taiwan University, Taipei.

Chang, K.-J., and A. Taboada (2009), Discrete element simulation of the Jiufengershan rock‑ and‑soil avalanche triggered by the 1999 Chi‑Chi earthquake, Taiwan, *J. Geophys. Res. Earth Surface*, 114(F3), doi: 10.1029/2008JF001075.

Chan, Y., S. Chou, and J. Lee (2004, December). Reconstruction of high-resolution horizontal displacement field using aerial photogrammetry and particle image velocimetry: an example from the Taiwan Chi-Chi Earthquake rupture area. In *AGU Fall Meeting* Abstracts.

Chen, R.-F., and J.-C. Lee (2005). Application of the particle image velocimetry (PIV) technique to obtain near-fault surface displacement field: a case study of the 2003, Mw= 6.5, Chengkung earthquake in eastern Taiwan. In *Geodynamics and Environment in East Asia International Conference & 5th Taiwan–France Earth Science Symposium*.

Chen, R. F., Lee, C. Y., Yin, H. Y., Huang, H. Y., Cheng, K. P., & Lin, C. W. (2017, May). Monitoring the deep-seated landslides by using ALOS/PALSAR satellite imagery in the disaster area of 2009 Typhoon Morakot, Taiwan. In *Workshop on World Landslide Forum* (pp. 239-247). Springer, Cham.

Chigira, M. (1992), Long-term gravitational deformation of rocks by mass rock creep, Eng. Geol., 32(3), 157-184.

Chiu, C.-H. (2018), Improving geological mapping by using high-resolution DEM: An example from the fold-thrust belt around the Taipei region (Master Thesis). National Taiwan University, Taipei.

Colesanti, C., and J. Wasowski (2006), Investigating landslides with space-borne Synthetic Aperture Radar (SAR) interferometry, *Eng. Geol.*, 88(3), 173-199, doi: 10.1016/j.enggeo.2006.09.013.

Corominas, J. (1996), The angle of reach as a mobility index for small and large landslides, *Can. Geotech. J.*, 33(2), 260-271.

Crosetto, M., O. Monserrat, M. Cuevas-González, N. Devanthéry, and B. Crippa (2015), Persistent scatterer interferometry: A review, *ISPRS J. Photogramm. Remote Sens.*, 115, 78-89, doi: 10.1016/j.isprsjprs.2015.10.011.
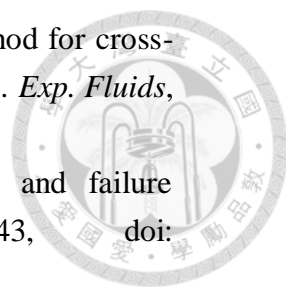
Crosta, G. B., & Frattini, P. (2008). Rainfall-induced landslides and debris flows. *Hydro. Process.*, 22(4), 473-477.

Cruden, D. M., and D. J. Varnes (1996), Chapter 3-Landslide types and processes, in *Landslides: investigation and mitigation*, edited by A. K. Turner and L. R. Schuster, pp. 36-75, Transportation Research Board, 247.

Cundall, P. A. (1971), A computer model for simulating progressive, large-scale movements in blocky rock systems, *Proc. Symp. Rock Fracture (ISRM)*, Nancy, Vol. 1.

Cundall, P. A., and O. D. Strack (1979), A discrete numerical model for granular assemblies, *Geotechnique*, 29(1), 47-65.

Cundall, P. A., and R. D. Hart (1992) Numerical modelling of discontinua, *Eng. Comput.*, vol.

9 Iss: 2, pp. 101-113, doi: http://dx.doi.org/10.1108/eb023851.

Dai, F. C., C. F. Lee, and Y. Y. Ngai (2002), Landslide risk assessment and management: An overview, *Eng. Geol.*, 64(1), 65-87, doi:10.1016/S0013-7952(01)00093-X.

Darvish, M., R. Sclögel, L. Bruzzone, and G. Cuozzo (2018), Integration of PSI, MAI, and Intensity-Based Sub-Pixel Offset Tracking Results for Landslide Monitoring with X-Band Corner Reflectors—Italian Alps (Corvara), Remote Sens, 10(3), 409

Dassault Systèmes (2014) Abaqus Analysis User's Guide, Version 6.14.

Dawson, E. M., W. H. Roth, and A. Drescher, (1999). Slope stability analysis by strength reduction. Geotechnique, 49(6), 835-840.

Davies, T. (2014), Landslide Hazards, Risks, and Disasters, in *Hazards and Disasters Series*, edited by J. F. Shroder, Elsevier, Netherlands.

De Michele, M., D. Raucoules, J. de Sigoyer, M. Pubellier, and N. Chamot-Rooke (2010). Three-dimensional surface displacement of the 2008 May 12 Sichuan earthquake (China) derived from synthetic aperture radar: Evidence for rupture on a blind thrust, Geophys. J. Int., 183, pp. 1097-1103

Debella-Gilo, M., and A. Kääb (2011). Sub-pixel precision image matching for measuring surface displacements on mass movements using normalized cross-correlation. *Remote Sens. Environ.*, 115(1), 130-142.

Desai, C. S. and H. J. Siriwardane (1972) Constitutive Laws for Engineering Materials with Emphasis on Geologic Materials: Rainbow-Bridge Book Co. Ltd.

Dieterich, J. H. (1992) Earthquake nucleation on faults with rate-and state-dependent strength. *Tectonophysics*, 211(1-4), 115–134.

95
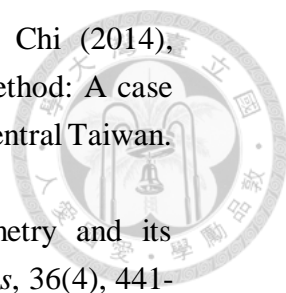
Di Toro, G., D. L. Goldsby, and T. E. Tullis (2004), Friction falls towards zero in quartz rock as slip velocity approaches seismic rates, *Nature*, 427(6973), 436-439, doi: 10.1038/nature02249.

Dominguez, S., J. P. Avouac, and R. Michel, (2003). Horizontal coseismic deformation of the 1999 Chi-Chi earthquake measured from SPOT satellite images: Implications for the seismic cycle along the western foothills of central Taiwan. *J. Geophys. Res.- Sol. Ea.*, 108(B2).

Dong, Y.-H. (2017), Assessment of Potential Landslide Hazard by PS-InSAR and Distinct Element Method: A Case Study in Slate Belt, Central Taiwan (Master thesis). National Taiwan University, Taipei.

Dramis, F., and M. Sorriso-Valvo (1994), Deep-seated gravitational slope deformations, related landslides and tectonics, *Eng. Geol.*, 38(3), 231-243, doi: 10.1016/0013- 7952(94)90040-X.

Driscoll, F. G. (1986). Groundwater and wells. St. Paul, Minnesota: Johnson Filtration Systems Inc., 1986, 2nd ed.

Duncan, J. M. (1996). State of the art: limit equilibrium and finite-element analysis of slopes. *J. Geotech. Eng.*, 122(7), 577-596.

Ferretti, A., C. Prati, and F. Rocca (2001), Permanent scatterers in SAR interferometry, *IEEE Trans. Geosci. Remote Sensing*, 39(1), 8-20, doi: 10.1109/36.898661.

Fruneau, B., J. Achache, and C. Delacourt (1996), Observation and modelling of the Saint- Etienne-de-Tinée landslide using SAR interferometry, *Tectonophysics*, 265(3), 181-190, doi: 10.1016/S0040-1951(96)00047-9.

Gabriel, A. K., R. M. Goldstein, and H. A. Zebker (1989), Mapping small elevation changes over large areas: differential radar interferometry, *J. Geophys. Res.*, 94(B7), 9183–9191, doi: 10.1029/JB094iB07p09183.

Glenn, N. F., D. R. Streutker, D. J. Chadwick, G. D. Thackray, and S. J. Dorsch (2006), Analysis of LiDAR-derived topographic information for characterizing and differentiating landslide morphology and activity, *Geomorphology*, 73(1), 131-148, doi:10.1016/j.geomorph.2005.07.006.

Gomberg, J., P. Bodin, W. Savage, and M. E. Jackson (1995), Landslide faults and tectonic faults, analogs? : The Slumgullion earthflow, Colorado. *Geology*, 23(1), 41–44.

Griffiths, D. V. (1982) Computation of bearing capacity factors using finite elements. *Geotech.*, 32(3), 195–202

Griffiths, D. V. and P.-A. Lane (1999) Slope stability analysis by finite elements. *Geotech.,* 49(3), 387–403
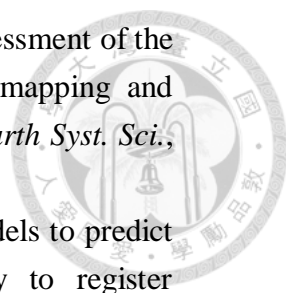
Griffiths, D.V., and R. M. Marquez (2007) Three-dimensional slope stability analysis by elasto-plastic finite elements. *Geotech.,* 57(6), 537–546

Guha-Sapir, D., R. Below, and P. Hoyois (2019), EM-DAT: International disaster database, *Univ. Cathol. Louvain, Brussels: Belgium.* www.em-dat.net. Accessed, 20.

Gurocak, Z., S. Alemdag, and M. M. Zaman (2008). Rock slope stability and excavatability assessment of rocks at the Kapikaya dam site, Turkey. *Eng. Geol.*, 96(1-2), 17-27.

Guzzetti, F., S. Peruccacci, M. Rossi, and C. P. Stark (2007), Rainfall thresholds for the initiation of landslides in central and southern Europe, *Meteor. Atmos. Phys.*, 98(3-4), 239-267, doi: 10.1007/s00703-007-0262-7.

Hammouri, N. A., A. I. H. Malkawi, and M. M. Yamin, (2008). Stability analysis of slopes using the finite element method and limiting equilibrium approach. *B. Eng. Geol. Environ.*, 67(4), 471.

Han, R., T. Shimamoto, T. Hirose, J.-H. Ree, and J. I. Ando (2007), Ultralow friction of carbonate faults caused by thermal decomposition, *Science*, 316(5826), 878-881, doi: 10.1126/science.1139763.

Handwerger, A. L., Rempel, A. W., Skarbek, R. M., Roering, J. J., & Hilley, G. E. (2016), Rate-weakening friction characterizes both slow sliding and catastrophic failure of landslides. *P. Natl. A. Sci.*, 113(37), 10281-10286.

Hanssen, R. F. (2001), *Radar interferometry: Data interpretation and error analysis* (vol. 2), 308 pp., Springer Science & Business Media, Press, Netherlands.

Hibbitt, Karlsson, and Sorensen (1996), Abaqus Theory Manual v5.6, Hibbitt, Karlsson ＆Sorensen INC., US.

Hibbitt, Karlsson, and Sorensen, (1997) Abaqus Theory Manual, v5.7, Hibbitt, Karlsson ＆Sorensen INC., US.

Hilley, G. E., R. Bürgmann, A. Ferretti, F. Novali, and F. Rocca (2004), Dynamics of slow- moving landslides from permanent scatterer analysis, *Science*, 304(5679), 1952-1955, doi: 10.1126/science.1098821.

Highland, L., and P. T. Bobrowsky (2008), *The landslide handbook: a guide to understanding landslides*, 129 pp, U.S. Geological Survey Circular, 1325.

Ho, W.-Y. (2006). 3-D Distinct Element Modeling for the current crustal deformation of southwestern Taiwan (Master Thesis). National Taiwan University, Taipei.
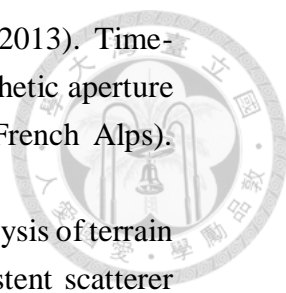
Hooper, A., H. Zebker, P. Segall, and B. Kampes (2004), A new method for measuring deformation on volcanoes and other natural terrains using InSAR persistent scatterers, *Geophys. Res. Lett.*, 31, L23611, doi: 10.1029/2004GL021737.

Hooper, A., P. Segall, and H. Zebker (2007), Persistent scatterer interferometric synthetic aperture radar for crustal deformation analysis, with application to Volcán Alcedo, Galápagos, *J. Geophys. Res.*, 112, B07407, doi: 10.1029/2006JB004763.

Hung, W.-C., C. Hwang, Y.-A. Chen, C.-P. Chang, J.-Y. Yen, A. Hooper, and C.-Y. Yang (2011), Surface deformation from persistent scatterers SAR interferometry and fusion with leveling data: A case study over the Choushui River Alluvial Fan, Taiwan, *Remote Sens. Environ.*, 115(4), 957-967, doi: 10.1016/j.rse.2010.11.007.

Industrial Technology Research Institute (2011), Applied to Monitor Subsidence and Investigate Mechanism in Taipei, Changhwa and Yunlin Area in 2011, Water Resources Agency, Ministry of Economic Affairs, Taipei, Taiwan. (in Chinese)

Isaacs, A. J., J. P. Evans, P. T. Kolesar, and T. Nohara (2008). Composition, microstructures, and petrophysics of the Mozumi fault, Japan: In situ analyses of fault zone properties and structure in sedimentary rocks from shallow crustal levels. *J. Geophys. Res.-Sol. Ea.*, 113(B12).

Itasca, Consulting Group Inc. (2008), User's Guide of PFC3D Particle Flow Code in 3 Dimensions, Minneapolis, Minnesota, USA.

Iverson, R. M., S. P. Schilling, and J. W. Vallance (1998), Objective delineation of lahar- inundation hazard zones, *Geol. Soc. Amer. Bull.*, 110(8), 972-984, doi: 10.1130/0016-7606(1998)110<0972:ODOLIH>2.3.CO;2v. 110 no. 8 p. 972-984.

Iverson, R. M. (2000), Landslide triggering by rain infiltration, *Water Resour. Res.*, 36(7), 1897-1910, doi: 10.1029/2000WR900090.

Javankhoshdel, S., N. Luo, and R. J. Bathurst (2017). Probabilistic analysis of simple slopes with cohesive soil strength using RLEM and RFEM. *Georisk: Assess. Manag. Risk Eng. Syst. Geohazards*, 11(3), 231-246.

Jibson, R. W. (2007), Regression models for estimating coseismic landslide displacement, *Eng. Geol.*, 91(2), 209-218, doi: 10.1016/j.enggeo.2007.01.013.
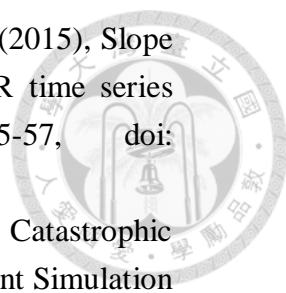
Kääb, A., and M. Vollmer (2000). Surface geometry, thickness changes and flow fields on creeping mountain permafrost: automatic extraction by digital image analysis. *Permafrost Periglac.*, 11(4), 315-326.

Kääb, A. (2002), Monitoring high-mountain terrain deformation from repeated air-and spaceborne optical data: examples using digital aerial imagery and ASTER data. ISPRS J. Photogramm. Remote sens., 57(1), 39-52, doi: 10.1016/S0924-2716(02)00114-4.

Kanungo, D. P., A. Pain, and S. Sharma (2013). Finite element modeling approach to assess the stability of debris and rock slopes: a case study from the Indian Himalayas. *N. Hazards*, 69(1), 1-24.

Kasai, M., M. Ikeda, T. Asahina, and K. Fujisawa (2009), LiDAR-derived DEM evaluation of deep-seated landslides in a steep and rocky region of Japan, *Geomorphology*, 113(1), 57-69, doi: 10.1016/j.geomorph.2009.06.004.

Keefer, D. K. (2000), Statistical analysis of an earthquake-induced landslide distribution—the 1989 Loma Prieta, California event, *Eng. Geol.*, 58(3), 231-249, doi: 10.1016/S0013- 7952(00)00037-5.

Keefer, D. K., and M. C. Larsen (2007), Assessing landslide hazards, *Science*, 316(5828), 1136-1138, doi: 10.1126/science.1143308

Keys, R. (1981). Cubic convolution interpolation for digital image processing. *IEEE T. Acoust. Speech*, 29(6), 1153-1160.

Kilburn, C. R., and D. N. Petley (2003), Forecasting giant, catastrophic slope collapse: lessons from Vajont, Northern Italy, *Geomorphology*, 54(1), 21-32, doi: 10.1016/S0169- 555X(03)00052-7.

Landreth, C. C., R. J. Adrian and C.-S. Yao (1988). Double pulse particle image velocimetry with directional resolution for complex flows. *Exp. Fluids,* 6(2),119-128.

Le, T. M. H. (2014). Reliability of heterogeneous slopes with cross-correlated shear strength parameters. *Georisk: Assess. Manag. Risk Eng. Syst. Geohazards*, 8(4), 250-257.

Lee, J.-H., C.-Y. Wei, and C.-C. Huang (2004) The study of Hungtsaiping landslide using digital aerial photogrametric technique. In *Proceeding of International Symposium on Landslide and Debris Flow Hazard Assessment*, 7th～8th Oct.

Legros, F. (2002), The mobility of long-runout landslides, *Eng. Geol.*, 63(3), 301-331, doi: 10.1016/S0013-7952(01)00090-4.
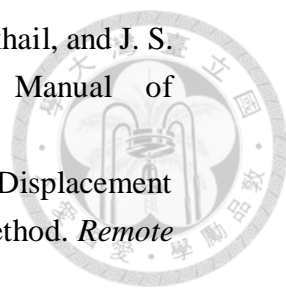
Lecordier, B., and M. Mouqallid (1994). CCD recording method for cross-correlation PIV development in unstationary high speed flow. *Exp. Fluids*, 17(3), 205-208.

Leroueil, S. (2001), Natural slopes and cuts: movement and failure mechanisms. *Geotechnique*, 51(3), 197-243, doi: 10.1680/geot.2001.51.3.197.

Lewis, J. P. (1995) Fast normalized cross-correlation. *Vision Interface*, pp. 120-123

Lillesand, T., R. W. Kiefer, and J. Chipman (2014), Remote sensing and image interpretation, 768 pp., John Wiley & Sons.

Lin, M.-L., H.-J. Liao, and Z.-S. Ueng (2000). The geotechnical hazard caused by Chi-Chi earthquake. In *Proc. International Workshop on the September 21,1999 Chi-Chi Earthquake*, Taichung, Taiwan, June 30, 113-123

Lin, H.-H., M.-L. Lin, C.-C. Chi, and L.-Y. Fei (2014). The study of dip slope landslide mechanisms and activities in Tai-ho Village, Chia-Yi County. *J. Eng. Environ.*, 33, 1-16

Lin, C.-H., and M.-L. Lin (2015), Evolution of the large landslide induced by Typhoon Morakot: A case study in the Butangbunasi River, southern Taiwan using the discrete element method. *Eng. Geol.*, 197, 172-187, doi: 10.1016/j.enggeo.2015.08.022.

Liu, H.-J., J.-F. Li, and C.-C. Chi (2004). Geological map of Taiwan scale 1:50,00: Yulin mapsheet. Central Geological Survey, MOEA, Taipei.

Liu, S.-Y., L.-T. Shao, and H.-J. Li (2015). Slope stability analysis using the limit equilibrium method and two finite element methods. *Comput. Geotech.*, 63, 291-298.

Liu, Y., W. Zhang, L., Zhang, Z., Zhu, J. Hu, and H. Wei, (2018). Probabilistic stability analyses of undrained slopes by 3D random fields and finite element methods. *Geosci. Front.*, 9(6), 1657-1664.

Lo, C.-M., M.-L. Lin, C.-L. Tang, and J.-C. Hu (2011), A kinematic model of the Hsiaolin landslide calibrated to the morphology of the landslide deposit. *Eng. Geol.*, 123(1), 22- 39, doi: 10.1016/j.enggeo.2011.07.002.

Lu, C.-Y. (2012), Assessment of movement and deposition for a potential landslide in Lushan area, central Taiwan by 3D discrete element simulation (Master thesis). National Taiwan University, Taipei.
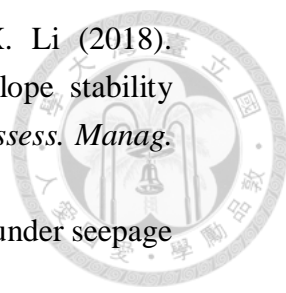
Lu, C.-Y., C.-L. Tang, Y.-C. Chan, J.-C. Hu, and C.-C. Chi (2014), Forecasting landslide hazard by the 3D discrete element method: A case study of the unstable slope in the Lushan hot spring district, central Taiwan. *Eng. Geol.*, 183, 14-30, doi: 10.1016/j.enggeo.2014.09.007.

Massonnet, D., and K. L. Feigl (1998), Radar interferometry and its application to changes in the Earth's surface. *Rev. Geophysics*, 36(4), 441-500, doi: 10.1029/97RG03139.

Matsui, T., and K. C. San (1992). Finite element slope stability analysis by shear strength reduction technique. *Soils Found.*, 32(1), 59-70.

McDougall, S., M. Mckinnon, and O. Hunger (2012), Developments in landslide runout prediction. In *Landslides: Types, Mechanisms and Modeling*, 16, 187-195, edited by J. J. Clague and D. Stead, Cambridge Univ, Press, New York.

Meijering, E., and M. Unser (2003). A note on cubic convolution interpolation. IEEE Image Process., 12(4), 477-479.

Michel, R., J. Avouac, J. Taboury (1999), Measuring ground displacements from SAR amplitude images: Application to the Landers earthquake. *Geophys. Res. Lett.*, 26, pp. 875-878.

Moallemi, S., J. H. Curran, and T. Yacoub (2018, November). On Modeling Rock Slope Stability Problems using XFEM. In *2nd International Discrete Fracture Network Engineering Conference. American Rock Mechanics Association.*

Nadim, F., O. Kjekstad, P. Peduzzi, C. Herold, and C. Jaedicke (2006), Global landslide and avalanche hotspots, *Landslides*, 3(2), 159-173, doi: 10.1007/s10346-006-0036-1.

Nicoletti, P. G., and M. Sorriso-Valvo (1991), Geomorphic controls of the shape and mobility of rock avalanches, Geol. Soc. America Bull., 103(10), 1365-1373, doi: 10.1130/0016-7606(1991)103<1365:GCOTSA>2.3.CO;2v. 103 no. 10 p. 1365-1373.

Nikolaeva, E., T. Walter, M. Shirzaei, and J. Zschau (2014), Landslide observation and volume estimation in central Georgia based on L-band InSAR, *Nat. Hazards Earth Syst. Sci.*, 14(3), 675–688.

Nobach, H., and M. Honkanen (2005). Two-dimensional Gaussian regression for sub-pixel displacement estimation in particle image velocimetry or particle position estimation in particle tracking velocimetry. *Exp. Fluids*, 38(4), 511-515.

Notti, D., J. C. Davalillo, G. Herrera, and O. Mora (2010), Assessment of the performance of X-band satellite radar data for landslide mapping and monitoring: Upper Tena Valley case study, *Nat. Hazards Earth Syst. Sci.*, 10, 1865-1875, doi: 10.5194/nhess-10-1865- 2010.

Notti, D., C. Meisina, F. Zucca, and A. Colombo (2012), Models to predict persistent scatterers data distribution and their capacity to register movement along the slope, Proceedings of Fringe 2011 Workshop, September 19-23, 2011, Frascati, Italy. ESA Special Publication, SP-697 (January 2012, CD. ISBN 978-92-9092-261-2, ISSN 1609- 042X).

Okada, Y. (1985), Surface deformation due to shear and tensile faults in a half-space, Bull. Seismol. *Soc. Am.*, 75(4), 1135–1154.

Okada, Y. (1992), Internal deformation due to shear and tensile faults in a half-space, Bull. Seismol. *Soc. Am.*, 82(2), 1018–1040

Pantelidis, L., and D. V. Griffiths (2013). Integrating Eurocode 7 (load and resistance factor design) using nonconventional factoring strategies in slope stability analysis. *Can. Geotech. J.*, 51(2), 208-216.

Pathier, E., E. Fielding, T. Wright, B. Walker, B. Parsons, and S. Hensley (2006), Displacement field and slip distribution of the 2005 Kashmir earthquake from SAR imagery. *Geophys. Res. Lett.*, 33, p. L20310,

Petley, D. N., T. Higuchi, D. J. Petley, M. H. Bulmer, and J. Carey (2005), Development of progressive landslide failure in cohesive materials, *Geology*, 33(3), 201-204, doi: 10.1130/G21147.1v. 33 no. 3 p. 201-204.

PIVview 2C/3C, user manual, PIVTEC, www.pivtec.com

Poisel, R., and A. Preh (2008), 3D landslide modelling using the particle flow code PFC3D, in Proceedings of the 10th International Symposium on Landslides and Engineered Slopes, edited by Z. Chen, J. Zhang, Z. Li, F. Wu, and K. Ho, pp. 873–879, Taylor and Francis, Landon.

Poisel, R., H. Angerer, M. Pöllinger, T. Kalcher, and H. Kittl (2009), Mechanics and velocity of the Lärchberg–Galgenwald landslide (Austria). *Eng. Geol.*, 109(1), 57-66, doi: 10.1016/j.enggeo.2009.01.002.

Potyondy, D. O., and P. A. Cundall (2004), A bonded-particle model for rock. *Int. J. Rock Mech. Min. Sci.*, 41(8), 1329-1364, doi: 10.1016/j.ijrmms.2004.09.011.

Qing, J.-Y. (1995). A Study on Bearing Behavior of Model Weak Rocks (Master Thesis). National Taiwan University, Taipei.

Raucoules, D., M. De Michele, J. P. Malet, and P. Ulrich (2013). Time-variable 3D ground displacements from high-resolution synthetic aperture radar (SAR). Application to La Valette landslide (South French Alps). *Remote Sens. Environ.*, 139, 198-204.

Riddick, S. N., D. A. Schmidt, and N. I. Deligne (2012), An analysis of terrain properties and the location of surface scatterers from persistent scatterer interferometry, *ISPRS J. Photogramm. Remote Sens.*, 73, 50-57, doi: 10.1016/j.isprsjprs.2012.05.010.

Rubin, A. M. (2008), Episodic slow slip events and rate-and-state friction. *J. Geophys. Res.*,

113(B11), doi: 10.1029/2008JB005642.

Scheidegger, A. E. (1973), On the prediction of the reach and velocity of catastrophic landslides, *Rock Mech. Rock Eng.*, 5(4), 231-236, doi: 10.1007/BF01301796.

Segall, P., A. M. Rubin, A. M. Bradley, J. R. Rice (2010), Dilatant strengthening as a mechanism for slow slip events. *J. Geophys. Res.,* 115(B12), doi: 10.1029/2010JB007449.

Singleton, A., Z. Li, T. Hoey, and J. P. Muller (2014). Evaluating sub-pixel offset techniques as an alternative to D-InSAR for monitoring episodic landslide movements in vegetated terrain. *Remote Sens. Environ.*, 147, 133-144.

Skarbek, R. M., A. W. Rampel, and D. A. Schmidt (2012) Geologic heterogeneity can produce aseismic slip transients. *Geophys Res Lett,* 39(21), doi: 10.1029/2012GL05376

Steketee, J. A. (1958), On Volterra'a dislocation in a semi-infinite elastic medium, *Can. J. Phys.*, 36, 192–205

Soil and Water Conservation Bureau (2006), Planning, investigation and stabilization project of landslide at Tai-14 route from 88 K to 91 K, 241 pp, Taichung, Taiwan.

Soil and Water Conservation Bureau (2008), Investigation, management and planning project of the Lushan landslide area, 270 pp., Taichung, Taiwan.

Sun, K.-T. (2004). Effect of Setback Distance on Loading Behavior of Shallow Foundation in a Poorly Cemented Sandstone (Master thesis). National Chiao Tung University, Hsinchu.

Sun, L., and J. P. Muller (2016). Evaluation of the use of sub-pixel offset tracking techniques to monitor landslides in densely vegetated steeply sloped areas. *Remote Sens.*, 8(8), 659.

Sun, Q., L. Zhang, X.-L. Ding, J. Hu, Z.-W. Li, and J.-J. Zhu (2015), Slope deformation prior to Zhouqu, China landslide from InSAR time series analysis, *Remote Sens. Environ.*, 156, 45-57, doi: 10.1016/j.rse.2014.09.029.

Tang, C.-L. (2010), The Transportation and Deposition of Catastrophic Landslides in Taiwan: Insight from Granular Discrete Element Simulation (Doctoral dissertation). National Taiwan University, Taipei.

Tang, C.-L., J.-C. Hu, M.-L. Lin, J. Angelier, C.-Y. Lu, Y.-C. Chan, and H.-T. Chu (2009),

The Tsaoling landslide triggered by the Chi-Chi earthquake, Taiwan: insights from a discrete element simulation, *Eng. Geol.*, 106(1), 1-19, doi: 10.1016/j.enggeo.2009.02.011.

Tang, C.-L., J.-C. Hu, M.-L. Lin, R.-M. Yuan, and C.-C. Cheng (2013), The mechanism of the 1941 Tsaoling landslide, Taiwan: insight from a 2D discrete element simulation, *Environ. Earth Sci.*, 70(3), 1005-1019, doi: 10.1007/s12665-012-2190-1.

Tang, C.-L., P.-L. Wang, J.-C. Hu, M.-L. Lin, C.-T. Lee, and M.-C. (n.d.), Tang. Reassessment of the kinematic process of 2009 Hsiaolin landslide from 3-D distinct element modeling. Unpublished manuscript.

Tsao, C.-Y. (2017). Characteristics of landslide induced by Typhoon Morakot in central Taiwan via Aerial Photo analysis (Master thesis). National Taiwan University, Taipei.

Tseng, C.-H. (2006), Non-Catastrophic Landslides Induced by the Mw 7.6 Chi-Chi Earthquake in Central Taiwan Revealed by the PIV Analysis (Master thesis). National Taiwan University, Taipei.

Tseng, C.-H., J.-C. Hu, Y.-C. Chan, H.-T. Chu, J.-F. Lee, J. Y. Wei, C.-Y. Lu, and M.-L. Lin (2009). Non-catastrophic landslides induced by the Mw 7.6 Chi-Chi earthquake in central Taiwan as revealed by PIV analysis. *Tectonophysics*, 466(3-4), 427-437.

Ugai, K., and D. O. V. Leshchinsky (1995). Three-dimensional limit equilibrium and finite element analyses: a comparison of results. *Soils Found.*, 35(4), 1-7.

Varnes, D. J. (1978). Slope movement types and processes. In Special report 176: Landslides – Analysis and Control, R. L. Schuster and R. J. Krizek, eds., TRB, National Research Council, Washington, D. C., 11-33.

Vosselman, G., M. Sester, H. Mayer, J. C. McClone, E. M. Mikhail, and J. S. Bethel (2004). Basic computer vision techniques. Manual of photogrammetry, (5), 455-504.

Wang, C., X. Mao, and Q. Wang. (2016). Landslide Displacement Monitoring by a Fully Polarimetric SAR Offset Tracking Method. *Remote Sens.*, 8(8), 624, doi: 10.3390/rs8080624.

Wang, I-S. (2000). Bearing Capacity of Layered Rock Mass (Master Thesis). National Central University, Taoyuan.

Wasowski, J., D. K. Keefer, and C. T. Lee (2011), Toward the next generation of research on earthquake-induced landslides: current issues and future challenges, *Eng. Geol.*, 122(1), 1-8, doi: 10.1016/j.enggeo.2011.06.001.

Wasowski, J., and F. Bovenga (2014), Investigating landslides and unstable slopes with satellite Multi Temporal Interferometry: Current issues and future perspectives. *Eng. Geol.*, 174, 103-138, doi: 10.1016/j.enggeo.2014.03.003.

Westerweel, J. (1993). Digital particle image velocimetry: theory and application.

White, D. J., W. A. Take and M. D. Bolton (2003). Soil deformation measurement using Particle Image Velocimetry (PIV) and photogrammetry, *Geotechnique*, 53(7), 619-631.

Willert, C. E., and M. Gharib (1991). Digital particle image velocimetry. *Exp. Fluids*, 10(4), 181-193.

Woodward, N. B., S. E. Boyer, and J. Suppe (1989). Balanced geological cross-sections: An essential technique in geological research and exploration. AGU, Washington, D. C.

Xu, B., and B.-K. Low (2006). Probabilistic stability analyses of embankments based on finite-element method. *J. Geotech. Geoenviron.,* 132(11), 1444-1454.

Xu, J.-C., Y.-Q. Shang, K.-F. Chen, and J.-F. Yang (2005). Elastoplastic contact FEM analysis of bedding landslide stability. *Chinese J. Rock Mech. Eng.*, 24(13), 2231－2236

Zhang, L., Ding, X., and Lu, Z. (2011a). Ground settlement monitoring based on temporarily coherent points between two SAR acquisitions.*ISPRS J. Photogramm.*, 66(1), 146-152.

Zhang, L., Ding, X., and Lu, Z. (2011b). Modeling PS-InSAR time series without phase unwrapping. *IEEE T. Geosci. Remote.*, 49(1), 547-556.

Zhang, L., F. Wu, Y. Zheng, L. Chen, J. Zhang, and X. Li (2018). Probabilistic calibration of a coupled hydro-mechanical slope stability model with integration of multiple observations. *Georisk: Assess. Manag. Risk Eng. Syst. Geohazards*, 12(3), 169-182.

Zhang, X.-Y., and Z.-H. Dai (2010) Analysis of slope stability under seepage by using Abaqus program. Chinese J. Rock Mech. Eng., 29.

Zhao, L., F. Yang, Y. Zhang, H. Dan, and W. Liu (2015). Effects of shear strength reduction strategies on safety factor of homogeneous slope based on a general nonlinear failure criterion. Comput. Geotech., 63, 215-228.

Zheng, H., D.-F. Liu, and C. Li (2005). Slope stability analysis based on elasto-plastic finite element method. *Int. J. Numer. Meth. Eng.*, 64(14), 1871-1888.

Zheng, H., L.-G. Tham, and D. Liu (2006). On two definitions of the factor of safety commonly used in the finite element slope stability analysis. *Comput. Geotech.*, 33(3), 188-195.

Zheng, H., G. Sun, and D. Liu (2009). A practical procedure for searching critical slip surfaces of slopes based on the strength reduction technique. *Comput. Geotech.*, 36(1-2), 1-5.

Zienkiewicz, O. C., C. Humpheson, and R. W. Lewis (1975). Associated and non-associated visco-plasticity and plasticity in soil mechanics. *Geotechnique*, 25(4), 671-689.

Appendix A. Parametric test on PIV

Window size (pixel)		32	48	64	96
Step 1 [a]	D_{max} (pixel) [e]	23.0136	34.0602	45.5265	67.9687
	$\bar{C}$ (%) [f]	34.54	32.69	31.75	31.02
Step 2 [b]	D_{max} (pixel)	22.9467	34.201	45.2993	67.7109
	$\bar{C}$ (%)	32.04	30.23	29.46	28.95
Step 3 [c]	D_{max} (pixel)	22.7459	34.0355	45.3645	67.6158
	$\bar{C}$ (%)	46.83	42.87	40.44	37.11
Step 4 [d]	D_{max} (pixel)	22.7912	34.1629	45.4216	67.7695
	$\bar{C}$ (%)	48.88	45.32	42.48	38.78

a. Images are only transformed into grayscale images.
b. Brightness and contrast of images are adjusted after step 1.
c. Contrast of images is enhanced after step 2.
d. Ground objects are emphasized by adjusting contrast of images after step 3.
e. D_{max}: Maximum of displacement derived from PIV
f. $\bar{C}$: Average of degree of correlation

Table A-1. Parametric tests on size of interrogation window.

Window size (pixel)		32	48	64	96
Single-Pass interrogation	D_{max} (pixel)	22.7912	34.1629	45.4216	67.7695
	$\bar{C}$ (%)	48.88	45.32	42.48	38.78
Multi-pass interrogation [a]	D_{max} (pixel)	43.0317	60.658	81.9873	144.579
	$\bar{C}$ (%)	50.34	46.64	43.65	39.86
Multi-grid interrogation [b]	D_{max} (pixel)	55.7377	80.7493	75.5898	105.249
	$\bar{C}$ (%)	37.23	22.94	21.46	19.55

a. Maximum number of interrogation passes is 3.
b. Initial grid size is 128 pixels.

Table A-2. Parametric test on different interrogation methods.